# DOUBLE PAIR PRODUCTION

# DOUBLE POSITRON ELECTRON PAIR PRODUCTION, AN INTERACTION OF ELECTROMAGNETIC RADIATION WITH MATTER

By

ANDREW ROBERTSON, B.A.

A Thesis
Submitted to the Faculty of Graduate Studies
in Partial Fulfilment of the Requirements
for the Degree
Doctor of Philosophy

McMaster University
August 1974

DOCTOR OF PHILOSOPHY (1974)
(Physics)

McMASTER UNIVERSITY
Hamilton, Ontario

TITLE: Double Positron-electron Pair Production, an Interaction of Electromagnetic Radiation with Matter

AUTHOR: Andrew Robertson, B.A. (McMaster University)

SUPERVISOR: Dr. T. J. Kennett

NUMBER OF PAGES: xi, 231

SCOPE AND CONTENTS:

The task of detection and measurement of the instantaneous process of double positron-electron pair production was undertaken. Several targets of different atomic number were used, in conjunction with 6.6-MeV gamma rays, to isolate the process from the interfering two-pair processes known as the bremsstrahlung-cascade and the direct-cascade effects. A quantitatively significant value has been determined for the cross section for double pair production relative to that for single pair production.

# ACKNOWLEDGEMENTS

I wish to express my sincerest appreciation to my Research Director, Dr. T. J. Kennett, for his advice and assistance at all times. His wide spectrum of scientific interests and involvements has made my stay at McMaster University a particularly enriching experience. I am also indebted to Dr. W. V. Prestwich for our many enlightening discussions and his deep interest in the challenges of this research project. His insight and encouragement in moments of despair were greatly appreciated.

I am grateful to Mr. John McDougall, Mr. Peter Ernst and the other members of the reactor staff for their assistance and ready cooperation, to Mr. Hector Blanchard for his long-term loan of most of the electronics required for this investigation, and to Mrs. Helen Kennelly for both her great efficiency in typing this manuscript and her patience in awaiting the sporadic arrival of the chapters.

A special word of thanks must be given to my wife, Lynne, and my children for the sacrifices they have endured for my sake.

This work has been supported financially by the National Research Council of Canada and the Government of the Province of Ontario.

## TABLE OF CONTENTS

CHAPTER III (continued) Page

# LIST OF ILLUSTRATIONS

FIGURE TITLE Page

# LIST OF TABLES

# CHAPTER I

# INTRODUCTION

## 1.1 INTRODUCTION

In nature one encounters four primary forces, namely gravitational, weak, electromagnetic, and strong forces. The comparative coupling strengths of these interactions 1) are respectively $\sim 10^{-39}$, $\sim 10^{-13}$, 1/137 and $\sim 1$. Consequently only the latter three interactions are of significance to the experimental nuclear physicist.

The weak interaction is revealed in beta decay where a nucleus undergoes a change of atomic number, without a corresponding change in mass number, by emitting a $\beta^{\pm}$ particle. Following the hypothesis of the neutrino by Pauli 2) in 1931, Fermi 3) in 1934, using time-dependent perturbation techniques (appendix A), gave a complete descriptive theory of beta decay which explained satisfactorily beta spectral shapes, lifetimes, recoil, and angular correlation experiments. The only addition to the completeness of the theory was introduced in 1956 by Lee and Yang 4) who included the nonconservation of parity inherent in weak interactions.

Electromagnetic forces are evidenced in a wide variety of physical phenomena involving the interaction of charged particles and electromagnetic fields. In general these forces are well understood in terms of the classical field equations of Maxwell5) and the concepts of quantum electrodynamics established by Dirac, Heisenberg, and Pauli6). A few notable examples are the de-excitation of nuclear states by gamma emission7) or internal conversion of orbital electrons8), and the interactions of charged particles and photons with matter9).

The strong or nuclear-interaction force is a short-range saturated force which acts between nucleons irrespective of the charge of the nucleons involved. This force, despite considerable and concerted effort, is the least understood of all the forces mentioned so far. The two-body problem, found in nucleon-nucleon scattering and the simple nucleus of deuterium, has been treated with minimal "success" but the many-body problem associated with nuclei of higher mass number has been most resistive to solution. The approach to understanding nuclear forces via potentials has led to a variety of models. A few of the more celebrated models are the shell model of Mayer10), the distorted-potential model of Nilsson11), the vibrational model, and the rotational model. Amongst their several successes one can list the explanation of the magic numbers, the spins and parities of ground states and low lying excited states, nuclear magnetic moments, some energy levels, and the occurrence of $2^+$ excited states in even-even nuclei with large B(E2) values for the ground-state transitions. However, as intimated previously, there exists no unified model which can explain all phenomena attributable to the nuclear interaction.

Although all three of the above forces are involved in the present work the most important will be the electromagnetic force and its delineation in theory by quantum electrodynamics.

## 1.2 QUANTUM ELECTRODYNAMICS

A good theory usually meets with initial success followed by difficulties/or limitations which give rise to a better theory in which the difficulties are removed or wider application is found. Quantum electrodynamics has seen exactly the opposite trend with the immediate difficulties of diverging self-energy and diverging integrals in exact solutions, followed by outstanding success[6)]. Good results can be obtained in the first (non-zero) approximation due to the relatively small coupling constant ($\alpha \equiv \frac{e^2}{\hbar c} = \frac{1}{137}$) involved, and perturbation theory (appendix A), in general, provides an excellent description of the various processes. Higher-order terms not only provide small corrections (i.e. the radiative corrections) but also get rid of the infamous divergences through renormalization theory. Two renowned triumphs of quantum electrodynamics are associated with the anomalous magnetic moment of the electron[12)], and the Lamb shift[13)]. The additional magnetic moment has been measured by Wesley and Rich[14)] to be $(1159657.7 \pm 3.5) \times 10^{-9}$ Bohr magnetons. By comparison, calculated sixth-order radiative corrections[15)] provide the satisfactory result $(1159655.4 \pm 3.3) \times 10^{-9}$ Bohr magnetons. The Lamb shift which represents the unexpected difference in energy between the 2S and the $2P_{1/2}$ states in atomic hydrogen, was measured by Vorburger and Cosens[16] to be 1.057.86±0.06 MHz, whereas radiative corrections to the fourth order[16] predict the excellent theoretical value of 1.057.911±0.012 MHz.

A lucid approach to field quantization via the interaction picture is provided by Mandl[17]. This approach, which is particularly suited to treatment of interacting systems by perturbation theory, allows relativistically covariant calculations. Let us consider the Hamiltonian involved to be

$$H = H_I + H_O , \tag{1.1}$$

where $H_I$ is the interaction part of the Hamiltonian and $H_O$ is the interaction-free part. The equation of motion of the coupled system in natural units ($\hbar=c=1$) can be shown to be

$$\frac{i\partial\phi(t)}{\partial t} = H_I\phi(t) , \tag{1.2}$$

where $\phi(t)$ represents the state vectors involved in the interaction. One can then define a scattering matrix (S-matrix) which will transform the initial state of $\phi(-\infty)$ into the final state of $\phi(\infty)$ via the equation

$$\phi(\infty) = S\phi(-\infty). \tag{1.3}$$

Here $\phi(-\infty)$ and $\phi(\infty)$ are to be considered as meaning long before and long after the interaction has taken place. By integrating equation (1.2) over the range of $-\infty$ to t, and by consecutive resubstitution one gets

$$\phi(t) = \phi(-\infty) + (-i)\int_{-\infty}^{t} dt_1 H_I(t_1)\phi(t_1) \qquad (1.4)$$

$$= \phi(-\infty)+(-i)\int_{-\infty}^{t} dt_1 H_1(t_1)\{\phi(-\infty)+(-i)\int_{-\infty}^{t_1} dt_2 H_I(t_2)\phi(t_2)\}, \qquad (1.5)$$

and so on. A comparison of this development with equation (1.3) reveals that the S-matrix may be interpreted as

$$S = \sum_{n=o}^{\infty} \frac{(-i)^n}{n!} \int_{-\infty}^{\infty}\cdots\int_{-\infty}^{\infty} dt_1 \ldots dt_n P\{H_I(t_1)\ldots H_I(t_n)\} \qquad (1.6)$$

where P{ } stands for the Dyson time-ordered product. This last equation may be rewritten in terms of the interaction density $\mathcal{H}_I$ and space-time integrals as

$$S = \sum_{n=0}^{\infty} \frac{(-i)^n}{n!} \int\cdots\int d^4x_1 \ldots d^4x_n \; P\{\mathcal{H}_I(x_1)\ldots\mathcal{H}_I(x_n)\}, \qquad (1.7)$$

where $d^4x$ stands for $d^3x dt$.

At this juncture one should consider the question of whether or not unperturbed wave functions can be used to describe the initial and final states. This is perfectly permissible when dealing with short-range potentials, and merely implies that there is no interaction when the quanta are far apart. However, in quantum electrodynamics it is necessary to appeal to the adiabatic hypothesis[18)]. This in brief involves the concept of a time-dependent coupling constant $\alpha(t)$ which is switched on between times $-T$ to $T$, with the interaction occurring between times $-\tau$ to $\tau$, where $\infty >> T >> \tau$. Normally, after completing calculations, one would then allow T to tend to infinity, but fortunately, since quantum electrodynamics provides satisfactory solutions in the lowest order of perturbation, one can set $T = \infty$ immediately.

The interaction density $H_I$ found in equation (1.7) may be expressed in accordance with electromagnetic theory as

$$H_I(x) = eS_\mu(x)A_\mu(x), \tag{1.8}$$

where $A_\mu$ represents the photon field and $S_\mu$ the electron-positron current. The latter may be written in terms of the single-particle Dirac theory (appendix B) as

$$S_\mu(x) = i\bar{\psi}(x)\gamma_\mu\psi(x). \tag{1.9}$$

Here $\psi(x)$ is the 4-component spinor wave function of the electron and $\gamma_\mu$ stands for the $4\times4$ Dirac matrices satisfying anti-commutation relations. The interaction density of equation (1.8) may then be rewritten in operator formalism as

$$H_I = ie(\bar{\psi}^+ + \bar{\psi}^-)\gamma_\mu(\psi^+ + \psi^-)(A_\mu^+ + A^-), \tag{1.10}$$

with the following interpretation.

$A^+$ and $A^-$ absorb and create photons respectively.

$\psi^+$ and $\bar{\psi}^-$ absorb and create electrons respectively.

$\bar{\psi}^+$ and $\psi^-$ absorb and create positrons respectively.

Substitution of equations (1.8) and (1.9) into equation (1.7) results in the statement

$$S = \sum_{n=o}^{\infty} \frac{e^n}{n!} \int \cdots \int d^4x_1 \ldots d^4x_n T\{N(\bar{\psi}A\!\!\!/\psi)_{x_1} \ldots N(\bar{\psi}A\!\!\!/\psi)_{x_n}\}. \qquad (1.11)$$

Here $\gamma_\mu$ has been incorporated into $A\!\!\!/$, and the normal product, N( ), implies ordering of absorption operators to the right of creation operators while the T-product, T{ }, implies an ordering in time of the fermion fields. The latter product may be expanded as

$$T\{N(\bar{\psi}A\!\!\!/\psi)_{x_1} \ldots N(\bar{\psi}A\!\!\!/\psi)_{x_n}\} = N\{(\bar{\psi}A\!\!\!/\psi)_{x_1} \ldots (\bar{\psi}A\!\!\!/\psi)_{x_n}\} + C, \qquad (1.12)$$

where C represents the sum of all possible orders of contraction. A contraction may be thought of as simply a means of propagating from $x_i$ to $x_j$.

Rather than delving deeper into the formalism, let us now realize that equation (1.11) describes a scattering matrix which is infinitely expendable in processes involving absorption and creation of fermions and photons, in addition to fermion and photon propagators. For example, $\overset{-}{\bar{\psi}}_2\overset{-}{A}_2\underbrace{\overset{+}{\psi}_2\overset{-}{\bar{\psi}}_1}\overset{+}{A}_1\overset{+}{\psi}_1$ can be understood to mean the absorption of an electron and a photon at $x_1$, the propagation $(\sqcup)$ from $x_1$ to $x_2$ by an electron, and finally the emission at $x_2$ of an electron and a photon. This of course represents one possible description of the Compton effect. A few of the myriad of possible processes are illustrated in the diagrams of figure 1-1. The beautifully simple concepts of the diagrams are due to Feynman$^{19)}$. Conventionally, electrons are drawn as upward pointing arrows, positrons as downward pointing arrows, photons as dashed lines, and time as evolving from bottom to top of the diagrams. The Feynman diagrams of figure 1-1

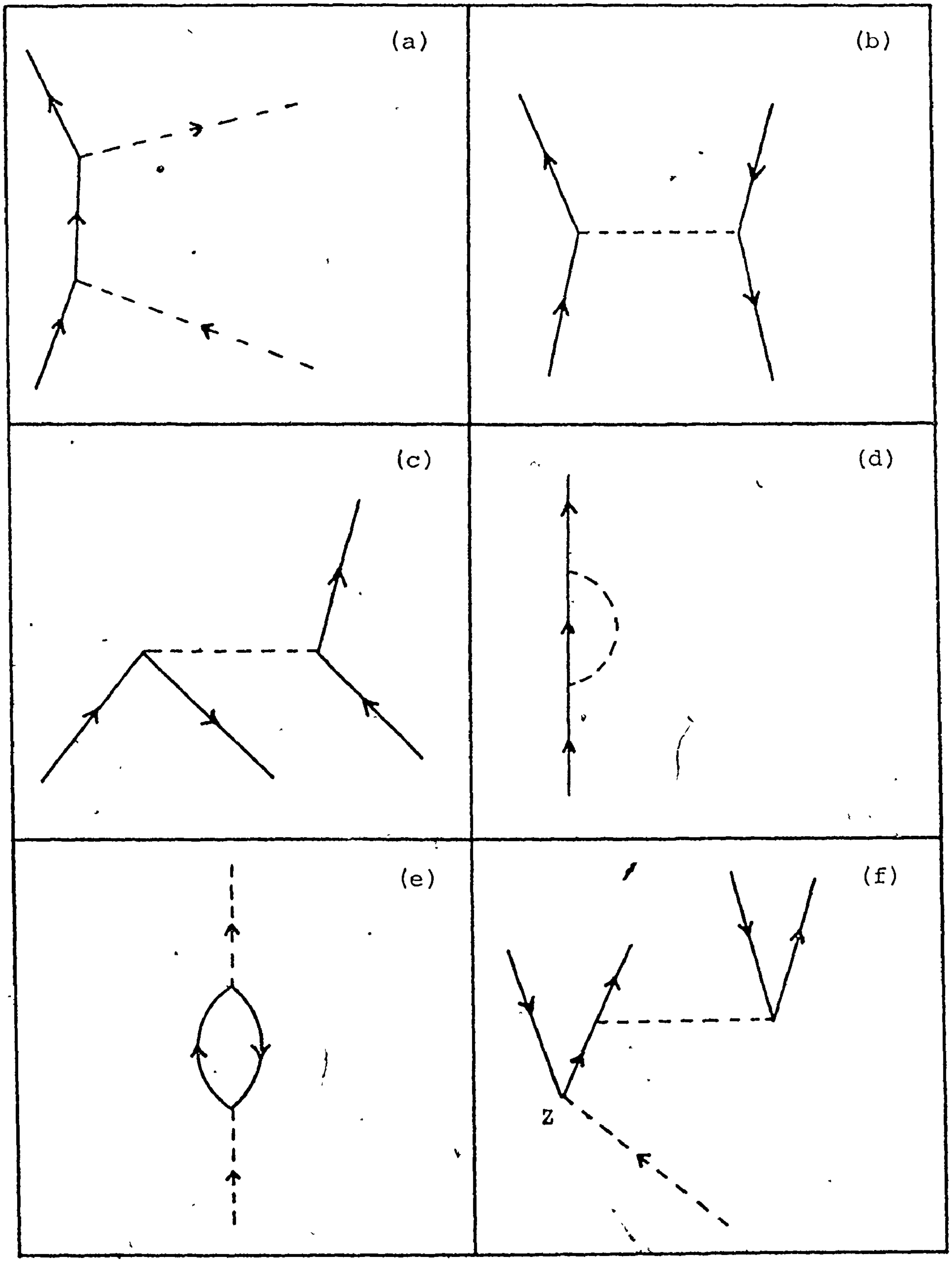

FIG. 1-1 FEYNMAN DIAGRAMS OF VARIOUS PROCESSES

(a) Compton scattering, (b) Bhabha scattering, (c) pair annihilation in the field of an electron, (d) electron self-energy, (e) vacuum polarization, and (f) double pair production.

illustrate possible processes for (a) Compton scattering by an electron, (b) Bhabha scattering of an electron by a positron, (c) pair annihilation in the field of an electron, (d) electron self-energy, (e) vacuum polarization, and (f) double pair production by a photon. It is the isolation and measurement of the process illustrated in figure 1-1(f) which provides the major challenge of this thesis.

## 1.3 DOUBLE POSITRON-ELECTRON PAIR PRODUCTION

Multiple processes in general are of interest in quantum electrodynamics since the reaction probabilities involved cannot be estimated on the basis of classical theory and the correspondence principle. Therefore, a comparison of theoretically calculated cross sections for multiple processes with experimental results constitutes a valuable test of quantum electrodynamics. Although it is commonly accepted that the theory has been well established up to the second expansion term in $\alpha/\pi$, it is also evident that little or no experimental verification exists for higher-order processes. In particular, the importance of the third expansion term has been stressed by Wilkinson and Alburger$^{20)}$ who indicate that not only is it demanded by the g-2 data, but also, that matters of great weight such as hadronic contributions and/or finite length in fundamental theory turn on the validity of the higher-order corrections. Double pair production, which involves the instantaneous creation of two electron-positron pairs from a gamma ray in the field of a nucleus, is a process described in theory by the third expansion term in $\alpha/\pi$.

Consequently the cross section for this process can be expected to be extremely small when compared with that for single pair production. It is therefore not surprising to find very little discussion in the scientific literature of the possibility of double pair creation having been observed experimentally.

The first report of possible observation of double pair production was provided in 1950 by Hooper and King[21] who conducted an experiment in which photographic emulsions were exposed, at an altitude of 68000 feet, to gamma radiation from the decay of neutral pions. In their sampling they found a total of 1380 pair events, two of which appeared to be simultaneous double-pair creations. They were able to deduce that the specific ionization of the tracks in the emulsion possibly corresponded to particles of unit charge $|e|$, and that the measured momenta implied that all particles involved were less massive than protons, several being lighter than $\mu$-mesons. The total energies involved in the two events were found to be 220 and 2000 MeV. The possibility of a particle from a single-pair-creation event interacting with the medium to produce a further pair was considered but was eliminated as being too improbable. The probability was experimentally determined from observation of 52 such trident events from which the mean free path of the projectile particle was calculated as being of the order of 100 cm. The consequent conclusion that double positron-electron pair production had been observed with a probability of 2/1380, compared to single pair creation, appeared to be supported by Heitler[22] whose theoretical considerations indicated an expected ratio of cross sections of $\sigma_{\pi\pi}/\sigma_{\pi} \sim \alpha/\pi$ $(= \frac{1}{430})$. However it has been pointed out[20)] that Heitler's estimate was in error by an additional factor of $\alpha/\pi$ and that therefore the two events were either due to some other phenomenon or a very unlikely fluctuation.

A more correct theoretical estimate of multiple-pair-creation cross sections is due to Afrikian[23)] who calculated the double-pair-production cross section to be

$$\sigma_{\pi\pi} \sim (r_o^2 Z^2 \alpha^3/\pi^2)\ln^2(E/m_oc^2). \tag{1.13}$$

Here $r_o$ is the classical electron radius, Z the atomic number of the target, E the energy of the impinging gamma ray, and $m_oc^2$ the rest-mass energy of an electron. Comparing equation (1.13) with the Bethe-Heitler formula[24)] of

$$\sigma_{\pi} \sim r_o^2 Z^2 \alpha \ln(E/m_oc^2) \tag{1.14}$$

for single pair production, one readily sees that the ratio of cross sections is given by

$$\sigma_{\pi\pi}/\sigma_{\pi} \sim (\alpha/\pi)^2 \ln(E/m_oc^2). \tag{1.15}$$

This ratio does not include the effect of screening of the nuclear field by the atomic electrons. However, the relative effect of screening is believed to be small[25)].

A more complete calculation of the double-pair-production cross section was made, in the extreme relativistic limit, by Serbo[26)] who reported the ratio of cross sections as

$$\sigma_{\pi\pi}/\sigma_{\pi} \approx (L/28)(\alpha/\pi)^2 \ell n(E/m_o c^2). \qquad (1.16)$$

Here L is a constant whose value is of order 43.09[20].

The only other report, known to the author, of possible experimental observation of double pair production was made in 1972 by Wilkinson and Alburger[20]. Basically their experiment consisted of allowing 6.13-MeV gamma rays from the $^{19}F(p,\alpha)^{16}O$ reaction to strike a Ge(Li) spectrometer until a spectrum of excellent statistics had been collected. The resultant pulse-height spectrum was then searched for the presence of a peak which corresponded to an energy 2.044 MeV lower than the full gamma-ray energy of 6.13 MeV. Such a peak was taken to indicate the escape of the four 0.511-MeV quanta expected from the annihilation of two positrons with two electrons. The content of the four-quanta-escape peak was then compared to the content of the more common double-escape peak which arose from the annihilation of positrons created in single-pair production events. Thus, following an accounting for additional effects, a measure of $\sigma_{\pi\pi}/\sigma_{\pi}$ was obtained. A theoretical value of $\sigma_{\pi\pi}/\sigma_{\pi} \sim 2\times10^{-5}$ was predicted by application of equation (1.16) to 6.13 MeV gamma rays and a germanium target. A 15-cm$^3$ co-axial Ge(Li) detector was used first, and then a 4-cm$^3$ one of planar configuration. The latter was chosen since its 0.5 cm thickness was expected to reduce the relative contribution, to the four-escape peak, of interfering effects. A four-escape peak, although barely observable, was shown to exist at the correct energy through use of a minimum $\chi^2$ (chi-squared) test. A total of

$(4.7\pm1.4)\times10^3$ four-quanta escape events and $2.64\times10^7$ double-escape events were found in the data associated with the 15-$cm^3$ detector. The corresponding numbers of events found in the data of the 4-$cm^3$ detector were $(1.14\pm0.94)\times10^3$ and $1.19\times10^7$. However, as mentioned previously, corrections were made necessary by interfering processes. The corrections, calculated on the basis of theory, proved to be able to account for the contents of the four-quanta-escape peaks. The cross section ratio was consequently reported as the negative result $\sigma_{\pi\pi}/\sigma_{\pi} = -(2\pm5)\times10^{-5}$.

The two interfering processes considered by Wilkinson and Alburger, namely the direct and bremsstrahlung cascade effects, are of importance in the present work. However, it is intended that both interferences be accounted for experimentally by using several targets of different atomic number. Schematic representations of these processes, as well as double pair production, are shown in figure 1-2 to illustrate both similarities and differences. Both interferences involve a single-pair production by a gamma ray in the field of a nucleus followed by a further pair production. In the direct-cascade effect either the electron or the positron of the initial pair interacts with another nucleus to form an additional pair. An expression of the production rate of two pairs by means of this effect relative to single pair creation may be given as$^{20)}$

$$P_{D\pi} = bZ, \qquad (1.17)$$

where, for a given gamma-ray energy, b is a constant independent of sample thickness provided that the thickness is significantly

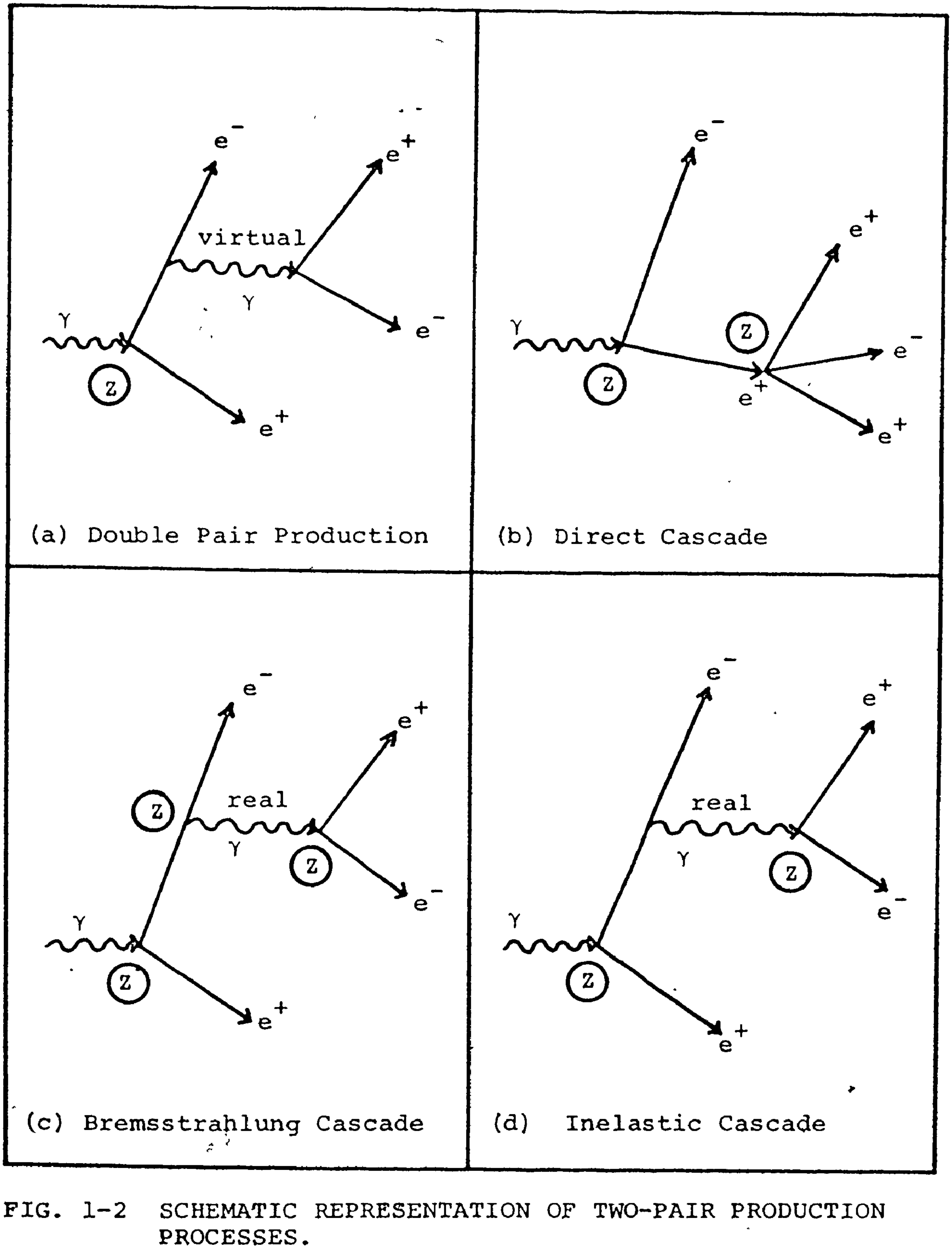

(a) Double Pair Production

(b) Direct Cascade

(c) Bremsstrahlung Cascade

(d) Inelastic Cascade

FIG. 1-2 SCHEMATIC REPRESENTATION OF TWO-PAIR PRODUCTION PROCESSES.

greater than the electron-positron ranges. This effect is particularly important in samples of low atomic number. The dominant interference in materials of high atomic number is the bremsstrahlung cascade. This occurs when one member of the primary pair emits bremsstrahlung radiation which in turn creates an additional pair in the field of a nucleus. The variation of the relative production rate due to this process, with atomic number, is illustrated by the thin sample formula

$$P_{B\pi} = k\rho\ell Z^3/A. \qquad (1.18)$$

Here $\rho$, $\ell$, and A are the sample density, length,and atomic weight respectively whereas k is a constant for monoenergetic gamma rays. Preliminary investigations[27)] with gamma rays of average energy 6.6 MeV reveal an approximate value of $k \sim 10^{-7}$ $cm^2/g$. Additionally, the constant b in equation (1.17) is found to be approximated by $b \approx (0.4\pm0.2)\times10^{-5}$.

Another possible interfering effect is indicated by the theoretical considerations of Shklyarevskii[28)] and Volkovyskii[29)]. They investigated the probability for radiative pair production by very high-energy gamma rays (100 and 200 MeV). In this process a gamma ray, of energy lower than that of the original incident gamma ray, is envisaged as accompanying the production of a positron-electron pair. The cross section for this effect will be smaller than that for ordinary pair production by a factor of order $\alpha/\pi$. The interference arises of course when the second gamma ray is sufficiently energetic to create a second pair. The contribution of this effect, which was disregarded by Wilkinson and Alburger, is believed to be small. However, should the need arise it will be considered experimentally.

# CHAPTER II

# INTERACTION OF RADIATION WITH MATTER

## 2.1 INTRODUCTION

This thesis is concerned with a few, specific, low probability, interactions of radiation with matter. However, it should be realized that such interactions do not occur in total isolation from the more commonly known interactions. It is therefore essential to experimental planning, and interpretation of acquired data, that one have a good appreciation of the complexities of the general processes possible. The radiations of concern in this work are gamma rays, and beta particles derived from the positron-electron pair-production process. A description of the salient features of those effects which are of paramount importance will be given in this chapter. In addition, the concept of cross section, which was introduced without explanation in Chapter I, will be reviewed.

## 2.2 THE CONCEPT OF CROSS SECTION

A summary of the physicist's understanding of the probability of occurrence of a particular interaction often finds expression in the concept of cross section. Although the term is used rather loosely at times, its true meaning can be visualized in two basic but distinct interpretations$^{30)}$. In the first the cross section is envisaged in terms of wave theory, whereas the other requires a corpuscular picture. However, duality in nature dictates that the physicist be able to transfer at will from the one viewpoint to the other.

Consider an interaction in which a plane wave of electromagnetic radiation is incident upon a free electron. Here the wave is regarded as being of infinite dimension, normal to its direction of propogation, when compared with its wavelength and the dimensions of the electron. If the energy flux I of the radiation is known, in units of energy per unit area per unit time, one can calculate the rate at which energy is removed from the beam. Since the power removed is proportional to the intensity I one can write

$$\frac{Q}{t} = \sigma I, \qquad (2.1)$$

where Q is the energy removed by the electron in a time t and $\sigma$ is the constant of proportionality. Since the constant $\sigma$ has units of area it is easy to understand why it is then called the cross section of the interaction. Units of cross section are typically cm$^2$ or barns (per target atom), where 1 barn $\equiv 10^{-24}$ cm$^2$. If several processes are in competition for removal of the power, a similar development can be made for the fraction of energy removed by each. The resultant cross sections are then called partial cross sections, and the relationship holds that the total cross section is given by the sum of the partial cross sections.

Another term which arises is "differential cross section". This most frequently refers to the amount of power removed from the beam and scattered into a solid angle $d\Omega$ at a mean angle of $\theta$. The defining expression is then

$$\frac{dQ}{t} = d\sigma\ I, \qquad (2.2)$$

where $d\sigma$ is the differential cross section.

The above can be extended to a real, physical situation in which many electrons are present. If one considers a thin foil of thickness $dx$ and surface area $S$ containing $N$ atoms per unit volume, each having $Z$ electrons, one can calculate the total power removed from a beam perpendicular to the surface. Since the total number of electrons is $SNZdx$ the equation can be written that

$$\frac{Q}{t} = \sigma I(SNZdx). \qquad (2.3)$$

This also holds for a finely collimated beam of area $S$ since the area of the target illuminated will also be $S$.

The transition to a corpuscular interpretation of cross section is achieved by quantizing the incident radiation into photons of energy $h\nu$ where $h$ is Planck's constant and $\nu$ is the frequency of the wave. Since the total incident energy per unit time can be expressed as $IS$, where $S$ is now the area of the beam, the number of photons per unit time can be written as

$$n = \frac{IS}{h\nu} \ . \qquad (2.4)$$

The number removed from the beam per unit time is given by

$$dn = \frac{(Q/t)}{h\nu} \ . \qquad (2.5)$$

Substitution of the latter two equations in equation (2.3) results in, after rearrangement,

$$\frac{dn}{n} = \sigma NZdx, \qquad (2.6)$$

which is independent of time and area of the beam. From this equation one can interpret the cross section as being the probability that one incident particle will undergo a particular interaction while passing through a foil containing just one target centre per unit area. Integration of equation (2.6), under the realization that dn represents a removal or negative quantity, results in

$$n = n_o e^{-\sigma NZx} \ , \qquad (2.7)$$

which can be interpreted as meaning that n photons per unit time, out of an original rate of $n_o$, remain after passage through a material of thickness x. This represents the well known exponential transmission of photons through a material, under conditions of good geometry. The absorption rate within the target can be written, with $\mu$ replacing $\sigma NZ$, as

$$R = n_o(1-e^{-\mu x}) \ , \qquad (2.8)$$

where $\mu$ is defined as the linear absorption coefficient.

Furthermore, should partial cross sections be involved in the process, the interaction probability associated with a partial cross section $\sigma_p$ can be expressed as

$$P = \frac{\sigma_p}{\sigma_T} (1-e^{-\mu x}) \ , \qquad (2.9)$$

where $\sigma_T$ is the total cross section.

The approach to theoretical calculation of a cross section is also of interest. In quantum mechanics one describes the interaction in terms of an initial state vector $\psi_i$ being transformed into a final state vector $\psi_f$ via an interaction Hamiltonian H. The transition rate of this process is given by time-dependent perturbation theory (Appendix A) to be

$$\lambda = \frac{2\pi}{\hbar} |H_{fi}|^2 \rho_F(E) \qquad (2.10)$$

where $\rho_F(E)$ represents the density of final energy states and $H_{fi}$ stands for the matrix element

$$H_{fi} \equiv \langle\psi_f, H\psi_i\rangle \ . \qquad (2.11)$$

For purposes of illustration the discussion is restricted to first-order perturbation theory although some common interactions require second order. Irrespective of the order of perturbation, the differential cross section for scattering of radiation into a solid angle $d\Omega$ is directly related to the transition probability as

$$d\sigma_s = \text{transition rate} \times d\Omega/\text{incident flux.} \qquad (2.12)$$

In first order theory this becomes

$$d\sigma_s = \frac{2\pi}{\hbar} |H_{fi}|^2 \rho_F(E)d\Omega/\text{incident flux.} \qquad (2.13)$$

The incident flux, which is given by

$$\phi = |\psi_i|^2 v \ , \qquad (2.14)$$

reduces to the velocity v if the wavefunction is normalized to $|\psi_i|^2 = 1$ at large distances from the target. Therefore the differential cross section becomes

$$d\sigma_s = \frac{2\pi}{\hbar} |H_{fi}|^2 \rho_F(E) \frac{d\Omega}{v} \ . \qquad (2.15)$$

When photons are being considered, v is of course the speed of light. In order to evaluate the differential cross section, it is then only necessary that one have knowledge of the density of final energy states. Finally, the total scattering cross section can be found by integrating equation (2.15) over 4π steradians.

## 2.3 INTERACTIONS OF PHOTONS WITH MATTER

Forms of electromagnetic radiations are found under many names which serve only to relate them to their source of origin. Characteristic X-rays are emitted when electrons undergo transitions from one electron shell to another. Annihilation radiation is found when particles annihilate with their antiparticles, such as electrons with positrons. Bremsstrahlung or "braking radiation" is given off when free charged particles are decelerated, and, gamma rays arise from electromagnetic transitions between nuclear energy levels. All can be quantized as photons whose energies are given as hν.

However, significantly, the interaction of each with matter is dependent on photon energy and atomic number of target, but is completely independent of the mode of origin.

There are numerous processes by which electromagnetic radiation can interact with matter$^{31)}$. In the energy range of present concern, namely from a fraction of an MeV to several MeV, photons lose energy by three main processes. These are the photoelectric effect, the pair-production process, and the Compton effect. The region of importance for each is well illustrated in figure 2-1$^{32)}$. The curves drawn in this figure are lines of equal cross section. It is evident that the photoelectric effect is dominant at low energy and high atomic number, pair creation at high energy and high Z, and the Compton effect over the large region of energy and atomic number remaining.

### 2.3.1 THE PHOTOELECTRIC EFFECT

The photoelectric effect, which was discovered in 1887 by Hertz$^{33)}$, defied all attempts at classical explanation. It remained so until Einstein$^{34)}$ in 1905 incorporated Planck's photon concept into the theory. The effect involves the absorption of a photon and the ejection of an electron. Einstein's equation for the kinetic energy of the ejected electron can be written as

$$T = h\nu - B \,, \tag{2.16}$$

where B represents the binding energy of the electron. Momentum considerations lead to the conclusion that a free elec-

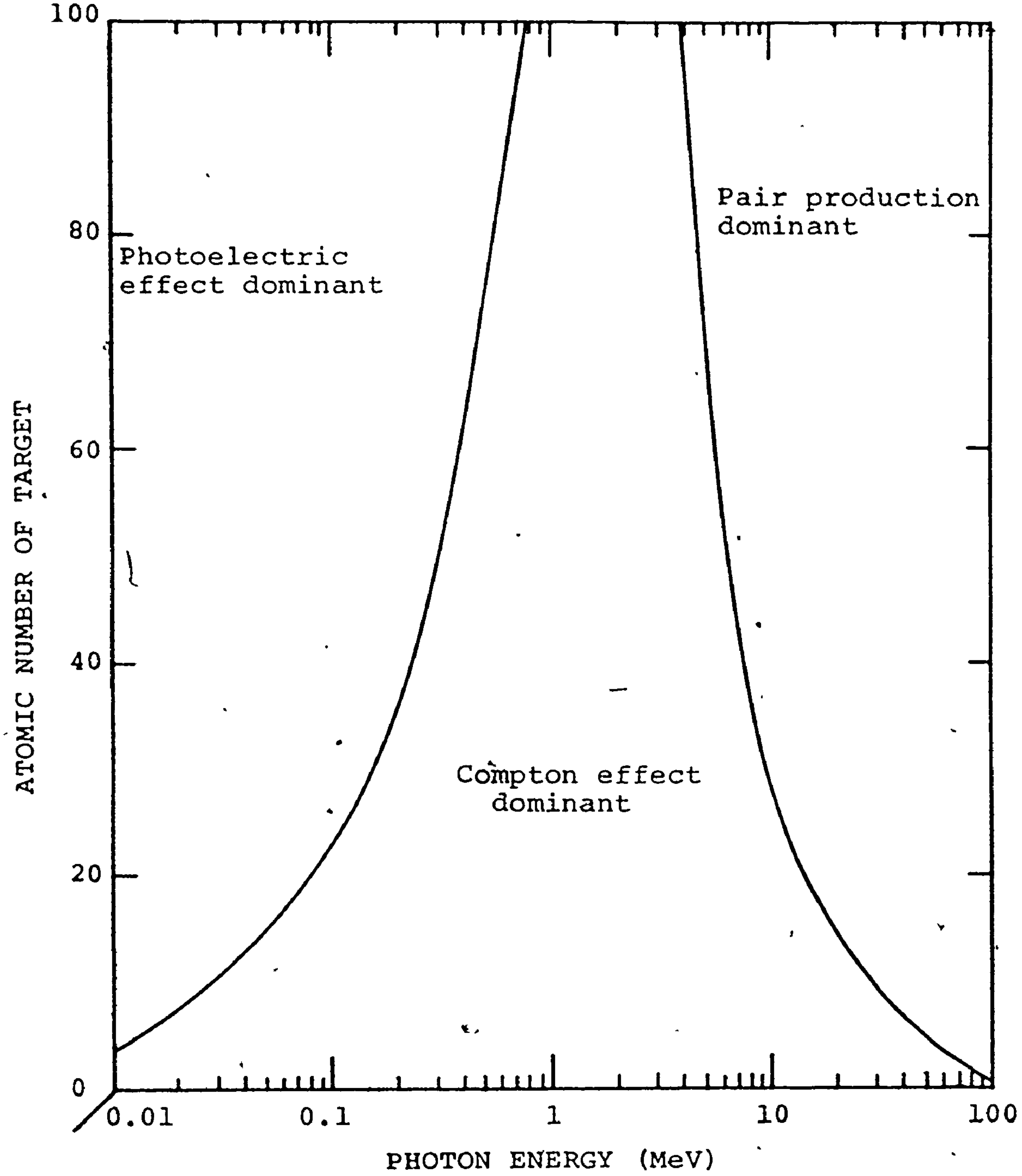

FIG. 2-1 SIGNIFICANCE OF THE PRIMARY PHOTON INTERACTIONS WITH MATTER. The regions of dominance of the photoelectric, Compton, and pair-production cross sections are shown. The curves drawn are lines of equal cross section.

tron cannot completely absorb a photon. The need for a third body to take up the recoil is served by the atom as a whole. Consequently photo-absorption increases rapidly with binding energy. If $h\nu >> B_K$, the binding energy of a K electron, the probability of absorption in the K shell has been estimated[35] as being 80% of the total absorption probability.

Since figure 2-1 indicates that the photoelectric effect is significant for medium and high Z materials at energies below 0.1 MeV, it is reasonable to consider the process theoretically under the constraint $B << h\nu << m_o c^2$, where $m_o$ is the rest mass of the electron. Under this condition the first Born approximation is valid and the final-state electron wavefunction may consequently be represented by a plane wave. Heitler[36] performed a non-relativistic calculation under the above conditions to estimate the differential cross section for photo-absorption within the K shell. He proposed the expression

$$\frac{d\sigma_K}{d\Omega} = \alpha^4 Z^5 r_o^2 \left(\frac{m_o c^2}{h\nu}\right)^{7/2} \cdot \frac{4\sqrt{2}\,\sin^2\theta\cos^2\phi}{(1-\beta\cos\theta)^4} . \qquad (2.17)$$

Here B is the ratio of the velocity of the electron to that of light, $\theta$ is the angle of emission of the electron relative to the photon direction, and $\phi$ is the angle between the plane containing the interaction particles and the plane of the direction of propogation and polarization of the photon. After integrating over the angles in equation (2.17) one obtains

$$\sigma_K = 4\sqrt{2}\ \alpha^4 Z^5 \sigma_o \left(\frac{m_o c^2}{h\nu}\right)^{7/2} , \tag{2.18}$$

where

$$\sigma_o = \frac{8}{3} \pi r_o^{\,2} \tag{2.19}$$

is the classical Thomson[37)] scattering cross section. One should note that $\sigma_K$ falls off quickly with increasing energy but increases rapidly with Z. However, when the photon energy approaches the energy of ionization the Born condition is no longer satisfied and the exact wave functions must be used. Stobbe[38)] has carried out calculations involving hydrogen-like wave functions. His results indicate that equation (2.18) must be multiplied by a function of

$$\xi = (\alpha/\beta) Z. \tag{2.20}$$

At the other extreme of energy, $h\nu >> m_o c^2$, it becomes necessary to use Dirac's relativistic theory (appendix B) for a bound electron. Relativistic wave functions have been incorporated into the transition matrix by Grodstein[39)]. For very low energies Grodstein's formulation reduces to that of Heitler, and for very high energy photons it becomes

$$\sigma_K = \frac{3}{2} \sigma_o \alpha^4 Z^5 \left(\frac{m_o c^2}{h\nu}\right) . \tag{2.21}$$

This equation illustrates that, at high energies, as photon energy increases the photoelectric cross section decreases more slowly than is found at low energies.

Additional significant theoretical contributions have been made by several workers[40)]. However, the presently accepted values are those of Brysk and Zerby[41)] in the region of 1 to 6 keV, where calculations show agreement to within 10% of experimental values, and in the 6 to 200-keV region, where experimental confirmation is good to 3%. For photons of higher energy, the Rakavy-Ron[42)] and Schmickley-Pratt[43)] calculations prove to be valid.

### 2.3.2 PAIR PRODUCTION

In the pair production effect a photon interacts with the field of a nucleus to produce a positron-electron pair. In this process the photon energy, which must be greater than 1.022 MeV, is completely absorbed. In addition to the minimum energy requirement of $2m_oc^2$, corresponding to the total rest mass of the two particles created, conservation of momentum requires that another body be present. The nucleus fills this need. Since the nucleus is massive compared to all other particles involved, it removes very little energy from the system. Thus one can write the energy equation of the effect as

$$h\nu = (T_- + m_oc^2) + (T_+ + m_oc^2) \ , \qquad (2.22)$$

where $T_-$ and $T_+$ refer to the kinetic energies of the electron and positron respectively.

Theoretical estimates of pair cross sections are often obtained from consideration of the inverse process of bremsstrahlung production. The similarities, as well as the need for $2m_oc^2$ of energy, are evident from the Dirac energy diagram of figure 2-2. The diagram arises quite naturally from the Dirac relativistic electron theory which requires that there

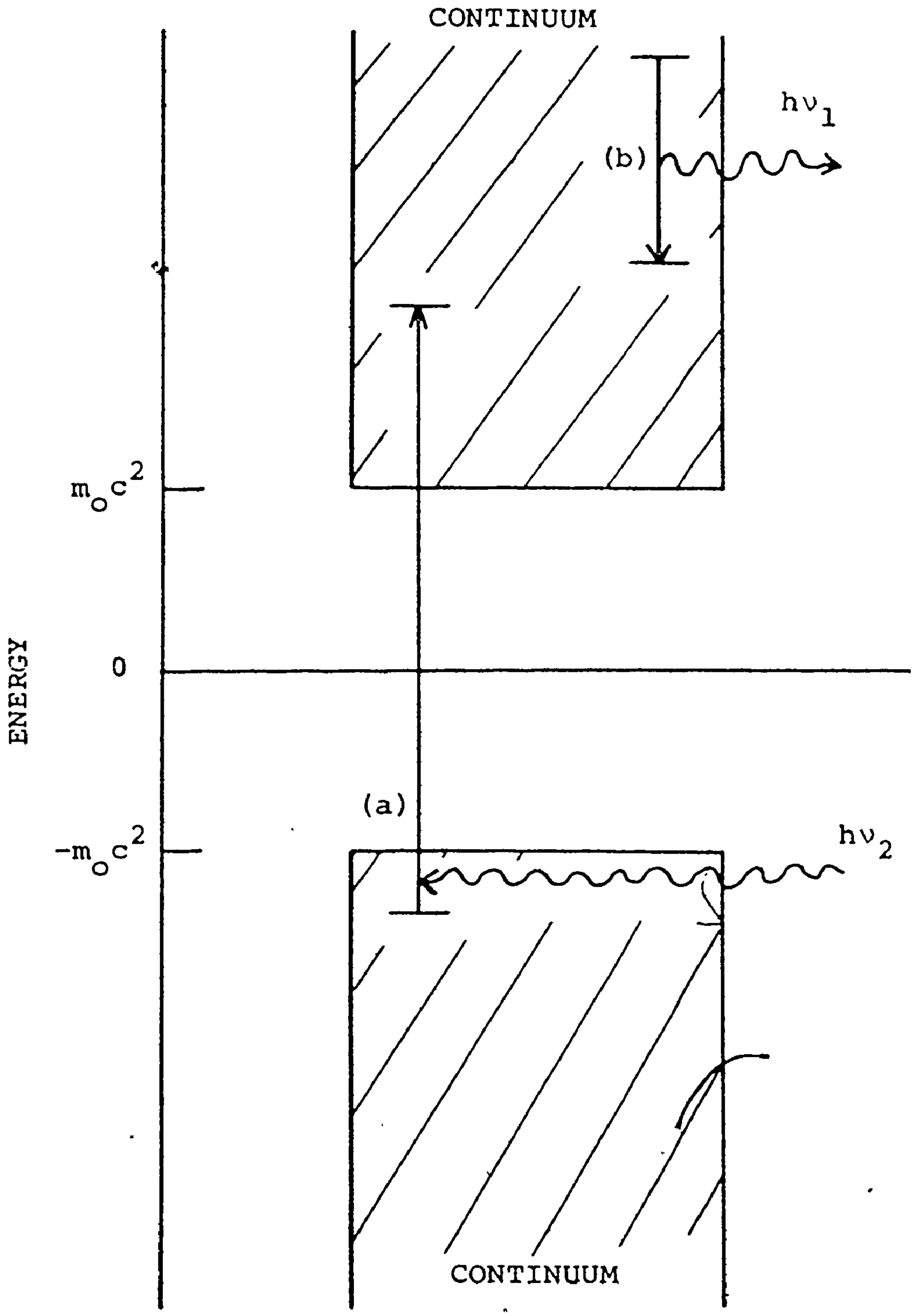

FIG. 2-2 DIRAC ENERGY DIAGRAM FOR FREE ELECTRONS

(a) pair production: when an electron in the filled negative-energy "sea" absorbs a photon of sufficient energy it may be excited to a positive energy state. The hole remaining in the negative-energy continuum and the excited electron are then seen as a positron-electron pair.

(b) Bremsstrahlung: Here a positive-energy electron emits a photon in going to a positive-energy state of lower energy.

be both negative and positive energy regions for the electron, the regions being separated by an energy gap of $2m_oc^2$. The negative energy region is usually envisaged as a completely filled sea of electrons. For the pair production process one can picture a photon of sufficient energy ($h\nu > 2m_oc^2$) striking a negative energy electron and causing it to cross the energy gap into the positive energy region. The vacancy left behind is then seen as a positron. In the associated process of bremsstrahlung creation, a positive energy electron is seen to lose electromagnetic energy in going to a positive state of lower energy. In cross section calculations one can, for weak interactions, invoke the theorem of detailed balance[44)] which transforms the matrix elements of the bremsstrahlung process into the complex conjugate elements of the pair creation effect. Hence the pair-production cross section can be obtained from the bremsstrahlung cross section with changes in the final-state density function[45)].

Bethe and Heitler[24)] derived a formula for the pair cross section through use of Dirac theory and specific assumptions. They chose plane waves to represent both the positron and the electron, and solved the problem under the conditions of the first Born approximation. These are that

$$\frac{Z}{137\beta} << 1 \qquad (2.23)$$

for each particle. They found that the differential cross section for the creation of a positron of kinetic energy $T_+$

could be written as

$$d\sigma_\pi = \frac{\sigma_o{}^2 Z^2 P}{h\nu - 2m_o c^2} \cdot dT_+ \ , \qquad (2.24)$$

where

$$\sigma_o = \frac{1}{137} \left(\frac{e^2}{m_o c^2}\right)^2 = \alpha r_o{}^2 , \qquad (2.25)$$

and the dimensionless quantity P is a complicated function of $h\nu$ and Z. The function, which varies in value from 0 to ∿ 20 as $h\nu$ varies from $2m_oc^2$ to infinity, is shown in figure 2-3 plotted against $T_+/(h\nu-2m_oc^2)$. The significance of this figure lies in the fact that the several curves shown summarize the distribution in energy of positrons created by gamma rays of various energies interacting with targets of different atomic number. Furthermore, the area under each curve is proportional to the total absorption cross section for pair production, under the applicable conditions. The latter fact is easily verified since

$$\sigma_\pi = \int d\sigma_\pi = \sigma_o Z^2 \int_o^{h\nu-2m_oc^2} \frac{P dT_+}{h\nu - 2m_o c^2} \qquad (2.26)$$

$$= \sigma_o Z^2 \int_o^1 P \ d\left[\frac{T_+}{h\nu - 2m_o c^2}\right] . \qquad (2.27)$$

Because the Bethe-Heitler formula involved the very complicated function P, Hough$^{46)}$ developed a prescription formula to describe the curves of figure 2-3. Hough's equation for the differential cross section can be written as

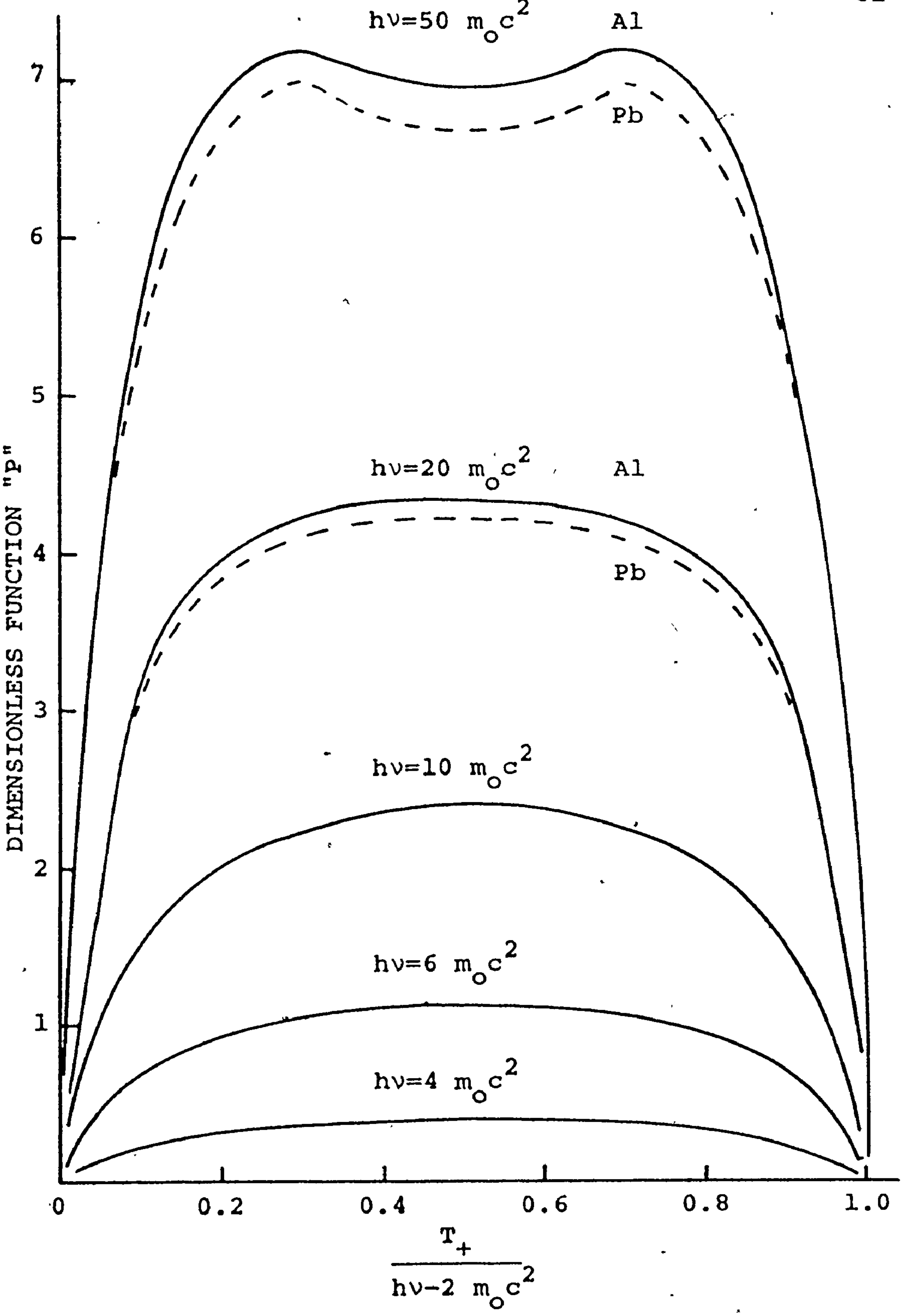

FIG. 2-3 DISTRIBUTIONS IN ENERGY OF THE POSITRON MEMBER OF PAIRS PRODUCED BY GAMMA RAYS

$$d\sigma_\pi = \alpha r_o^2 Z^2 \phi_o t[1+0.135t(1-t^2)(\phi_o-0.52)]dE_+ \ , \qquad (2.28)$$

where

$$t = 2[\eta(1-\eta)]^{1/2} \ , \qquad (2.29)$$

$$\eta = \frac{T_+}{h\nu-2m_oc^2} \ , \qquad (2.30)$$

$E_+$ is the total positron energy, and $\phi_o$ is the differential cross section for a kinetic energy of $T_{max}/2$. This description is valid within the limits $2m_oc^2 \le h\nu \le 15m_oc^2$ as long as the second term is dropped from the expression when $\phi_o$ is less than 0.52.

Unfortunately the Bethe-Heitler formula is in error when the conditions of the Born approximation (equation (2.23)) are not satisfied. This happens when either of the created particles receives little kinetic energy, or when high Z targets are used. The conditions are often restated in terms of restrictions on the photon energy as

$$m_oc^2 << h\nu << 137m_oc^2/Z^{1/3} \ . \qquad (2.31)$$

The Born approximation is then obviously invalid for photon energies near threshold or for energies near the upper limit, which corresponds, for example, to 16 MeV in lead (Z=82). In response to this difficulty, Bethe and Maximom[47)] and Davies et al[48)] have derived extensive formulations without resorting to use of the Born approximation. In brief, these calculations support the Bethe-Heitler analysis if an additional term, f(z) is included in both the differential and total cross sections.

For instance, the total cross section given by Davies can be stated as

$$\sigma_\pi = \frac{28}{9}\alpha r_o^2 Z^2 [\ln(\frac{2h\nu}{E_o}) - \frac{109}{42} - f(z)], \qquad (2.32)$$

where $E_o$ is the rest-mass energy of an electron and f(z) may be obtained from an algorithm provided by Davies et al.

So far, the problem of screening has not been considered. This is significant for high-energy gamma rays. In the process of pair creation the principle contribution to the matrix element[24)] comes from a region of the nuclear field whose radial distance r is given by

$$\frac{h}{2\pi m_o c} \leq r \leq (\frac{h}{2\pi m_o c})(\frac{h\nu}{2m_o c^2}) . \qquad (2.33)$$

Thus it may occur that as photon energy is increased the radius of interaction may exceed the average radius of the K-shell electrons. The nuclear charge will then effectively be reduced. Bethe[49)] has shown that the condition for screening to be effective is that

$$\frac{E_+E_-}{h\nu} > (\frac{9\pi^2}{2^7 Z})^{1/3} \frac{E_o}{2\alpha} . \qquad (2.34)$$

A Thomas-Fermi statistical model of the atom is used in Bethe-Heitler theory to incorporate the effect of screening by the atomic electrons. This model is reasonably applicable except in the case of light elements where the number of electrons available is insufficient to justify statistical averaging. Such screening corrections have been included in the curves of figure 2-3 where separate curves are shown for aluminum and lead. Once again the results of Bethe-Heitler theory are supported by the calculations of Davies et al to be lacking only the correction term f(z). By way of example, out of the several equations available for both differential and total cross sections under various degrees of screening, the total cross section for complete screening is reported by Davies et al to be

$$\sigma_{\pi_{\text{screened}}} = \frac{28}{9}\,\alpha r_o^{\,2} Z^2 [\ln(\frac{183}{Z^{1/3}}) - \frac{1}{42} - f(z)]. \qquad (2.35)$$

Recent excellent experimental work by Henry and Kennett[50)] provides a test of theory in the 2 to 11-MeV region. Nine different targets from carbon to uranium were studied for nineteen different gamma-ray energies. Excellent agreement was obtained with the Goodstein semi-empirical formula[51)] as modified by Øverbø, Mork and Olson[52)]. This formula represents the cross section in terms of the unscreened Bethe-Heitler cross section, the Coulomb correction of Davies et al, and an additive empirical correction which is a function of photon energy.

The angular distribution of particles in a pair production is of interest to the present work. Although no theoretical treatment has had remarkable success, the general picture is that the distribution of particles is strongly peaked in the forward direction for gamma rays of high energy. Bethe and Heitler[24)] indicate that the average angle between the created particles and the incident photon direction is of order

$$\langle\theta\rangle = \frac{m_o c^2}{T} \qquad (2.36)$$

as long as the total kinetic energy available, T, is much greater than $m_oc^2$. At low photon energies ($\sim 2m_oc^2$) the peaking of the distribution is much less marked. Borsellino53) has provided a differential cross section formula, for high electron-positron kinetic energies, derived with the Born approximation. The formula relates to the angle of divergence, Δ, between the positron and the electron. It can be stated as

$$d\sigma = 16\ \alpha r_o^2 Z^2 f(1-f)F \cdot \frac{x\ dx}{(1+x^2)^2} \qquad (2.37)$$

with

$$f = \frac{E_+}{h\nu}\ , \qquad (2.38)$$

$$x = \frac{\Delta}{(2\delta/E_o)}\ , \qquad (2.39)$$

and

$$\delta = \frac{E_o^2 h\nu}{2E_+E_-}\ . \qquad (2.40)$$

Here F is a function of photon energy. Bethe49) has produced a formula which can be seen as similar to equation (2.37) if F is assumed to be constant. Comparison of both formulae with the experimental data of Sandhu et al54) indicates that Bethe provides the better description in the 5 to 20-MeV range. Bethe's formula reproduces the experimental results at small angles where the distribution rises rapidly to the modal value of $x = 1/\sqrt{3}$, but overestimates the empirical distribution at large angles. However, in this energy range, as a result of the experimental data showing reasonable symmetry, the most probable angle is fairly representative of the mean angle. Furthermore, the experimental FWHM (full-width-half-maximum) is approximately 65% of that ascribed by Bethe.

The annihilation of the positron member of a created pair is also of interest. In general one can picture positrons as annihilating with electrons to produce anywhere from one to three quanta. When the positron interacts with a bound electron it is possible for the nucleus to absorb the recoil momentum thus permitting a single-quantum annihilation. This process yields essentially monoenergetic gamma radiation and occurs with a small but finite probability when annihilation takes place in flight. However, in the absence of a recoil absorption mechanism, one-quantum annihilation is strictly forbidden and two or more quanta must be emitted simultaneously. The probability for annihilation with a free electron is dominant over the single-quantum annihilation. Dirac[55)] has calculated the two-quantum annihilation cross section for positron energies ranging from nonrelativistic to extremely relativistic. In terms of his energy diagram (figure 2-2), the probability for annihilation is greatest for an electron near the bottom of the positive energy continuum to make a transition which fills a vacancy near the surface of the negative energy sea. The kinetic energies of the particle and antiparticle are consequently vanishingly small, and the annihilation, which then occurs at rest, results in the emission of two gamma quanta of essentially 0.511-MeV energy, each at an angle of 180° to the other.

In a more physical interpretation, when a positron is slowed down in passing through matter it forms a hydrogen-like system with a free electron in which both particles rotate about a common centre of gravity[56)]. The metastable system so formed, which has a binding energy of approximately 6.8 eV in its ground state, is known as positronium. The positronium may be formed with anti-parallel spins, in which case it is known as the singlet configuration parapositronium. In contrast, when the spins are aligned the triplet state of orthopositronium is formed. The mean lifetime against annihilation is of order $1.25\times10^{-10}$ seconds for parapositronium and $1.4\times10^{-7}$ seconds for the triplet system. Angular momentum considerations require that the singlet annihilation take place via the two-quantum process already discussed, whereas triplet annihilation requires three-quantum emission. The triplet lifetime is seen to be longer by a factor of $1.1\times10^{3}$, but the triplet system is three times more probable than the singlet system. Therefore two-quantum annihilation is more probable than three-quantum by a factor of roughly 370, if one assumes that there is no conversion from orthopositronium to parapositronium.

No discussion of pair production is complete without consideration of pair production in the field of an electron. In 1933 Perrin[57)] pointed out that this effect was possible provided that, for reasons of momentum conservation, the energy of the incident gamma ray was at least $4m_oc^2$. In this effect the target electron can carry off considerable recoil energy. As a result of this, firstly, the process is often referred to as inelastic pair production, and secondly, Bethe-Heitler theory is no longer valid. Since the final state is concerned with three particles, one positron and two electrons, the process is more commonly known as triplet production. Furthermore, because two identical electrons are now involved, the Pauli exclusion principle must be invoked and an exchange effect considered in the cross section. The cross section can also contain contributions in which the photon is absorbed by the target electron and the pair formed by a virtual photon emitted by the electron. This is known as the $\gamma$-e interaction. An intensive review and comparison of theories is provided by Joseph and Rohrlich[58) who indicate that the $\gamma$-e effect increases the triplet cross section at low and intermediate gamma-ray energies but is completely negligible at high energies. The exchange effect is seen to reduce the cross section at low energies but is negligible at high energies. Omission of both effects have no serious repercussions[58) since at very high energies they may be neglected, and at low and intermediate energies they tend to cancel each other.

In a situation in which both pair and triplet production are possible, one can express the ratio of cross sections as[59)

$$\frac{\sigma_{\text{triplet}}}{\sigma_{\pi}} = \frac{1}{kZ} , \qquad (2.41)$$

where k is a constant independent of Z but dependent on energy. Frei et al[60) have measured k to be 2.0±0.2 for 6.3-MeV photons.

Theory and experimental evidence indicate an assymptotic approach to unity as hν tends to infinity. The total production of pairs can then be expressed as

$$\sigma_{\text{Total}} = \sigma_{\pi}(1 + \frac{1}{kZ}) , \qquad (2.42)$$

where $\sigma_{\pi}$ varies as the square of Z. It should be remembered that the second term within the brackets of equation (2.42) makes zero contribution if $h\nu < 4m_oc^2$. Further, it should be realized that triplet production is only of importance in materials of low Z. In carbon (Z=6) with 6-MeV gamma rays, for example, the triplet contribution to the total is approximately 6%.

### 2.3.3 THE COMPTON EFFECT

Figure 2-1 illustrates well the importance of the Compton effect for gamma rays of moderate energy. This effect can be seen to be dominant even for the highest of atomic numbers in the energy region of 0.8 MeV $\leq h\nu \leq 4$ MeV. As the atomic number is reduced the energy region of dominance becomes greater, until, for $Z \leq 24$ the Compton effect is of paramount significance from 0.1 to 10 MeV. Much of the present discussion of Compton events will be based on the excellent, in depth, treatment by R. D. Evans[32).

Basically the Compton effect involves the interaction of a gamma ray with an electron which is considered to be free since its binding energy is small compared to the gamma-ray energy. In the interaction, the gamma ray scatters from the electron at an angle, and in so doing loses some energy.

Energy losses are seen to increase with increasing angle. In the meantime, the energy loss experienced by the gamma ray is received by the electron which then recoils at an angle different from that of the gamma ray. This angle decreases with increased energy of absorption. There are thus two cross sections involved, namely, the scattering cross section for the gamma ray and the absorption cross section for the electron. The differential cross section for the interaction, dσ, which is often called the differential collision cross section, is then given in terms of the above components as

$$d\sigma = d\sigma_s + d\sigma_a \,. \tag{2.43}$$

Here each of the cross sections, and the others to follow, represents the cross section per electron. These differential cross sections are interconnected through the relationships

$$d\sigma_s = \frac{\nu'}{\nu}\, d\sigma \,, \tag{2.44}$$

and

$$d\sigma_a = \frac{\nu-\nu'}{\nu}\, d\sigma, \tag{2.45}$$

with $\nu$ and $\nu'$ standing for the frequencies of the incident and scattered photons respectively.

Credit for the explanation of the effect goes to A. H. Compton$^{61)}$ who, in 1922-23, applied the concepts of duality to the process. He showed that the effect could be readily understood if the photon were assigned an energy $h\nu$ and momentum $h\nu/c$. The interaction could then be pictured as a collision between two particles in which energy and momentum were conserved. Application of the laws of conservation immediately give rise to the following relationships,

$$h\nu' = \frac{h\nu}{1+\gamma(1-\cos\theta)} , \qquad (2.46)$$

$$T_e = h\nu - h\nu' , \qquad (2.47)$$

and

$$\cot\phi = (1+\gamma)\tan(\theta/2) . \qquad (2.48)$$

Here $\phi$ and $\theta$ are the angles of deflection of the electron and photon respectively, $\gamma$ represents $h\nu/m_oc^2$, and $T_e$ is the kinetic energy of the recoiling electron. Equation (2.46) reveals that if $\gamma >> 1$, the energy of the scattered photon will be $2m_oc^2$ at 60°, $m_oc^2$ at 90°, and $0.5\ m_oc^2$ at 180°. Further, no matter what the energy of the incident photon is, there is a minimum, non-zero, energy for the scattered photon corresponding to a maximum kinetic energy delivered to the electron. The maximum kinetic energy, which corresponds to $\theta = 180°$ or $\phi = 0°$, is always slightly less than $h\nu$. The difference approaches a maximum of $0.5\ m_oc^2$ as $\gamma$ becomes large.

In 1929 Klein and Nishina$^{62)}$ developed a more sophisticated theory for the Compton effect, based on the Dirac electron formalism. They calculated the differential collision cross section for unpolarized photons incident upon nonaligned electrons to be

$$d\sigma = \frac{r_o^2}{2}\, d\Omega \left(\frac{\nu'}{\nu}\right)^2 \left(\frac{\nu}{\nu'} + \frac{\nu'}{\nu} - \sin^2\theta\right) . \qquad (2.49)$$

In this expression $d\Omega$ represents the solid angle $2\pi\sin\theta d\theta$. Equation (2.49) can be expressed in terms of $\gamma$ and $\theta$ by using equation (2.46). The result is

$$d\sigma = r_o^2\, d\Omega \left[\frac{1}{1+\gamma(1-\cos\theta)}\right]^2 \left(\frac{1+\cos^2\theta}{2}\right)\left\{1 + \frac{\gamma^2(1-\cos\theta)^2}{(1+\cos^2\theta)(1+\gamma(1-\cos\theta))}\right\}. \tag{2.50}$$

The differential scattering cross section can be obtained, through equations (2.44) and (2.46), by raising the factor in the first set of brackets of either equation (2.49) or equation (2.50) to the third power instead of the second. The differential absorption cross section can also be expressed by using equations (2.45), (2.49) and (2.50). A polar plot of $d\sigma/d\Omega$ for several photon energies is given in figure 2-4 to show how the number of photons scattered into a solid angle $d\Omega$ varies with photon energy and angle of deflection. It is clear that the distribution is almost symmetric about 90° for gamma rays of 0.01-MeV energy, as one would expect for low energy Thomson scattering, but quickly becomes peaked in the forward direction as energy increases.

The total collision cross section can be calculated as

$$\sigma = \int d\sigma \tag{2.51}$$

$$= 2\pi r_o^2\left\{\left(\frac{1+\gamma}{\gamma^2}\right)\left[\frac{2(1+\gamma)}{1+2\gamma} - \frac{\log(1+2\gamma)}{\gamma}\right] + \frac{\log(1+2\gamma)}{2\gamma} - \frac{(1+3\gamma)}{(1+2\gamma)^2}\right\}. \tag{2.52}$$

The total scattering cross section can also be calculated as

$$\sigma_s = \pi r_o^2\left[\frac{\log(1+2\gamma)}{\gamma^3} + \frac{2(1+\gamma)(2\gamma^2-2\gamma-1)}{\gamma^2(1+2\gamma)^2} + \frac{8\gamma^2}{3(1+2\gamma)^3}\right], \tag{2.53}$$

and the total absorption cross section found by subtracting equation (2.53) from equation (2.52).

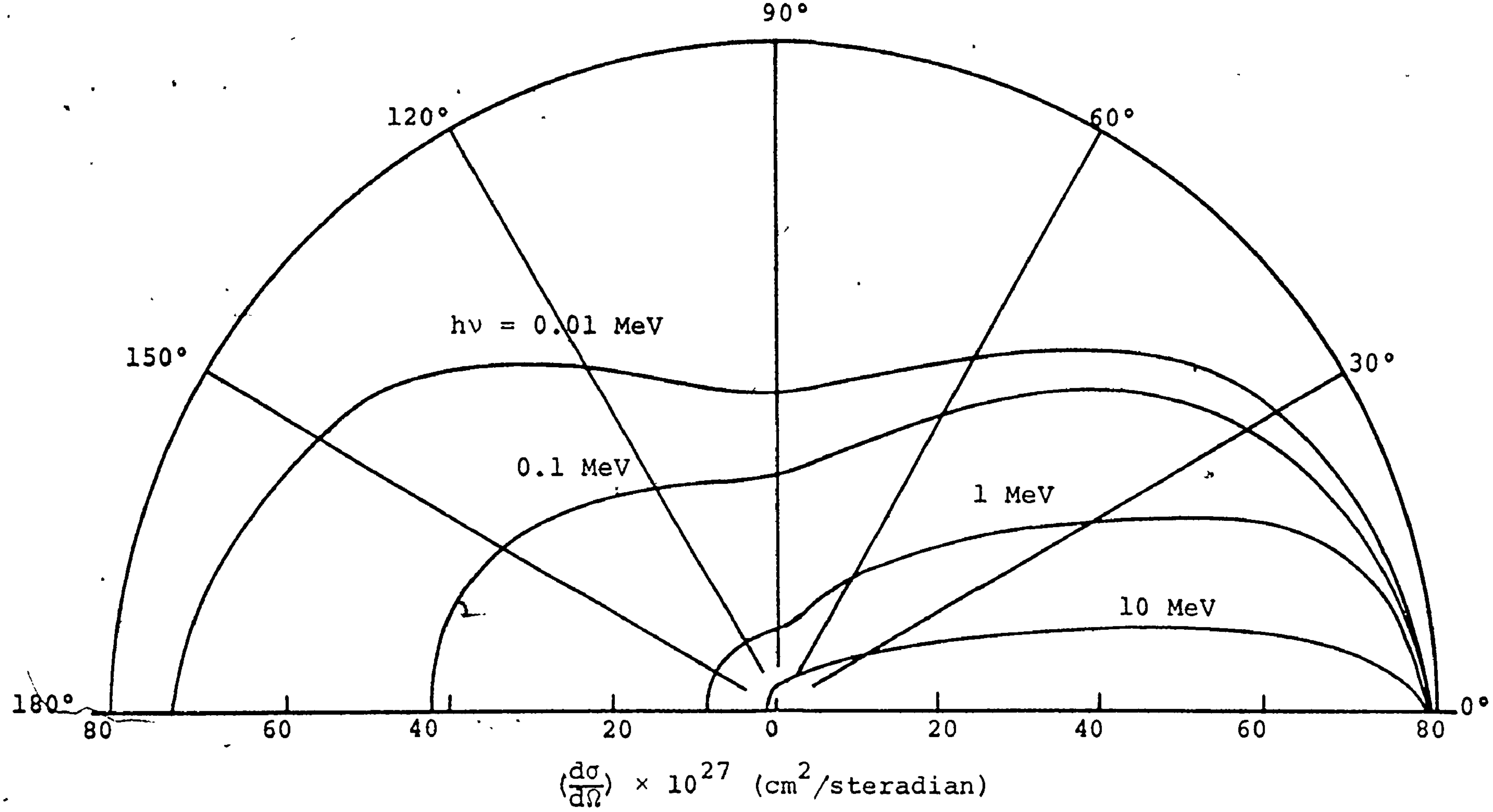

FIG. 2-4 PLOAR PLOT OF COLLISION DIFFERENTIAL CROSS SECTION

By further manipulation, the distribution in the number of Compton electrons per unit kinetic energy can be shown to be

$$\frac{d\sigma}{dT} = \frac{\pi r_o^2}{\gamma^2 m_o c^2}\{2 + (\frac{T}{h\nu - T})^2 [\frac{1}{\gamma^2} + \frac{(h\nu - T)}{h\nu} - \frac{2}{\gamma}(\frac{h\nu - T}{T})]\} . \quad (2.54)$$

The numerical evaluation of $d\sigma/dT$ is shown plotted in figure 2-5 against T, for various values of $h\nu$. Amongst the several characteristics of these curves one can list a small maximum at zero kinetic energy, a large maximum corresponding to the maximum kinetic energy ($T_{max}$), and a minimum at a value of $T \leq 0.5\ T_{max}$. As mentioned previously, $T_{max}$ is always less than the associated $h\nu$. The complementary energy distribution for scattered photons can be found by applying equation (2.47) to equation (2.54).

## 2.4 THE NaI(Tl) DETECTOR

The main component of this detector is the inorganic scintillator of sodium iodide. Thallium is included to reduce the trapping of light within the scintillator. When gamma radiation of intermediate energy is incident upon the scintillator it interacts with the material in accordance with the three interaction types just discussed. The contributions due to these effects are evidenced in figure 2-6 which shows a measured energy spectrum typical of the interaction of 2-MeV photons with the sodium iodide crystal. For comparison, the idealized response has been included. The large peak at 2 MeV is due to the photoelectric effect in which a vacancy is created in the K shell, followed by characteristic Xrays or

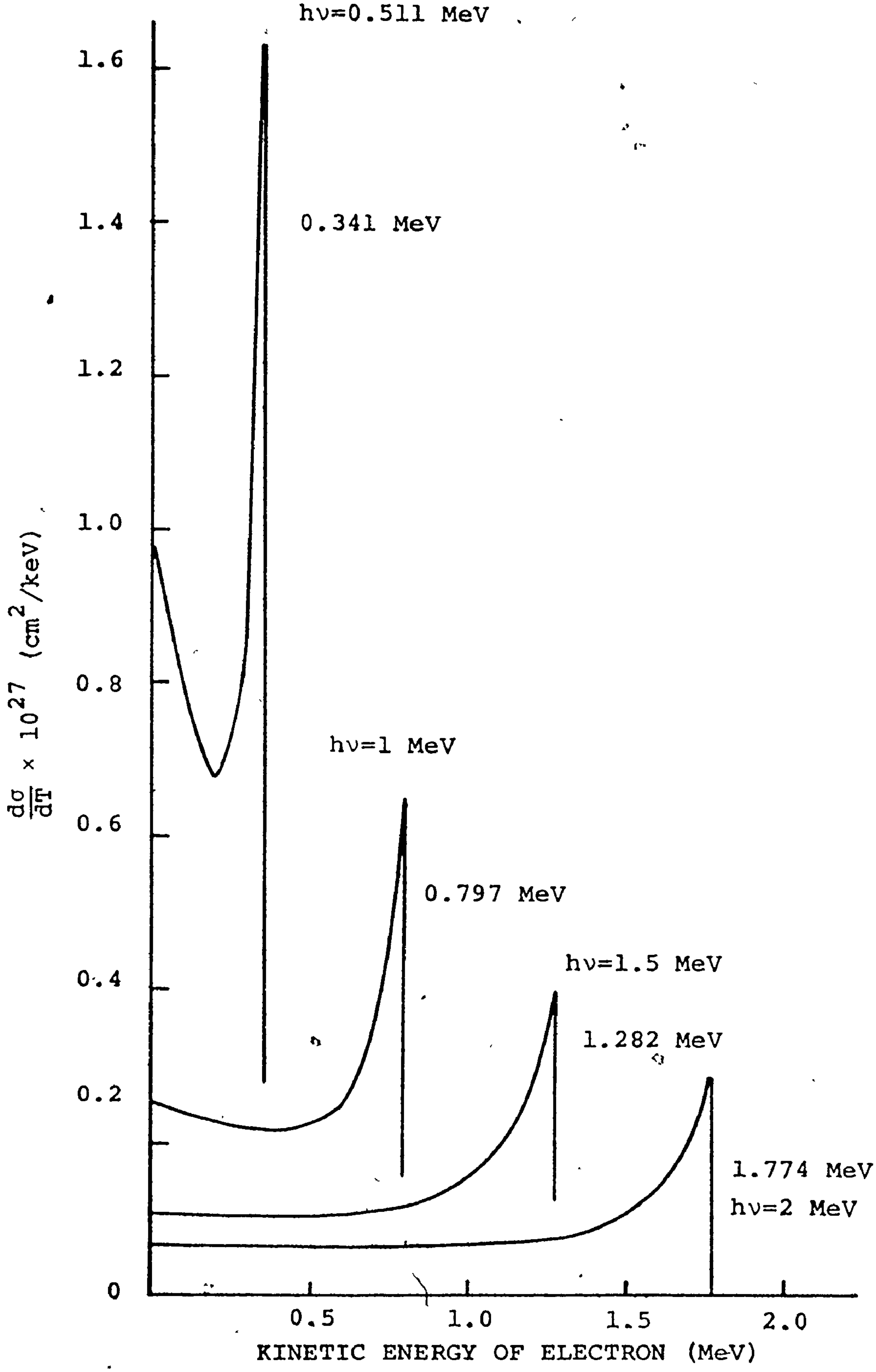

FIG. 2-5 RECOIL ENERGY DISTRIBUTION OF COMPTON ELECTRONS

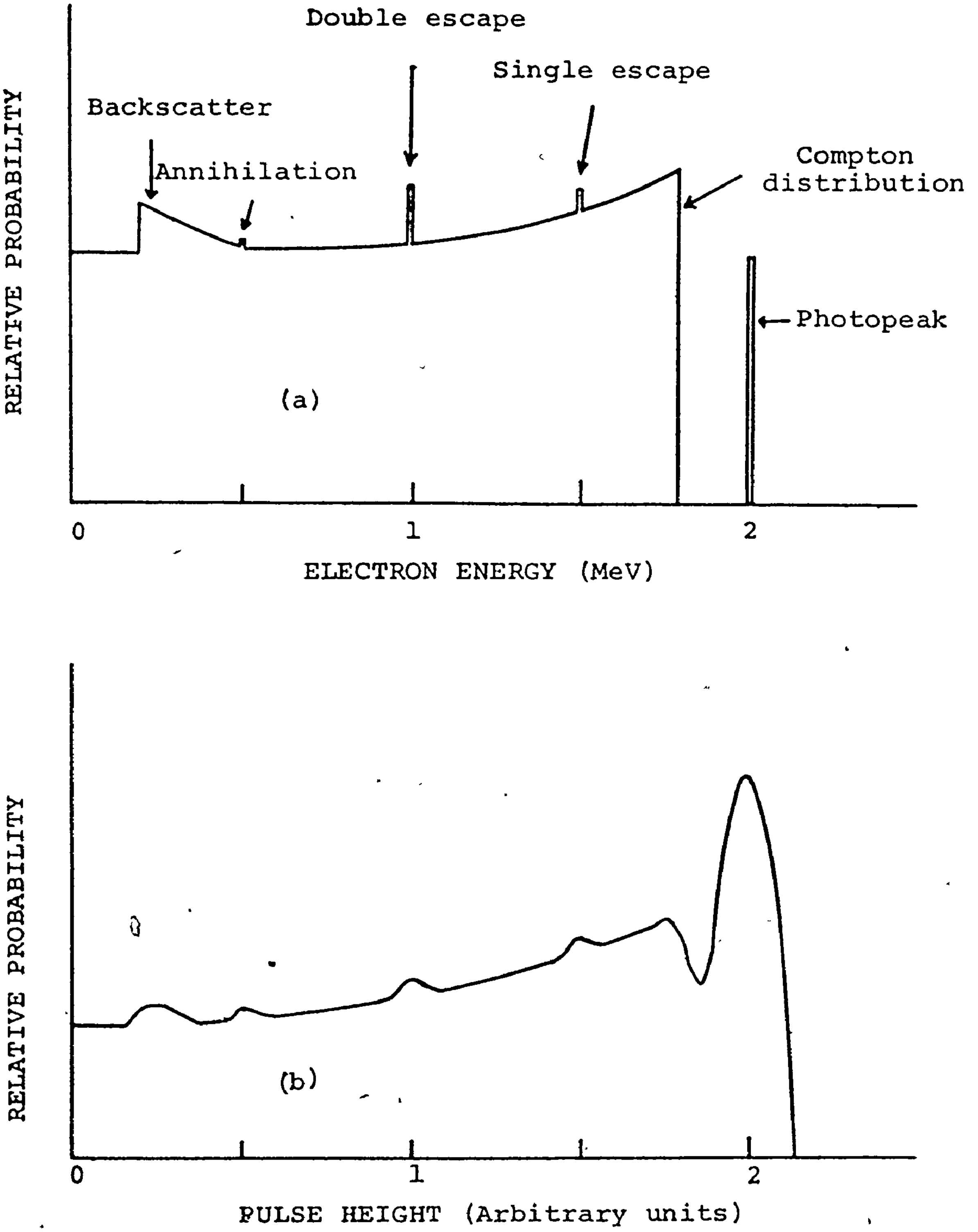

FIG. 2-6 RESPONSE OF NaI(Tl) DETECTOR TO 2-MeV GAMMA RAYS (a) Idealized electron energy distribution without multiple Compton scattering. (b) Observed response for 3-inch NaI(Tl) detector.

Auger electrons. The Xrays can easily be reabsorbed in other photoelectric collisions thus ensuring the containment of practically all of the incident energy. The photopeak so formed is fairly large because the interaction is primarily with the iodine content which has a high atomic number. It should be recalled from equation (2.17) that the photoelectric effect shows a $Z^5$ dependence. However, figure 2-6 also illustrates that there are many events in which energy is lost from the crystal. These are due to the pair interaction and the Compton effect. The former is evidenced in the two peaks at 1.489 MeV and 0.978 MeV. These peaks are representative of the escape of annihilation quanta. When the positron of the pair eventually slows down and annihilates with an electron two gamma rays each of energy $m_oc^2$ are emitted. Should one of these quanta escape, the contained energy would then peak at 2 MeV-$m_oc^2$ or 1.489 MeV. Similarly should both annihilation quanta escape, one would expect a peak at 2 MeV-$2m_oc^2$. The remaining energy loss features in figure 2-6 are solely due to Compton events. In these events it is possible for a gamma ray to scatter from a free electron thus delivering energy to the crystal. Not all of the photon energy is delivered to the crystal since the scattered radiation may escape. The energy distribution of the Compton electrons has already been discussed in conjunction with figure 2-5. The fairly flat portion of the observed spectrum is readily attributable to these Compton electrons. The gap between the high-energy Compton edge and the photopeak is then understandable in terms of the maximum kinetic energy achievable by a Compton electron being of order 1.8 MeV. The wide, low-energy, peak remaining can be explained as arising from Compton events external to the crystal. These events are seen to scatter radiation of consequently lower energy back into the crystal. The major contributions to this backscatter peak come from large angle scatterings which have a minimum energy of order 0.2 MeV for 180° deflections.

Basically an NaI(Tl) detector consists of an NaI(Tl) scintillator, a photocathode, and a photomultiplier. Light created in the de-excitation of the crystal falls on the optically coupled photocathode where primary electrons are ejected. These primary electrons are then accelerated before striking a dynode where secondary electrons are emitted. The secondary electrons then strike another dynode causing more secondary electrons to be emitted. This procedure continues through several dynode stages until the electrons strike the anode where the current is integrated and a voltage pulse obtained by means of a charge-sensitive preamplifier. Since the multiplication factor at each dynode increases with the kinetic energy of the incident electrons, the overall gain varies greatly with voltage. The final output is, however, proportional to the intensity of light received by the photocathode over a wide range of photomultiplier gains. The integration constant ($\tau = RC$) is usually chosen to be a few times larger than the decay time of the phosphor ($\sim$ 250 nanoseconds) if one wishes to have maximum pulse height. Maximum pulse height normally achieves best resolution since statistical variations decrease with increasing pulse height. However, although one prefers to have a good signal to noise ratio, it is also desirable to keep $\tau$ small in order to be dealing with reasonably narrow pulses.

## 2.5 INTERACTION OF ELECTRONS AND POSITRONS WITH MATTER

When charged particles such as electrons and positrons interact with matter they do so through Coulombic forces. The resultant interactions can be characterized as falling into four distinct groupings:

1. elastic collisions with nuclei,
2. inelastic collisions with atomic electrons,
3. inelastic collisions with nuclei,

and 4. elastic collisions with electrons.

The first group listed involves the deflection of electrons by nuclei, with only a minimal energy loss to the massive nucleus. The second group describes those interactions in which orbital electrons become sufficiently excited to cause ionization, or to at least enter a higher energy state. The third type of collision results from the emission of a quantum of radiation by an electron undergoing a deflection. Collisions of the fourth type listed are only significant for projectile electrons of energy less than 100 eV. This is due to the requirement that the energy delivered to the target electrons be less than the lowest excitation potential. However, all four types are involved in the complete stopping of an energetic electron. This is normally accomplished through a large number of chance encounters with nuclei and electrons (eg. a 1-MeV particle may experience ∿ $10^4$ collisions[63)]). The actual energy dimunition in any one encounter may range from the practically zero loss experienced in an elastic collision with a nucleus to the complete loss possible for an inelastic interaction with a nucleus. Thus the tortuous path of the electron and the associated energy decrements are best described in a probabilistic fashion. Experimentally measured quantities such as electron ranges are then seen as statistical averages.

### 2.5.1 ELASTIC COLLISIONS WITH NUCLEI

In the Coulombic scattering of electrons by nuclei, the electrons may undergo large deflections without losing any significant amount of recoil energy to the nuclei involved. Although the loss per collision is small, the probability of this process occurring is large, resulting in a substantial relative dimunition of energy by the accumulative effect of such scatterings.

The classical analysis of elastic scattering stems from the work of Rutherford[64)]. His formulation, when updated by Darwin[65)] to include the relativistic electron mass, is stated as

$$\sigma_R = \frac{r_o^2 \, Z^2}{4} \left(\frac{1-\beta^2}{\beta^4}\right) \csc^4\left(\frac{\theta}{2}\right) . \qquad (2.55)$$

Here θ represents the angle of deflection of the electron and

$\sigma_R$ stands for $d\sigma/d\Omega$.

The quantum-mechanical approach to elastic scattering has been taken by Mott(66) who obtained a conditionally convergent infinite series to represent the cross section. Probably the best simplification of Mott's infinite series is that attributed to McKinleyand Feshbach(67) who expressed the cross section in terms of the Rutherford formula as

$$d\sigma = \sigma_R[1-\beta^2\sin^2(\tfrac{\theta}{2})+\pi\beta\,\frac{Z}{137}\,(1-\sin(\tfrac{\theta}{2}))\sin(\tfrac{\theta}{2})]d\Omega. \quad (2.56)$$

The constraints of validity are that $\beta$ should be of order unity, and that $Z/137$ should be no greater than 0.2 in value. The latter condition implies that the equation holds for $Z \leq 26$. The exact series of Mott has been evaluated numerically by McKinley and Feshbach for $Z > 26$. The factor in the square brackets of equation (2.56) represents the nonclassical effect of the intrinsic spin of the electron. Additionally, positron scattering can be described in theory by simply replacing $Z$ by $-Z$.

As the electron path within a material is increased there is an increasing probability of getting more than the single scatterings described above. When the target is sufficiently great to permit many scatterings the effect is known as multiple scattering. This is most commonly experienced in practice, and, although complicated, can be treated statistically.

A good review of multiple scattering theories to date, and the effects of screening, is provided by Roy and Reed(68).

## 2.5.2 INELASTIC COLLISIONS WITH ELECTRONS

The predominant method for an energetic electron to lose energy in matter is through inelastic collisions with atomic electrons since the effective energy transfer can be large if the target particle is of comparable mass. The energy is lost through excitation and ionization of atoms. The kinetic energy of the incident electron is therefore taken to be much greater than the binding energy of the orbital electrons. If the incident particle has much energy to lose, many inelastic encounters will be required and of course, following possible ionization, the ejected or secondary electrons may have sufficient energy to cause further excitations or ionizations. Also, the scatterings involved will be in the forward direction since for particles of equal mass the maximum angle of deflection is $\theta_{max} = \pi/2$ and, for a nonrelativistic collision if one particle is scattered at an angle $\theta$ the other must necessarily be found at an angle of $\frac{\pi}{2} - \theta$. With the above in mind it is easy to comprehend the nonrelativistic formula developed by Mott[69)] to correct the classical concepts of Rutherford for quantum-mechanical effects. He obtained

$$\left(\frac{d\sigma}{d\Omega}\right)_{Mott} = \frac{r_o^2}{\beta^4}\left[\csc^4\theta+\sec^4\theta-\csc^2\theta\sec^2\theta\cos\left(\frac{\alpha}{\beta}\,\ln(\cot\theta)\right)\right]. \qquad (2.57)$$

The first two terms can be seen from equation (2.55) to be Rutherford type terms for two identical particles whose angles of deflection are complementary. The third term, which is purely quantum-mechanical, is due to the operation of the Pauli exclusion principle for indistinguishable particles. Such collisions between identical particles are often referred to as Møller collisions since Møller[70] developed the theory for them under the condition of relativistic invariance. His extensive equation for the cross section will not be included in this work.

However, since the magnitude of the energy lost in each collision is of primary importance, the differential cross sections are better expressed in terms of the energy, Q, transferred to the struck particle. For instance the classical Rutherford cross section for an incident electron of kinetic energy T and velocity v to lose energy Q to a stationary electron is

$$d\sigma = \frac{2\pi e^4}{m_o v^2} \frac{dQ}{Q^2} . \qquad (2.58)$$

Due to the inverse-square variation of dσ with Q, it is evident that soft collisions in which small amounts of energy are transferred are extremely frequent compared to those in which Q is large. Since it is impossible to distinguish the particles in an electron-electron collision, the faster of the two after the collision is assumed to be the incident particle. Thus Q is restricted to a maximum value of T/2, and the cross section is seen as the sum of two components. This gives rise to the classical equation

$$d\sigma = \frac{2\pi e^4}{m_o v^2} \left[\frac{1}{Q^2} + \frac{1}{(T-Q)^2}\right] dQ. \qquad (2.59)$$

Once again a more correct expression is available from the quantum-mechanical calculations of Møller who includes spin, relativity, and exchange effects. Bhabha[71)] has treated the corresponding problem for incident positrons by replacing the exchange effect by a virtual annihilation effect, and omitting the Pauli exclusion principle which was no longer applicable.

A useful concept in energy loss analyses is that of stopping power which is defined as the average energy loss per unit length of path through a material. If the material contains N atoms per unit volume, and Z electrons per atom, the stopping power is seen as

$$-\left(\frac{dT}{dS}\right) = NZ \int_{Q_{min}}^{Q_{max}} Q\, d\sigma. \tag{2.60}$$

Some idea of the form of the stopping power is achieved by using the classical cross section of equation (2.58) in the integration. The result is

$$-\left(\frac{dT}{dS}\right)_{classical} = \frac{2\pi e^4}{m_o v^2} NZ\, \ln\left(\frac{Q_{max}}{Q_{min}}\right). \tag{2.61}$$

Bethe and Bloch[72)] have worked out the stopping power formula in terms of the relativistic cross section of Møller. In the nonrelativistic region the representation reduces to the simple equation

$$-\left(\frac{dT}{dS}\right) = \frac{4\pi e^4}{m_o v^2} NZ\, \ln\left[\frac{m_o v^2}{I}\left(\frac{2.7182\cdots}{8}\right)^{1/2}\right], \tag{2.62}$$

where I is the geometric mean of all ionization and excitation potentials. This formula differs from one calculated previously by Bethe[73)], using Mott's nonrelativistic equation, by the inclusion of the square root factor in the logarithm.

It is worth noting that the stopping power is almost independent of Z but is dependent upon density. This is because NZ can be rewritten as $N_o \rho Z/A$ where $N_o$ is Avogadro's number and Z/A is practically constant for Z > 2. The only other possible Z dependence is one established through

$$I = I_o Z \ , \qquad (2.63)$$

where $I_o$ has been found experimentally[74)] to be 11±3 eV. However the effect is subdued somewhat in that it occurs logarithmically.

The equivalent development for positrons has been provided by Rohrlich and Carlson[75)] using the Bhabha cross section for distinguishable final ionization states. They indicate that the largest difference between the stopping powers for electrons and positrons (∿10%) occurs for $T << m_o c^2$, but that over a wide energy range the percentage difference in mean energy loss was quite insensitive to stopping material.

In the calculation of the preceding stopping powers, radiative losses have been assumed to be negligible. At high energies, $T >> m_o c^2$, radiative losses become comparable to ionization losses. Bhabha[76)] has provided the approximate ratio

$$\frac{(dT/dS)_{rad}}{(dT/dS)_{ion}} \approx \frac{TZ}{1400\ m_oc^2}. \tag{2.64}$$

It is therefore evident that the radiative stopping power increases to equal the ionization stopping power when T has increased to approximately 9 MeV in lead (Z=82) for example. Proportionately higher energies are required for materials of lower atomic number.

### 2.5.3 INELASTIC COLLISIONS WITH NUCLEI

Electrons may lose energy in collisions with nuclei via nuclear excitation and bremsstrahlung emission but by far the more significant is the radiative process. Clasically, the energy intensity of this radiation is dependent upon the square of the acceleration of the particle as it is deflected by the nucleus. Since the force involved is Coulombic, one can write, for a particle of unit charge,

$$I \propto a^2 = \frac{Z^2e^4}{m^2}, \tag{2.65}$$

from which it is obvious the bremsstrahlung is most significant for light particles such as the electron and positron, and, that the sign of the charge is unimportant. The energy carried away by the radiated photon can vary continuously up to a maximum$^{77)}$ of the complete kinetic energy T of the electron.

Once again quantum mechanics must be brought to bear on this interaction. The main qualitative difference between this description and that of classical theory is that whereas classical physics requires that all electron-nucleus collisions be accompanied by emission of a photon, quantum mechanics predicts only a small probability of radiation. However, when the many low energy photons of the classical picture are replaced by the few photons of relatively higher energy in the quantum-mechanical view, the ensemble average remains approximately the same, and the cross sections are both of order $\alpha r_o^2 Z^2$.

Many cross section formulae have been developed to describe bremsstrahlung production by electrons in so called thin targets. These targets are defined as being so thin that no appreciable energy is lost to ionization, no elastic deflections occur, and only one quantum of radiation is permitted during transit of the target. An excellent summary of these formulae and a discussion of their validity has been published by Koch and Motz 78).

For energetic electrons, it is unfortunately necessary to use approximations, the simplest being that of Born. Also one must take into account screening by atomic electrons. This effect can be considerable since the main contribution to the radiative process occurs at roughly the rationalized Compton wavelength (∿ $385\times10^{-13}$ cm), and greater. The influence is greatest at high electron energies.

Bethe and Heitler 79) have developed pertinent theory by using the Dirac relativistic electron and the Born expansion for the Coulomb interaction. The effect is treated as a perturbation in which the electrons interact with both the Coulomb field of the nucleus and the radiation field of the photons. For the highly relativistic case without screening the expression amounts to

$$d\sigma_{rad} = \frac{4Z^2 r_o^{\,2}}{137} \frac{d(h\nu)}{h\nu} [1 + \frac{E_f^{\,2}}{E_i^{\,2}} - \frac{2E_f}{3E_i}] [\ell n (\frac{2E_i E_f}{h\nu m_o c^2}) - \frac{1}{2}] \, , \qquad (2.66)$$

where $E_i$ and $E_f$ are the initial and final electron energies, and the condition of validity is that $(E_i E_f / h\nu) << (137\ m_o c^2 / Z^{1/3})$. It is of interest to observe that the cross section, differential in photon energy, is inversely proportional to the energy of the emitted quantum. The total radiation cross section can be determined from the definition of

$$\sigma_{rad} = \int_{h\nu=0}^{h\nu=T} \frac{h\nu}{E_i} d\sigma_{rad} \qquad (2.67)$$

to be

$$\sigma_{rad} = \frac{4Z^2 r_o^{\,2}}{137} [\ell n (\frac{2E_i}{m_o c^2}) - \frac{1}{3}] \, . \qquad (2.68)$$

Because of the breakdown of the Born conditions for materials of high Z a new approach was necessary. The work of Bethe, Maximom, Davies and Olsen$^{80)}$ for electrons with $T >> m_o c^2$ led to a particularly simple correction to the formulae of Bethe and Heitler. For instance one need only include a correction term f(Z) in the final square brackets of equations (2.66) and (2.68). For low and high Z materials the correction term can be approximated as 1.20 $\alpha^2 Z^2$ and 0.925 $\alpha^2 Z^2$ respectively. Additional extensions to the above work as well as considerations of cross sections near the high frequency limit are also available[81)].

The stopping power by bremsstrahlung production can now be calculated from the definition

$$-\left(\frac{dT}{dS}\right) = N \int_{h\nu=0}^{h\nu=T} h\nu \, d\sigma_{rad} . \tag{2.69}$$

Simple substitution and integration leads to

$$-\left(\frac{dT}{dS}\right) = N(T+m_o c^2)\sigma_{rad} , \tag{2.70}$$

where $\sigma_{rad}$ is independent of $h\nu$. For highly energetic electrons meeting the condition $m_o c^2 << T << 137\ m_o c^2/Z^{1/3}$, one may virtually ignore the effects of screening and use $\sigma_{rad}$ as defined by equation (2.68).

It is of interest to note the qualitative features of the angular distribution of bremsstrahlung. Since the momentum of the incident electron is shared amongst the scattered electron, the nucleus, and the photon, the radiation quantum may carry off any momentum up a maximum of T/c. However, in general, the amount of momentum intrinsic to a photon ($h\nu/c$) is relatively tiny compared to that for a particle with identical energy. The photon can therefore be emitted in any direction. For low incident electron velocities the maximum intensity of bremsstrahlung is found at a direction perpendicular to the plane of scattering. However at extremely relativistic energies of incidence the consequently higher-energy photons may carry momentum comparable to that of an electron, with the result that the radiation distribution tends to be strongly peaked in the forward direction. This can be approximately expressed[82] in terms of an average angle with respect to the direction of incidence as

$$\langle\theta\rangle \approx \frac{m_o c^2}{T} \ . \tag{2.71}$$

Several sources[81] are available for further discussion of angular distributions.

Finally, one must give consideration to the possible production of bremsstrahlung by an electron in the field of another electron. Although the effect is complicated by the possible exchange nature of the process, it is often adequately included by writing $Z(Z+1)$ instead of $Z^2$ in the nuclear cross sections. This procedure may be insufficiently accurate in materials of low $Z$. A summary of electron-electron bremsstrahlung has been provided by Joseph and Rohrlich[83] who indicate that, for extreme relativistic velocities and free electrons, the radiation cross section can be expressed as

$$\sigma'_{rad} = \frac{4r_o^{\,2} Z}{137}\left[\ell n\left(\frac{2E_i}{m_o c^2}\right) - \frac{4}{3}\right] \ . \tag{2.72}$$

Since the prime difference between this and equation (2.68) for nuclear bremsstrahlung is in having $Z$ instead of $Z^2$, one can write the total cross section in terms of the nuclear cross section by replacing $Z^2$ by $Z(Z+\delta)$. The additive term, $\delta$, given by

$$\delta \doteq \frac{[\ln(\frac{2E_i}{m_oc^2}) - \frac{4}{3}]}{[\ln(\frac{2E_i}{m_oc^2}) - \frac{1}{3}]}, \qquad (2.73)$$

amounts to 0.49 for an incident energy of $5m_oc^2$, 0.96 for 50 $m_oc^2$, and unity for infinite energy. However, the above treatment has avoided the influence of atomic binding. When this is taken into account, for extreme relativistic velocities and complete screening, a new additive constant $\Delta$ must be defined as

$$\Delta = \frac{\ln(530/Z^{2/3})}{\ln(183/Z^{1/3})+1/18}. \qquad (2.74)$$

This new constant varies with atomic number and can be evaluated as 1.04 for magnesium (Z=12) to 0.88 for lead (Z=82).

### 2.5.4 THICK TARGET CONSIDERATIONS

Since thin targets are rarely met in practice account must be taken of the effect of many elastic collisions and many ionizations. These processes of energy degradation greatly influence the production of bremsstrahlung. In calculating the intensity of energy radiated one cannot merely integrate over the radiative stopping power but must instead regard it in the context of a fractional component of the total stopping power. Fortunately equation (2.64) indicates that often the total stopping power can be represented solely by that due to ionization. The energy intensity can therefore be approximated by

$$I \approx \int_0^T \frac{(dT/dS)_{rad}}{(dT/dS)_{ion}}\, dT \qquad (2.75)$$

which, via equation (2.64), reduces to the form

$$I = kZT^2 \, . \qquad (2.76)$$

A variety of experimental and theoretical evaluations$^{84)}$ has led to the estimation of k as $(0.7 \pm 0.2) \times 10^{-3}$, when T is expressed in MeV. The efficiency of bremsstrahlung production is then given, as the fraction of input kinetic energy appearing as radiation, by

$$\varepsilon = kZT \, . \qquad (2.77)$$

Because this equation leads to efficiencies in excess of 100% at highly relativistic energies, the expression is often reformed as $^{85)}$

$$\varepsilon = \frac{kZT}{1+kZT} \, . \qquad (2.78)$$

The energy distributions of bremsstrahlung from electrons of intermediate and nonrelativistic energies have been described theoretically with reasonable success. If energy spectra are collected at various angles it is found$^{78)}$ that the relative number of high-energy photons increases with decreasing angle, a behaviour opposite to that predicted for thin targets. The actual shape of bremsstrahlung spectra integrated over all angles has been estimated by Kramers$^{86)}$ on the basis of a thick target being composed of many thin targets. He obtained the equation

$$dI = \text{constant}\times Z\ (\nu_{max}-\nu)\,d\nu \qquad (2.79)$$

which has met with surprising success despite its extreme simplicity.

At intermediate and nonrelativistic kinetic energies no analytic formula exists to describe the angular distribution of bremsstrahlung in thick targets. Experimentally the distribution is greatly dependent upon geometry since a complex of attenuations of photon flux is involved. One of the few reports of data corrected for photon absorption is provided by Buechner et al$^{87)}$ who studied electrons of kinetic energies ranging from 1.25 MeV to 2.35 MeV impinging upon thick targets of beryllium (Z=4) and gold (Z=79). Basically they found that the angular distributions were predominantly peaked in the forward direction, with the beryllium distribution considerably more so than that of gold.

Much of the above is substantiated by the recent experimental investigations of thick target bremsstrahlung by Dance$^{88)}$ and his coworkers. They studied targets of beryllium, aluminum, tin, and gold each being thicker than the respective electron ranges associated with incident electrons of particular kinetic energies between 0.2 MeV and 2.8 MeV. Data were collected for a variety of angles extending from 0° to 150° but were not corrected for photon absorption. They found the total integrated intensity to be closely related to the square of the kinetic energy as expected from equation (2.76), the average power being 2.01. The total intensity also appeared to be linearly dependent upon Z with k varying from $0.3\times10^{-3}$ to $0.38\times10^{-3}$. Application of the aluminum and iron data to the efficiency equation (2.77) revealed the relationship

$$\varepsilon(T) = (0.36\pm0.04)\times10^{-3}\ ZT^{(1.00\pm0.13)} \qquad (2.80)$$

It should be remembered that since the data were indicative of external bremsstrahlung the constant k should be somewhat larger in describing internal bremsstrahlung.

The angular distributions (dI/dΩ) of Dance tend to be very similar for all targets bombarded by electrons of the same energy, but the widening of the distributions with increasing Z agrees in trend with that noted by Buechner$^{87)}$. As bombardment energies are increased the distributions become strongly peaked towards small angles with greater than 80% of the intensity from photons of energy greater than 0.5T being found in the forward directions.

In the intensity versus photon energy graphs of Dance it is found that for identical incident energies the data curves tend to parallel each other, except in the low energy region where attenuation is significant. Since the graphs are plotted on log-linear scales the constancy of differences is indicative of the functional relationships being closely similar, but for different multiplicative constants.

Finally, the complications associated with the very many collisions suffered by electrons in losing energy in a thick target, and the subsequent large statistical fluctuations in the energy dimunition process, can often by avoided through the concept of electron range. If a beam of monoenergetic electrons is incident upon a target the number of transmitted electrons decreases with increasing target thickness. A typical illustration of this is shown in figure 2-7. The shape of the curve at small thicknesses is dependent upon the particular experiment conducted 89). However, irrespective of the experimental conditions, as the transmission falls off with increasing thickness two notable features are encountered. These are a long tail due to electron straggling which gradually is masked by background statistics, and a fairly linear portion just previous to the onset of the tail. The target thickness obtained by extrapolating the linear portion to intersect the background level is then known as the extrapolated range for electrons of the particular energy used. Katz and Penfold 90) have proposed empirical formulae to describe the variation of electron range in aluminum with energy. They have suggested the equations

$$R = 412\ T^{n}, \tag{2.81}$$

where

$$n = 1.265-0.095\ \ell n\ T \tag{2.82}$$

for energies between 0.01 and 3 MeV, and,

$$R = 530T-106 \tag{2.83}$$

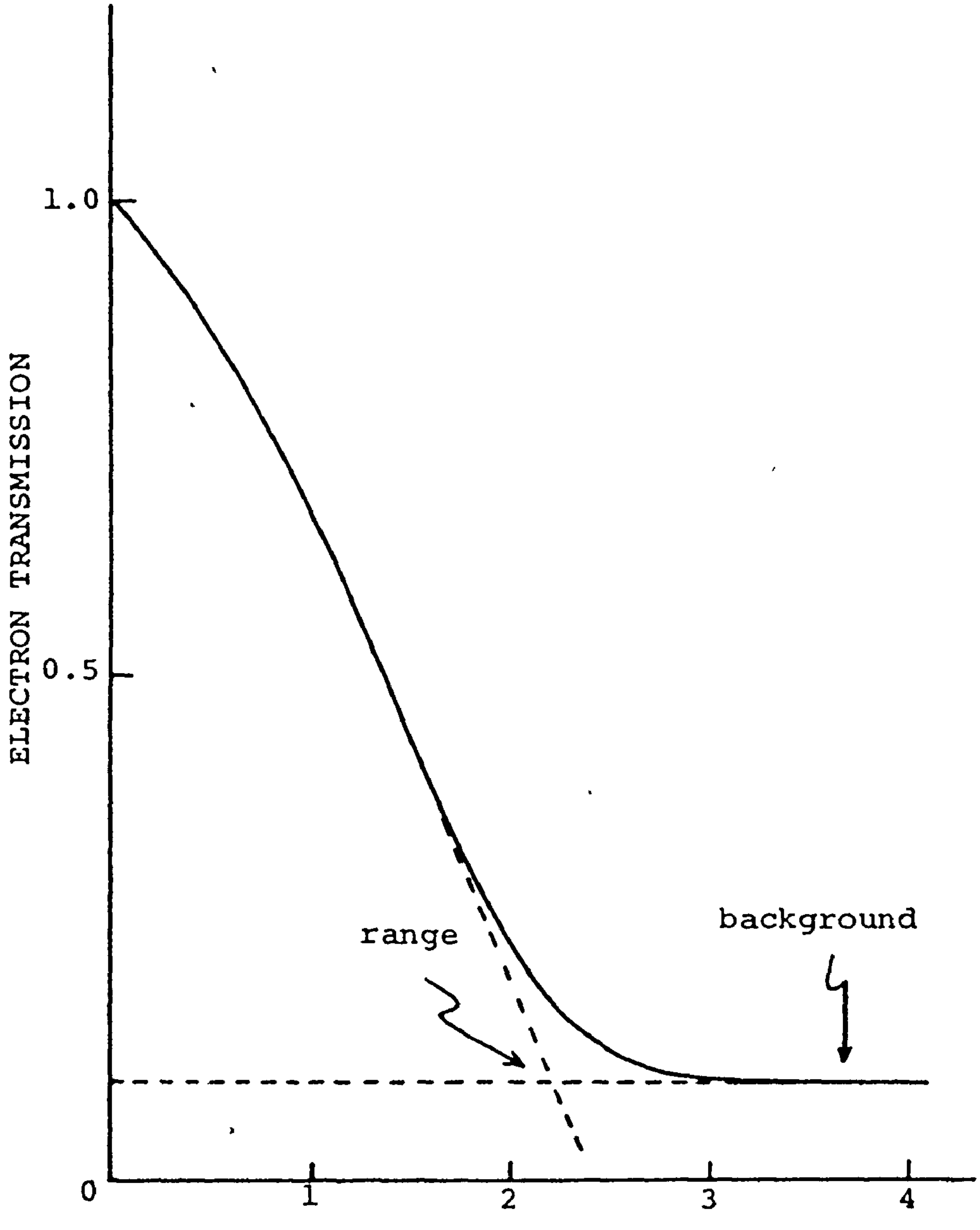

FIG. 2-7 ELECTRON RANGE VIA TRANSMISSION

for energies between 3 and 20 MeV. Application of equations (2.81) and (2.83) with T expressed in MeV will result in ranges expressed in $mg/cm^2$. These range equations are often taken as sufficiently accurate for many materials since stopping power is practically only dependent upon density. However, since a variation of range with atomic number does exist the theoretical compilations of Nelms91) and Berger and Seltzer92) may be more appropriate.

# CHAPTER III

# EXPERIMENTAL PLANNING

## 3.1 INTRODUCTION

In designing an experiment to measure double pair production one must keep in mind that the cross section for the process has been projected theoretically as being extremely small compared to that for single pair production ($\sigma_{\pi\pi}/\sigma_{\pi} \sim 10^{-5}$), and, that two electron-positron pairs may also be produced by the cascade process discussed in Chapter I.

The basic experimental requirements necessitate a suitable choice of

a) source,

b) detection system,

and c) targets.

The source of gamma rays must be strong in order to ensure a high flux incident upon the targets and thus avoid unrealistically long periods of data collection. The beam of gamma rays must be finely collimated to provide good geometry defintion, with its attendant simplification of analysis. Furthermore, the gamma rays should be sufficiently energetic to be well above the minimum energy requirement of 2.044 MeV for double pair production. Ideally, they should also be monoenergetic to avoid the unnecessary complication of introducing an energy dependence. Since the requirements of source strength and collimation could be met by the tangential irradiation facility of the McMaster Nuclear Reactor, it was decided to use an (n,γ) reaction to provide the beam of gamma rays. Specifically, thermal neutron capture in $^{48}$Ti was chosen since the capture cross section of 8.3±0.6 barns[93)] would lead to an intense beam of photons consisting predominantly of gamma rays of energy 6417.3, 6557.2 and 6761.7 keV[94)].

The decision to use the tangential irradiation facility was also influenced by the ready availability of an associated detection system suitable for detection of double-pair creations. The system, a quadrisected annulus of NaI(Tl), could be used with a target for γ-irradiation mounted axially within the annulus. The occurrence of a double-pair-creation event would then be determined by the coincident detection of 0.511-MeV photons, from annihilation of the two positrons, in all four of the quadrants.

The choices of source and method of detection were automatically accompanied by constraints on the targets to be used. Since detection of annihilation quanta would be required, a high efficiency for stopping positrons would be essential. Targets would have to be wider than the beam diameter of approximately 1 cm. and at least a few times longer than the maximum positron range. However, severe attenuation of the 511-keV photons could result from targets which were either too wide or overly dense. A compromise resulted in the choice of cylindrical targets with a diameter of 2.54 cm and a length of approximately 5 cm. Additionally, it was realized that targets should be both pure, to avoid misinterpretation of data, and low in atomic number, to minimize the effect of bremsstrahlung-cascade events (equation 1.18).

## 3.2 THE REACTOR FACILITY

The McMaster Nuclear Reactor is a light-water,enriched fuel, 5-MW, swimming-pool reactor. The configuration of the associated tangential irradiation facility, which has been described in depth by Nichol et al 95), is shown in figure 3-1. The system purposely parallels one face of the reactor core to avoid direct viewing of core gamma rays. The viewing of scattered core radiation is inhibited by the 10 cm-thick lead shield which covers the core face nearest to the external collimator. Additional shielding is provided by the internal collimator which is basically a lead annulus of length 23 cm, and inner and outer diameters of 3.8 cm and 15.2 cm respectively. The internal collimator is sealed at each end by an aluminum can containing a 3 mm-thick $^6$LiF disc which is used to remove thermal neutrons from the beam. The sample for irradiation is placed within an evacuated aluminum tube approximately 2 m in length and 7.6 cm outer diameter. The neutron flux at the source position is approximately $5\times10^{12}$ neutrons/cm$^2$/sec. The gamma radiation emitted by the source is then collimated towards the detection system by the external colli-

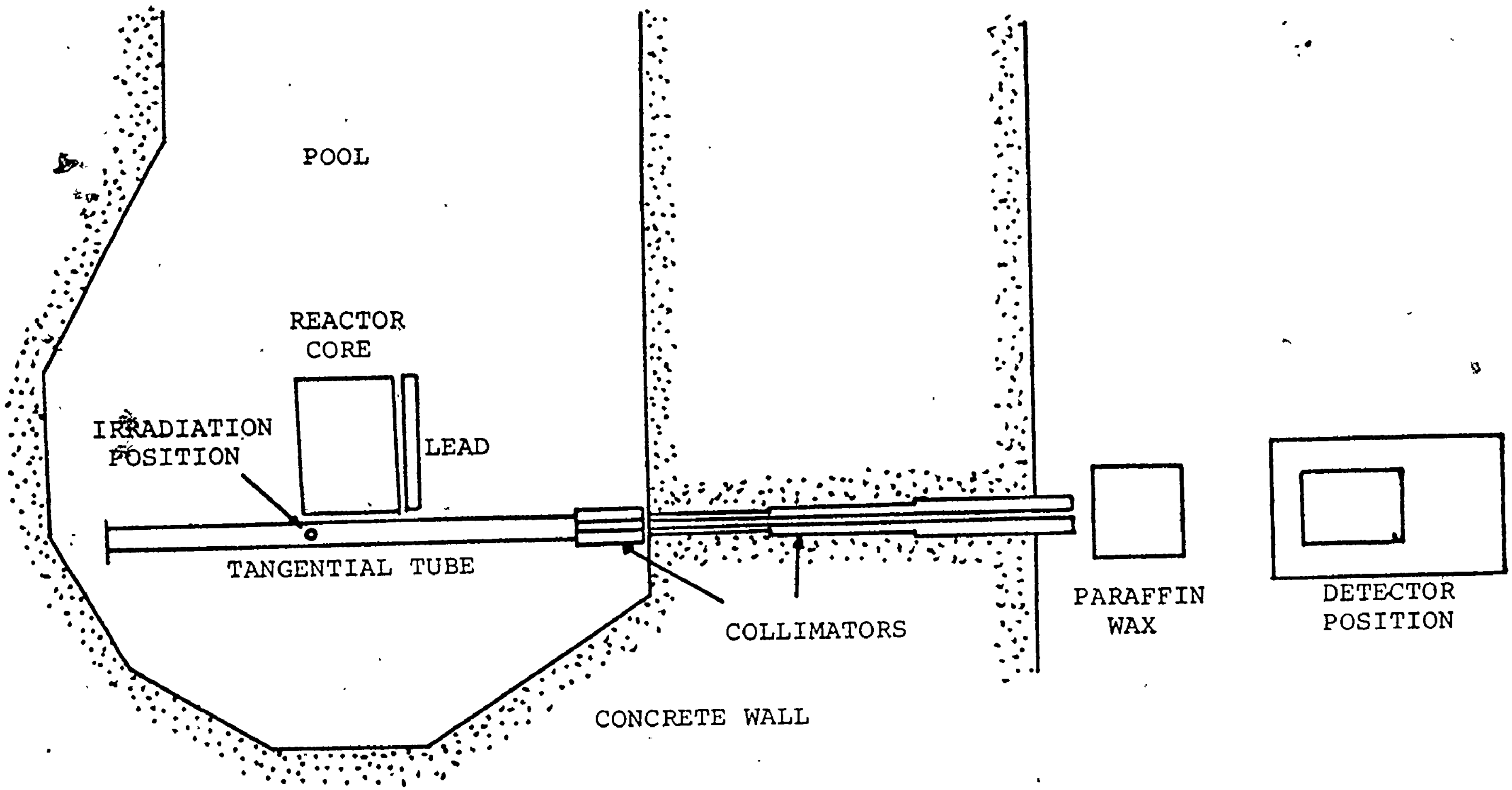

FIG. 3-1 TANGENTIAL IRRADIATION FACILITY

mator whose inner diameter is 0.83 cm and whose length is 1.9 m. The external collimator is separated from the pool by a 2.54-cm aluminum window locally-thinned to 0.6 cm in thickness. The collimator is stepped and is filled, but for the aperture, with lead and polyethylene shot to guard against streaming effects. The resultant solid angle subtended at the detection system by the source is of order $10^{-5}$ steradians. The beam is intercepted by approximately 30 cm of paraffin wax, positioned between the end of the collimator and the NaI(Tl) annulus, to remove any fast neutrons scattered into the collimation system by the source material.

The sample for irradiation is mounted in the tangential tube as illustrated in figure 3-2. The positioning straps, which are attached to both the end cap and the positioning ring, are used to maintain the sample towards the back of the core. Thus, at most, only large-angle scattered core radiation is permitted to enter the external collimator. The positioning ring, which has a small clearance with the inside of the evacuated tube, is used to centre the sample. The sample is suspended in a small holder made from a material innocuous to the particular intended investigation.

In the present work, a thin aluminum holder with open faces was chosen. The amount of aluminum present was reduced by boring many holes in the holder. A 5-gm titanium sample, cut from a rod of zone-refined natural titanium, was secured

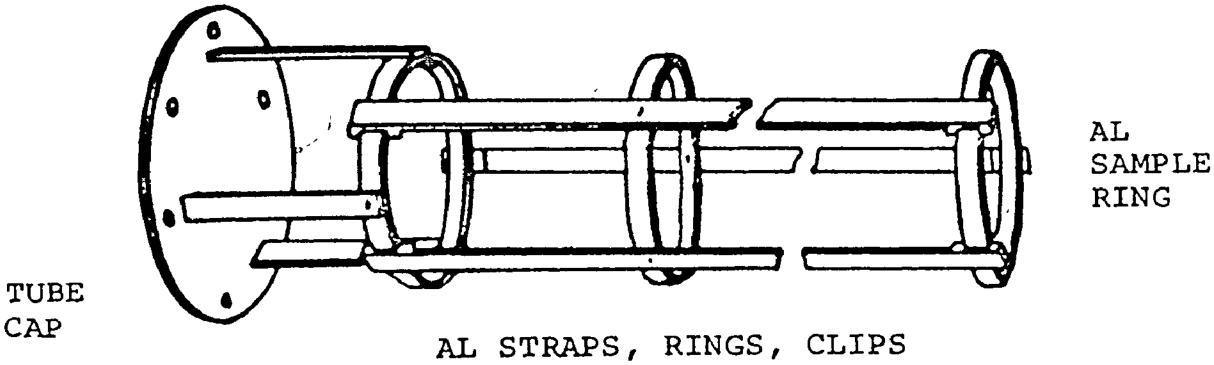

AL STRAPS, RINGS, CLIPS

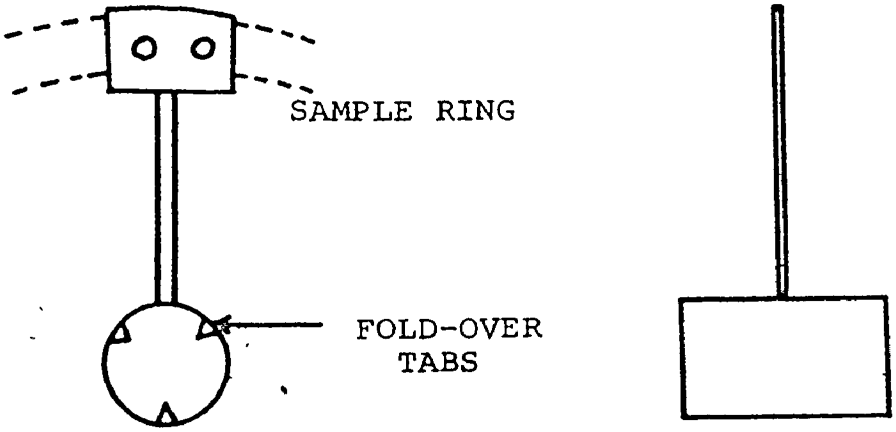

ALUMINUM SAMPLE CONTAINER

FIG. 3-2 SAMPLE POSITIONING

in position by fold-over tabs. Figure 3-3 shows the resultant gamma-ray spectrum collected at low reactor power using a 25 cc Ge(Li) spectrometer. The gamma rays of importance have an average energy of 6.6 MeV and account for roughly 70% of all thermal neutron captures[94)] in the natural target.

Since changes in reactor power, during the many months required for data-collection, were anticipated, it was decided to use barytes-concrete absorbers to regulate the gamma flux. More significantly however, the differences in reaction rate within the various targets could also be accommodated. The absorbers, which harden the beam by discriminating against gamma rays of low energy, were marked for ease of duplication of position. They were introduced between the end of the external collimator and the paraffin wax. The anticipated variation in gamma flux also demanded the use of a reliable flux monitor.

## 3.3 THE DETECTION SYSTEM

The NaI(Tl) annulus chosen as a detector system was manufactured by the Harshaw Chemical Company. The geometry of the system is illustrated in figure 3-4. The annulus consists of four optically isolated quadrants, each serviced by a 10-dynode photomultiplier tube. The annulus is 15.2 cm long, with inside and outside diameters 8.6 cm and 23.0 cm respectively. It is surrounded, but for the region of the photomultiplier tubes, by 5 cm of lead to shield against background radiation. A lead "nose-cone", 15 cm in length, and having an aperture 2.9 cm in diameter, is used to restrict the view at the annulus of

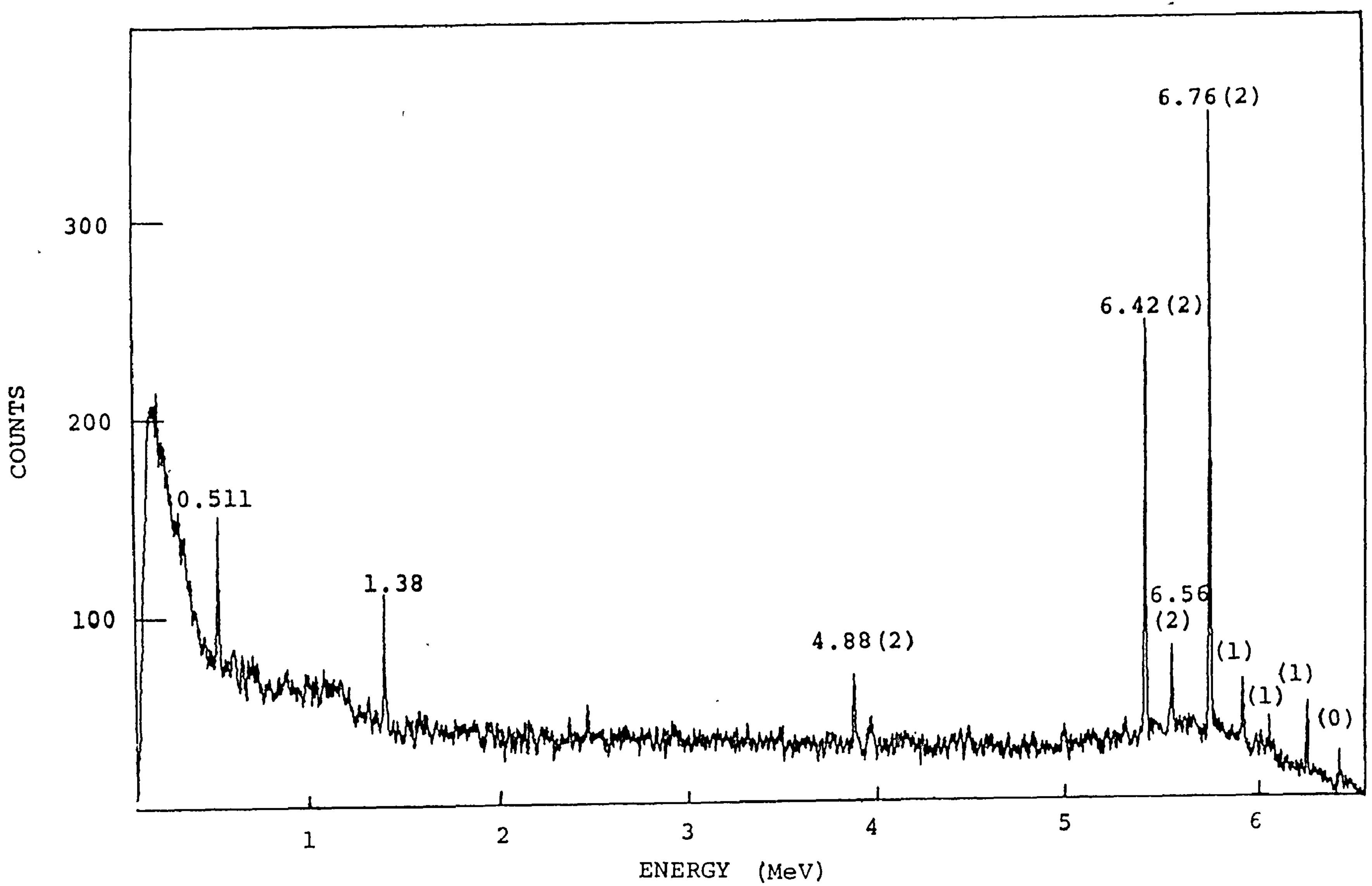

FIG. 3-3 Ge(Li) SPECTRUM FROM NEUTRON CAPTURE IN A NATURAL TITANIUM TARGET
The number of escaping annihilation quanta are shown in brackets. Data have been smoothed by means of a three-point rectangular fold-in function.

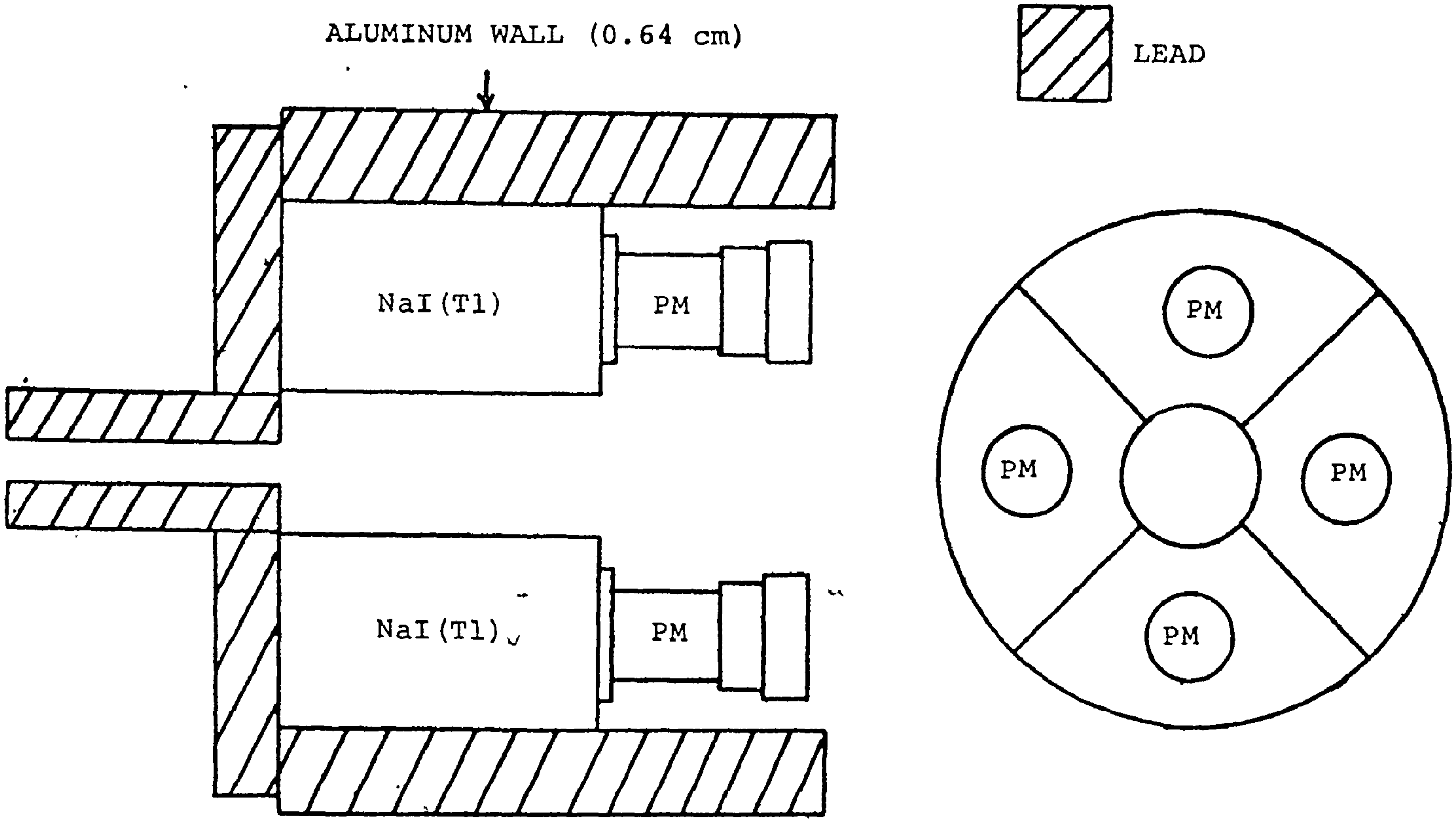

SCALE: QUARTER

FIG. 3-4 NaI(Tl) ANNULUS AND SHIELDING

radiation from the wall of the reactor pool. High voltage (∿ +1400V) is applied through a Hamner NV-21 high-voltage divider and a 3-kilovolt Hamner 4035 power supply. The signals extracted from the respective anodes are fed into Canberra 1405 scintillation preamplifiers, and from there to Canberra 1411 double delay-line (DDL) amplifiers.

## 3.4 THE TARGETS

Since powdered, as well as solid, targets were required it was necessary to contain them. Cylindrical containers of plexiglass, with inner dimensions of 5.08 cm in length and 2.54 cm in diameter, were machined to a wall and cap thickness of 0.4 mm to minimize any intereaction rate within the container material. The targets were then centred within the annulus by the technique illustrated in figure 3-5. Both the aluminum sleeve and the plexiglass suspensory attachments were kept to a minimal thickness. The sleeve was calibrated along its length to determine positioning of the targets within the annulus. The beam was made coaxial with the targets by adjusting the supporting table for the annulus until the scaling of annihilation quanta in the quadrants balanced. The targets selected as suitable for an investigation of double pair production are listed in table 3-1.

## 3.5 ELECTRONICS

The philosophy of the experiment was a prime influence in the designing of the electronic configuration. Although

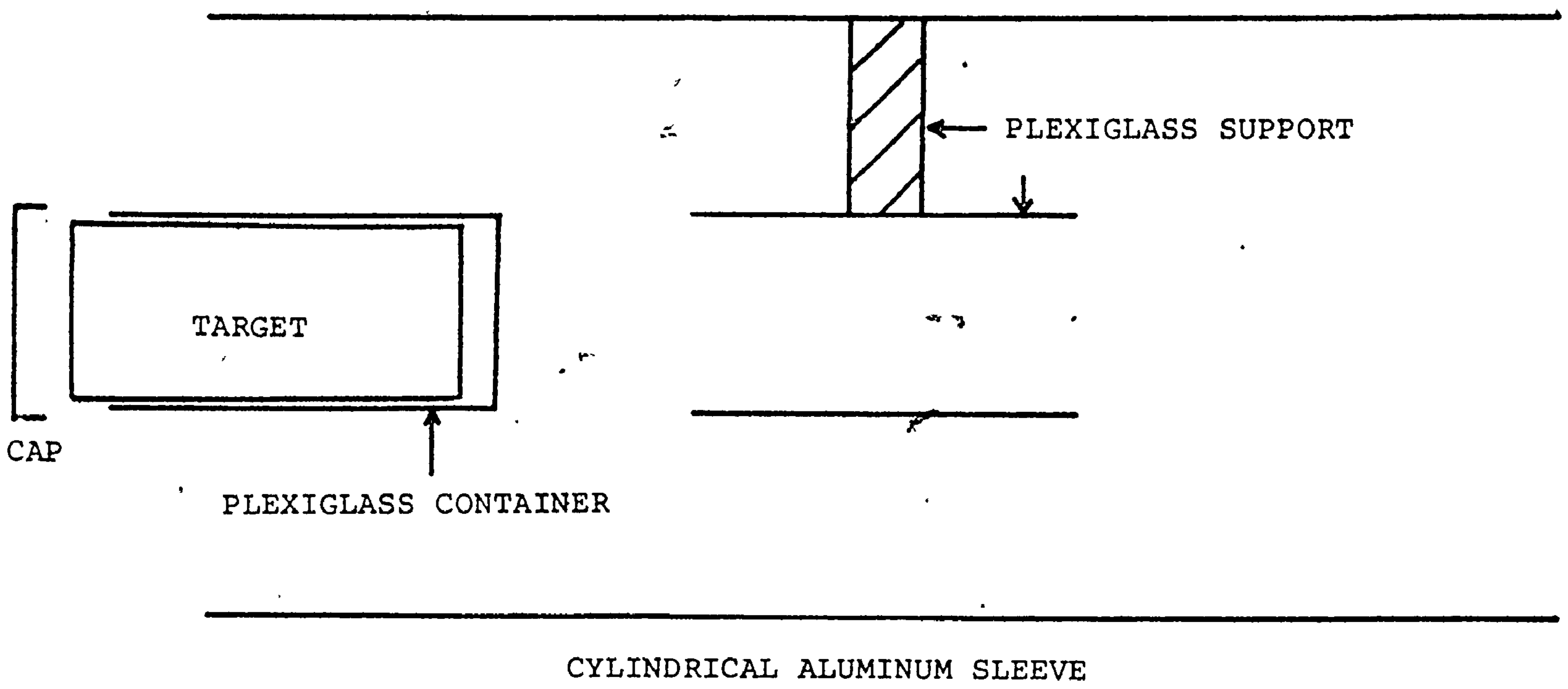

FIG. 3-5 TARGET HOLDER

### TABLE 3-1 TARGETS FOR FOURFOLD COINCIDENCE EXPERIMENT

| TARGET | ATOMIC NUMBER | TARGET LENGTH | |
|---|---|---|---|
| | | (cm) | (gm/cm$^2$) |
| Be | 4 | 4.45 | 8.29 |
| B | 5 | 4.89 | 4.12 |
| C | 6 | 4.45 | 7.33 |
| Al | 13 | 4.45 | 12.0 |
| S | 16 | 5.06 | 6.37 |
| Cu | 29 | 4.90 | 14.3 |
| Cu | 29 | 4.45 | 39.9 |

basically the rates of fourfold coincidences of 511-keV photons were required, it was appreciated that an accounting for chance coincidences would also be necessary. Allowance could be made for such events by recording a spectrum of coincidence times, obtained through use of a time-to-amplitude converter (TAC). The TAC could be started by a pulse signifying the coincident detection of annihilation quanta in one pair of opposite quadrants and stopped by a similar coincidence pulse derived from the other pair of quadrants. With the range of coincidence times for the stop-side quadrants widened to include many chance events, the true coincidences would be recognized in the time spectrum as constituting a large narrow peak, on top of a flat background due to chance coincidences. A time spectrum, typical of the use of such an arrangement, is illustrated in figure 3-6. In addition, it was realized that a large background component due to bremsstrahlung events would be present in the fourfold rates. It would therefore be necessary to record the complete energy coincidence spectrum, for events in the stop-side quadrants, in order to separate the coincidences of 511-keV photons from the bremsstrahlung continuum. A characteristic energy coincidence spectrum is presented in figure 3-7. In total then, a three-parameter (time-energy-energy) spectrum was required. The electronic configuration shown in figure 3-8 was designed to permit encodement of such a spectrum.

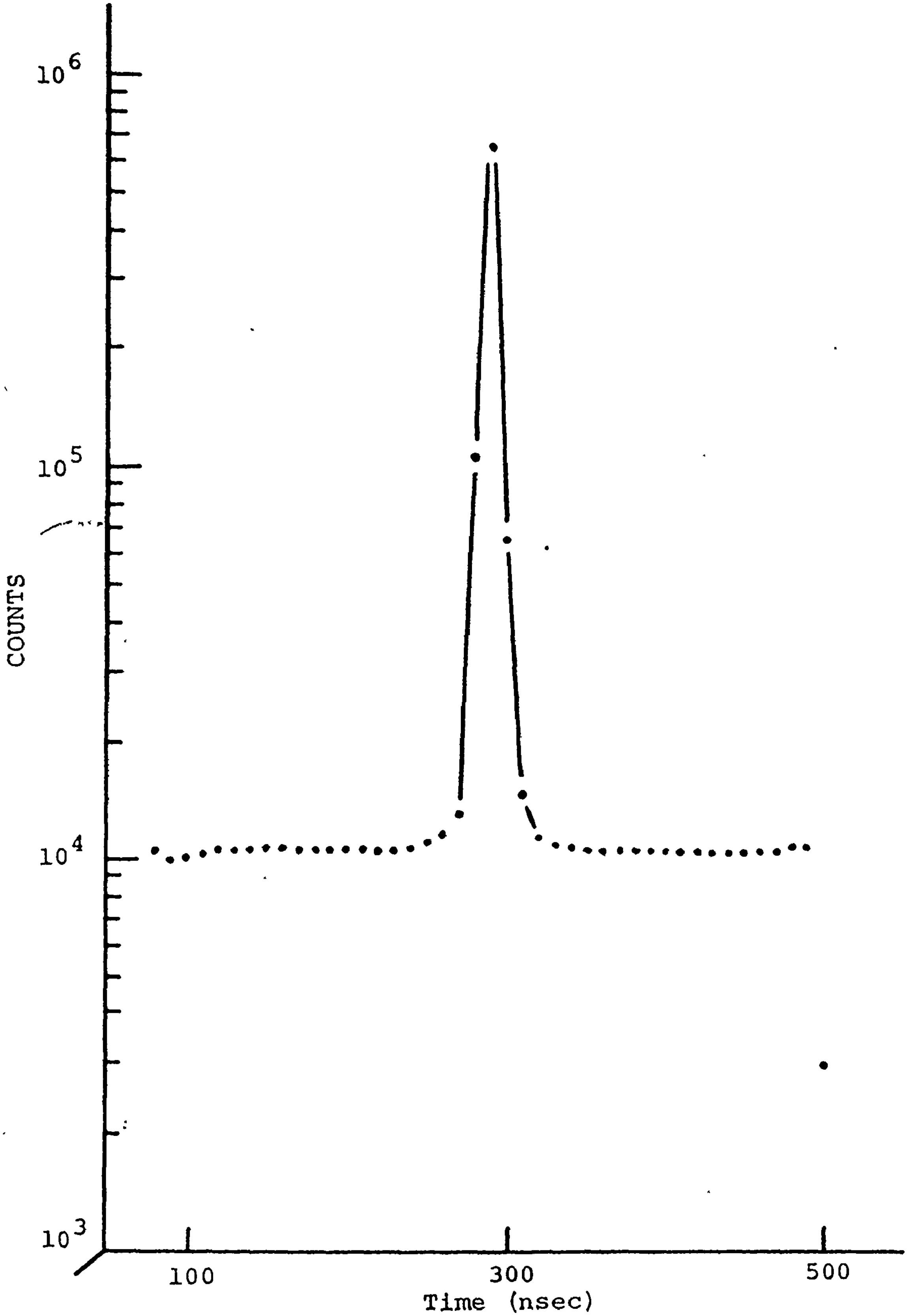

FIG. 3-6 TIME SPECTRUM ASSOCIATED WITH FOURFOLD COINCIDENCE EVENTS.

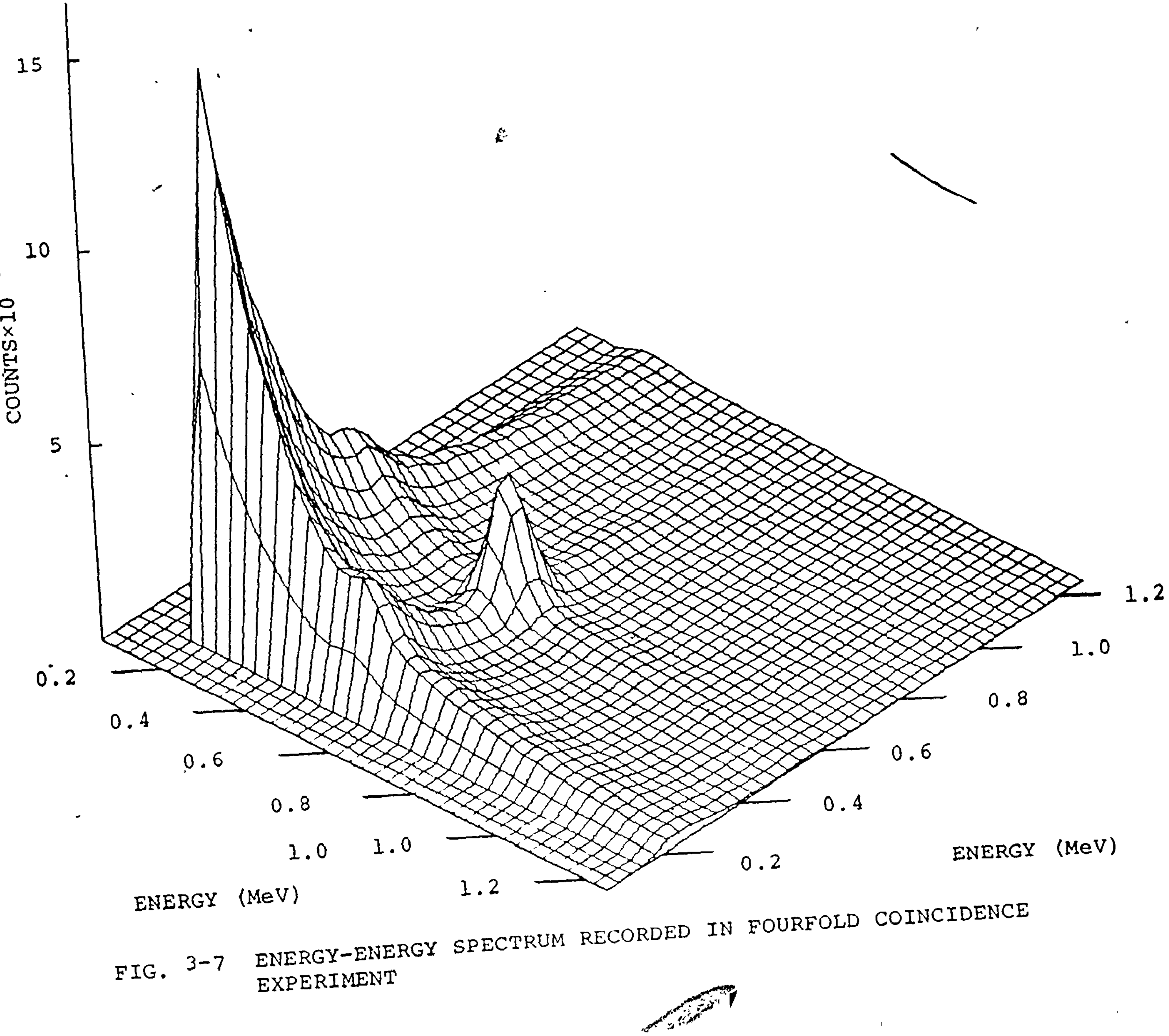

FIG. 3-7 ENERGY-ENERGY SPECTRUM RECORDED IN FOURFOLD COINCIDENCE EXPERIMENT

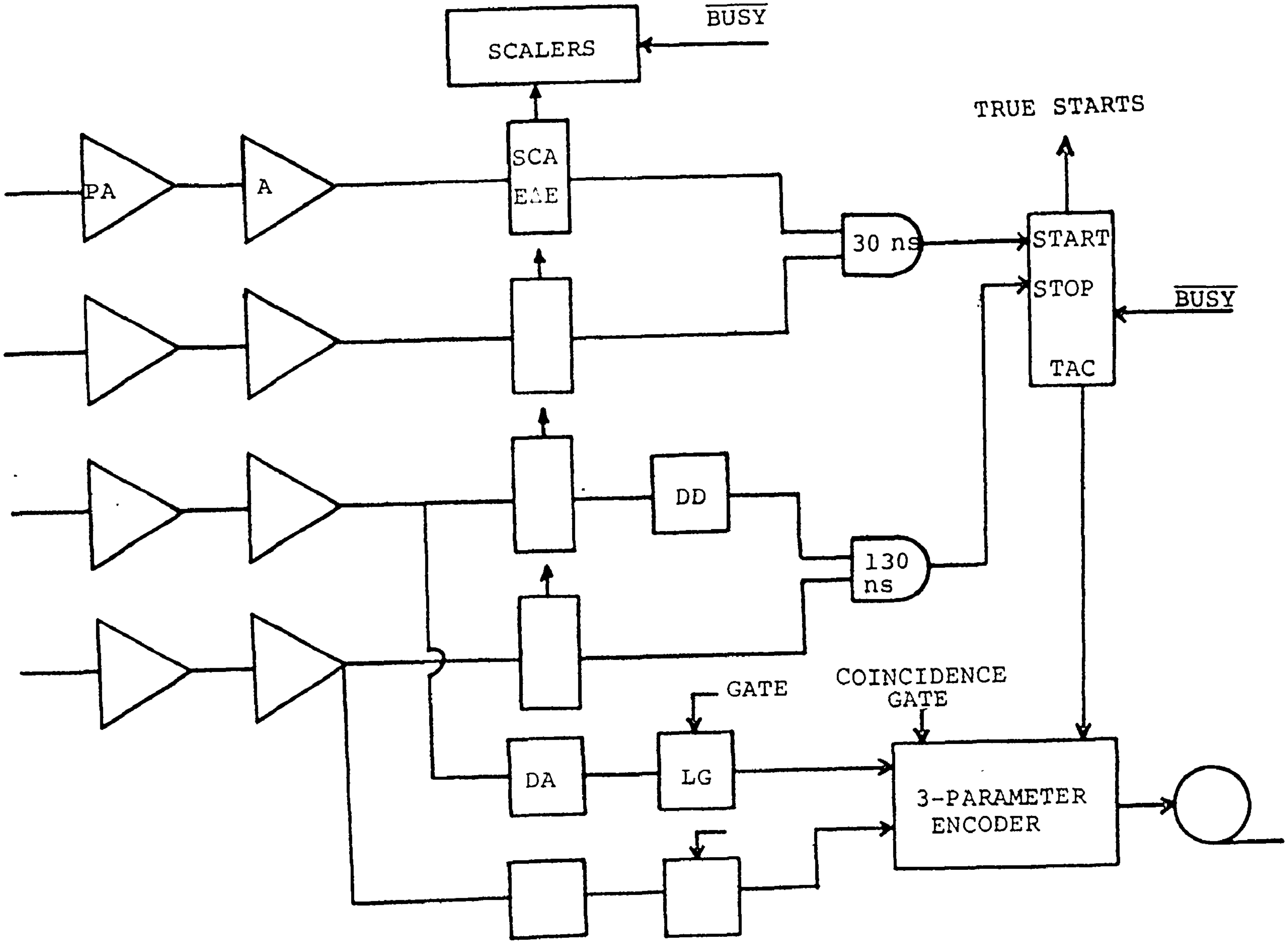

FIG. 3-8 ELECTRONIC CONFIGURATION

Following preamplification and amplification the resultant bipolar pulses from the four quadrants are each fed into a Canberra 1435 single channel analyser (SCA). In one pair of timing SCAs, associated with diametrically opposite quadrants, pulse-height windows are set around those pulses corresponding to 511-keV quanta. The crossover-timing pulses from the fast outputs of the SCAs then trigger a 30-nsec coincidence gate, using an EG&G C102B/N dual-coincidence module. The coincidence output pulse is then used to start an Ortec 437A time-to-amplitude converter (TAC). The other two SCAs are used in a similar fashion but for two significant differences. The pulse-height windows are widened considerably to encompass almost all of each pulse-height spectrum, and one of the fast-output pulses is widened by means of an EG&G TD101/N differential discriminator. The resulting 130-nsec coincidence gate is then used to stop the TAC. The pulse-height spectra from the monopolar outputs of the second pair of DDL amplifiers are fed into Canberra 1451 linear gates, after being delayed appropriately through Ortec 427 delay amplifiers. The linear gates are opened by logic pulses derived from another timing SCA into which pulses from the 1-Ω output of the TAC are fed. The resulting pulse-height spectra, derived from energies deposited in the two stop-quadrants, as well as that obtained from the 93-Ω output of the TAC, are then fed into three 4-K analogue-to-digital converters (ADCs) associated with a Nuclear Data 3300 analyser. Appropriate coincidence gates are formed, using Canberra 1455 logic shaper and delay modules, to condition each ADC. The three "addresses" formed by the ADCs for each fourfold event are then deposited in a buffer memory consisting of 1536 six-bit words. Whenever the capacity of the memory is reached the contents are automatically encoded on magnetic tape using a Datamec D202 tape deck. A signal, indicating that the ADCs are not busy ($\overline{\text{busy}}$), is extracted and used to condition both the TAC and a set of scalers. Thus the need for correction due to dead-time within the data-collection system is obviated. The scalers are used to record true start events from the TAC, live time from an internal clock, fourfold coincidences as a check on the data-collection system, and events within the SCA windows. The latter serve, by reason of expected symmetry, as a partial check against malfunction of the electronics during the considerable running time required. Additionally of course, all signals need periodic examination to ensure proper operation of equipment. The 20 MHz, nine decade, gateable, multi-scaler module was designed and built in this laboratory by J. Skene.

## 3.6 ANALYSIS OF EXPERIMENTAL DESIGN

The start rate, $N_1$, for the above experiment can be expressed simply as

$$N_1 = \frac{\sigma_\pi}{\sigma} (1-e^{-n\sigma})\phi_\gamma \, \varepsilon_1 f_s F_s + N_o, \tag{3.1}$$

where $\sigma_\pi$ and $\sigma$ are the pair and total cross sections for 6.6-MeV gamma rays, n is the sample thickness, and $\phi_\gamma$ the γ-ray flux. $\epsilon_1$ stands for the start efficiency including window effects, $f_s$ the containment probability for positrons from primary pair events, $F_s$ the self-absorption factor for the annihilation quanta, and $N_o$ the rate due to background and accidental coincidences. That the latter constitutes a fairly insignificant contribution to the start rate can be seen from figure 3-9. Part (a) shows a typical singles spectrum following positron annihilation and part (b) another spectrum collected as coincident with 511-keV events in the opposite quadrant. Clearly, the full-energy peak seen in the coincidence spectrum is practically devoid of accidental and background events.

In a similar fashion, the stop rate can be expressed as

$$N_2 = \frac{\sigma_\pi}{\sigma} (1-e^{-n\sigma}) \phi_\gamma \, \epsilon_2 f_s F_s \, , \qquad (3.2)$$

where $\epsilon_2$ is the intrinsic efficiency for full-energy detection of two coincident 511-keV photons by that part of the system which stops the TAC (stop efficiency).

The rate of fourfold coincidences can then be written to include double-pair creations, as well as direct and bremsstrahlung-cascade events, as

$$N_4 = \phi_\gamma (1-e^{-n\sigma}) [\frac{\sigma_{\pi\pi}}{\sigma} f_d + \frac{\sigma_\pi}{\sigma} P_{D\pi} f_D + \\ + (\frac{\sigma_\pi}{\sigma} \int P_B(E) \frac{\sigma_\pi(E)}{\sigma(E)} <1-e^{-n\sigma(E)}> dE) f_a f_b ] \epsilon_1 \epsilon_2 F_s^2 \, . \qquad (3.3)$$

Here $\sigma_{\pi\pi}$ is the double-pair-production cross section, $f_d$ the containment probability for positrons due to double pair production, $P_{D\pi}$ the probability of producing a pair by the direct-

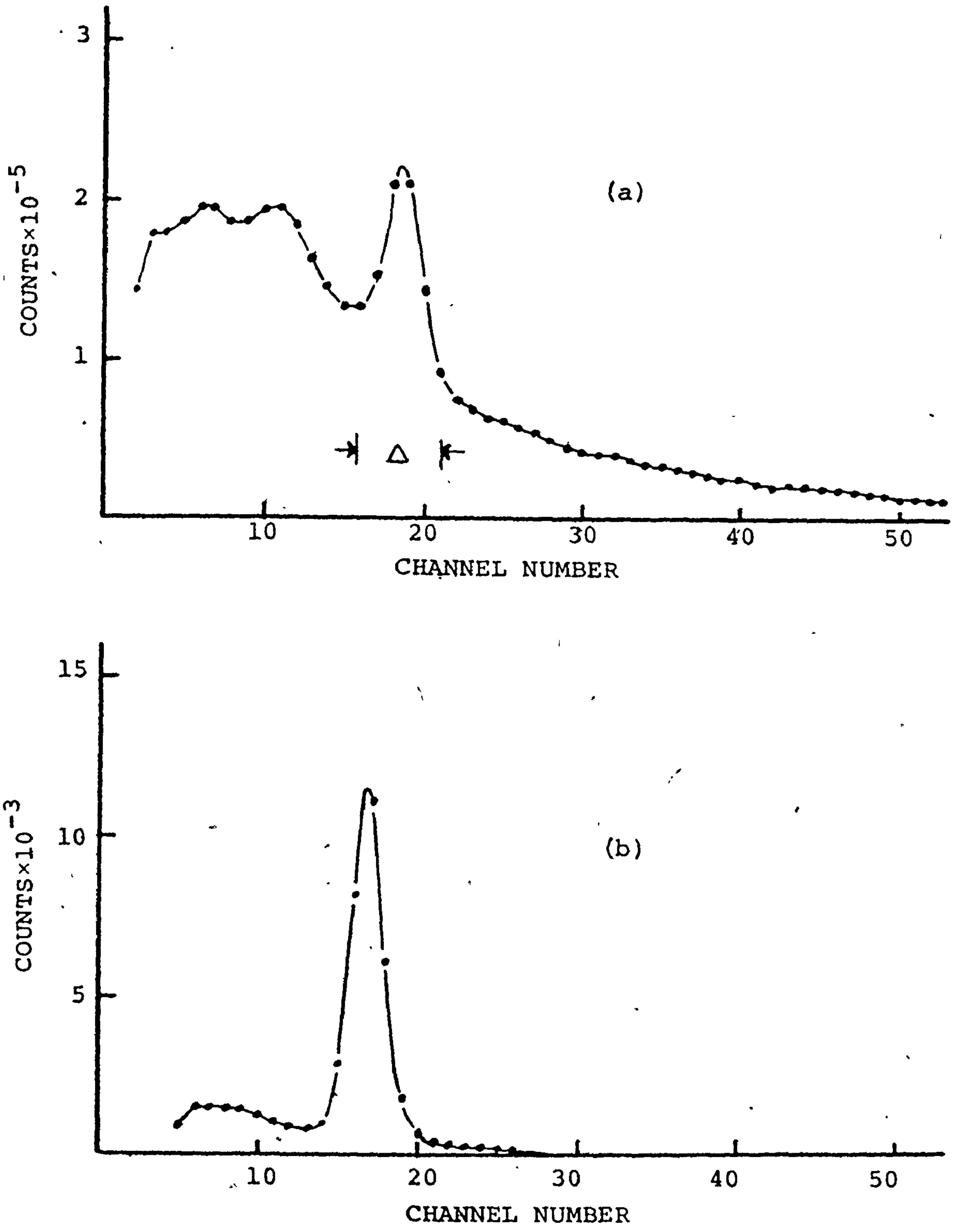

FIG. 3-9 EFFECT OF PULSE-HEIGHT WINDOW

(a) Illustrates a typical singles spectrum collected in one quadrant of the NaI(Tl) annulus. The window of width Δ includes events falling within the 511-keV full-energy peak.
(b) Illustrates those events in the opposite quadrant which are in coincidence with events within the window. A carbon target was used for both spectra.

cascade process, and $f_D$ the containment factor for the two positrons. Also, $P_B(E)$ is the probability of yielding a bremsstrahlung photon of energy E following a single-pair production, $f_a$ the containment probability for a positron of a pair involved in a radiative collision and $f_b$ the containment probability for a positron created by the bremsstrahlung-cascade effect. The ratio, $R_4$, of fourfold events to true start events is then given as

$$R_4 = \left[\frac{\sigma_{\pi\pi}}{\sigma_\pi}\left(\frac{f_d}{f_s}\right) + P_{D\pi}\left(\frac{f_D}{f_s}\right) + \left(\frac{f_a f_b}{f_s}\right)\int P_B(E) P_\pi(E)\,dE\right]\varepsilon_2 F_s \ . \quad (3.4)$$

In this expression

$$P_\pi(E) \equiv \frac{\sigma_\pi(E)}{\sigma(E)} \langle 1-e^{-n\sigma(E)} \rangle, \qquad (3.5)$$

with the average calculated over the exponential distribution of reaction rate along the target. It should be noted that $R_4$ is independent of the incident flux.

It is extremely difficult to measure all of the containment probabilities found in equation (3.4). One can note, however, that $f_d, f_D, f_a$ and $f_b$ are all fractionally greater than $f_s$, since less energy is available to the positrons involved. Since each has a possible maximum value of unity one can safely disregard them, within the context of the large experimental errors expected, by ensuring that $f_s$ represents a reasonably high probability for each target. This can be achieved somewhat by using targets which are both wide and several positron ranges in length.

## 3.7 ADDITIONAL EXPERIMENTS

Analysis of the experimental design (section 3.6) uncovered the need for several subsidiary experiments. The most obvious need was for an evaluation of the common factor $\varepsilon_2 F_s$ in equation (3.4).

It was decided to measure the stop efficiency, $\varepsilon_2$, by investigating the rate of coincident detection of 511-keV quanta in the two stop-side quadrants. A source which was solely a positron-emitter was required since complications arising from coincidence-summing effects would therefore be avoided. If a positron source of low-Q value was chosen, all of the positrons would be stopped within a small thickness of material. Difficulties stemming from annihilations occurring within the annulus material would then be precluded. The consequent point-source geometry afforded by such a source, mounted at the centre of the annulus, would simplify interpretation of the experiment considerably. The coincidence rate, $N_{AB}$, could be written as

$$N_{AB} = 2N_{\pi}\varepsilon_A\varepsilon_B\Omega f F_{AB}, \qquad (3.6)$$

where $N_{\pi}$ is the rate of emission of positrons, $\varepsilon_A$ and $\varepsilon_B$ are the intrinsic 511-keV "photopeak" efficiencies for the two quadrants involved, and $\Omega$ is the solid angle subtended by a quadrant. The containment probability for positrons is represented by f, and the self-absorption factor for escape of both annihilation quanta by $F_{AB}$. If the rate of single 511-keV events in each quadrant was measured concurrently with the coincidence investigation, the respective rates would be similarly expressed as

$$N_A = 2N_\pi \varepsilon_A \Omega f F_A , \qquad (3.7)$$

and

$$N_B = 2N_\pi \varepsilon_B \Omega f F_B . \qquad (3.8)$$

Here $F_A$ and $F_B$ are the self-absorption factors for single-escape of 511-keV photons. By forming the ratio, $R_{AB}$, of the square of the coincidence rate, $N_{AB}$, to the product of the singles rates, $N_A$ and $N_B$, one would obtain

$$R_{AB} = \varepsilon_A \varepsilon_B \left(\frac{F_{AB}^{\;2}}{F_A F_B}\right) , \qquad (3.9)$$

which is notably independent of $N_\pi$, $\Omega$ and f. Therefore, if the ratio of self-absorption factors in equation (3.9) were effectively established as unity, the efficiency product $\varepsilon_A \varepsilon_B$ could be determined. The stop efficiency, $\varepsilon_2$, for an investigation of fourfold events could then be evaluated as

$$\varepsilon_2 = 2\varepsilon_A \varepsilon_B \Omega \qquad (3.10)$$

from comparison of equations (3.2) and (3.6) solid-angle considerations. A small correction would of course be necessary to allow for the finite distribution of annihilation centres within the various targets. However, an indication of the relative variation in efficiency with position, along the axis of the annulus, could easily be obtained by measuring the twofold coincidence rates for a thin target, or a positron source, placed in known positions.

In order to ensure that the ratio of self-absorption factors in equation (3.9) was indeed very close to unity, one would have to use a material low in atomic number as the stopping substance for the positrons. Since the self-absorption factors would be close to unity individually, the ratio of factors would certainly be very close to unity.

Furthermore, since it was tacitly assumed in the above discussion that the "true" coincidence and singles rates would be used, some means of obviating all dead-time effects would be required. In accordance with a standard technique, suitable pulses, from a pulser of known frequency, could be fed into both stop-side preamplifiers. The pulser rate, which would necessarily be considerably lower than the source rate, would then be used to establish the experimental live time.

A determination of dead-time effects within the stop-side electronics was also demanded. It was appreciated that such effects could be investigated by measuring the coincidence rate for 511-keV quanta from a positron source, as the strength of the source decayed in time. Thus with proper selection of a suitably short-lived positron-emitter, dead-time effects could be investigated in parallel with the efficiency evaluation mentioned above. In order to include only dead-time effects due to the stop-side electronics, the analyser could be operated for a preset live time.

Since no suitable experiment could be devised to truly isolate the self-absorption factor $F_s$ in equation (3.4), for each target, it was elected that the factors should be evaluated theoretically. Numerical quadrature would be required, but the results would be fairly accurate since well known cross sections and a well defined geometry would be involved. Although the calculations could prove to be tedious, as a result of including the annulus geometry and the interaction rates therein, effort would be rewarded by two bonuses in particular. One could check the stop efficiency calculated for a small disc target against the experimentally determined values, and also, an easy method would be available for correction of the measured efficiency for finite target geometry. Furthermore, the values of $F_s$ calculated for the various targets could be compared, for purposes of reliability, with known results for simpler geometries[96)].

A determination of the containment probability, $f_s$, for positrons from primary pair events in each target was also required. An experimental evaluation could be achieved by measuring the stop rate for 0.511-MeV quanta in each target. As is indicated by equation (3.2), with the efficiency and self-absorption factors already known, and the cross sections readily available, the containment probabilities could be evaluated if the flux were known absolutely. Further thought suggested the possibility of an effective increase in flux due to pairs being created subsequent to Compton scattering of the incident beam. The significance of such multiple events could be calculated in terms of a simple model.

Thus, before containment factors could be evaluated, an experiment was required to measure the gamma flux absolutely. The well known absolute characteristics of commercially available NaI(Tl) scintillators[97)] came to mind. However, since the gamma beam was too intense for direct viewing, a measurement of a known fraction of the beam was needed. It was decided that a method employing Compton-scattered radiation would be used since the Klein-Nishina theory is firmly established for the range of energies concerned.

However, as intimated previously, it was anticipated that the gamma flux would change from experiment to experiment, as a result of either changes in reactor power or intentional insertion of concrete attenuators. It was therefore necessary to have some method of monitoring the integrated flux, for twofold coincidence experiments in particular. The method chosen involved the collimated viewing, by a NaI(Tl) detector, of radiation perpendicularly Compton-scattered by the paraffin wax in front of the annulus. By using a lower-level discriminator, events corresponding to the scattering of 6.6-MeV photons could be selected. It would of course be necessary to check the monitor for linearity of response to changes in reactor power. The effect of the absorbers could also be determined.

The bremsstrahlung term expressed in equation (3.4) also required attention. Although it was realized that a calculation could give some estimate of the relative significance of the term, it was also understood that an experimental method would be possibly more believable and certainly more satisfying. An investigation of triple-coincidence rates was chosen as the possible solution. In such an experiment, a TAC would be started under the normal condition of "simultaneous" detection of two 0.511-MeV quanta in one pair of opposite quadrants, but stopped by any event detected in a third quadrant. The energy spectrum extracted from the third quadrant would be derived, almost exclusively, from bremsstrahlung events. Perhaps an examination of the bremsstrahlung spectra from several targets would then lead to the elimination of the bremsstrahlung-cascade contribution to the fourfold-coincidence ratios.

Finally, energy calibrations could be accomplished by standard methods.

## 3.8 SUMMARY

In summary, the experimental intent was therefore to obtain the fourfold coincidence rates by stripping appropriate 3-parameter spectra, to eliminate the dependence on flux by forming the ratio of the coincidence rates to the true start rates, and to normalize the ratios by dividing throughout by both the stop efficiency and the appropriate self-absorption factor. It was proposed to then subtract off the bremsstrahlung contributions and finally, to separate the remaining contributions, from double pair production and the direct-cascade effect, through the realization that $P_{D\pi}$ is directly proportional to atomic number whereas $\sigma_{\pi\pi}/\sigma_{\pi}$ is constant. For convenience, the approach is delineated as a flow-chart in figure 3-10.

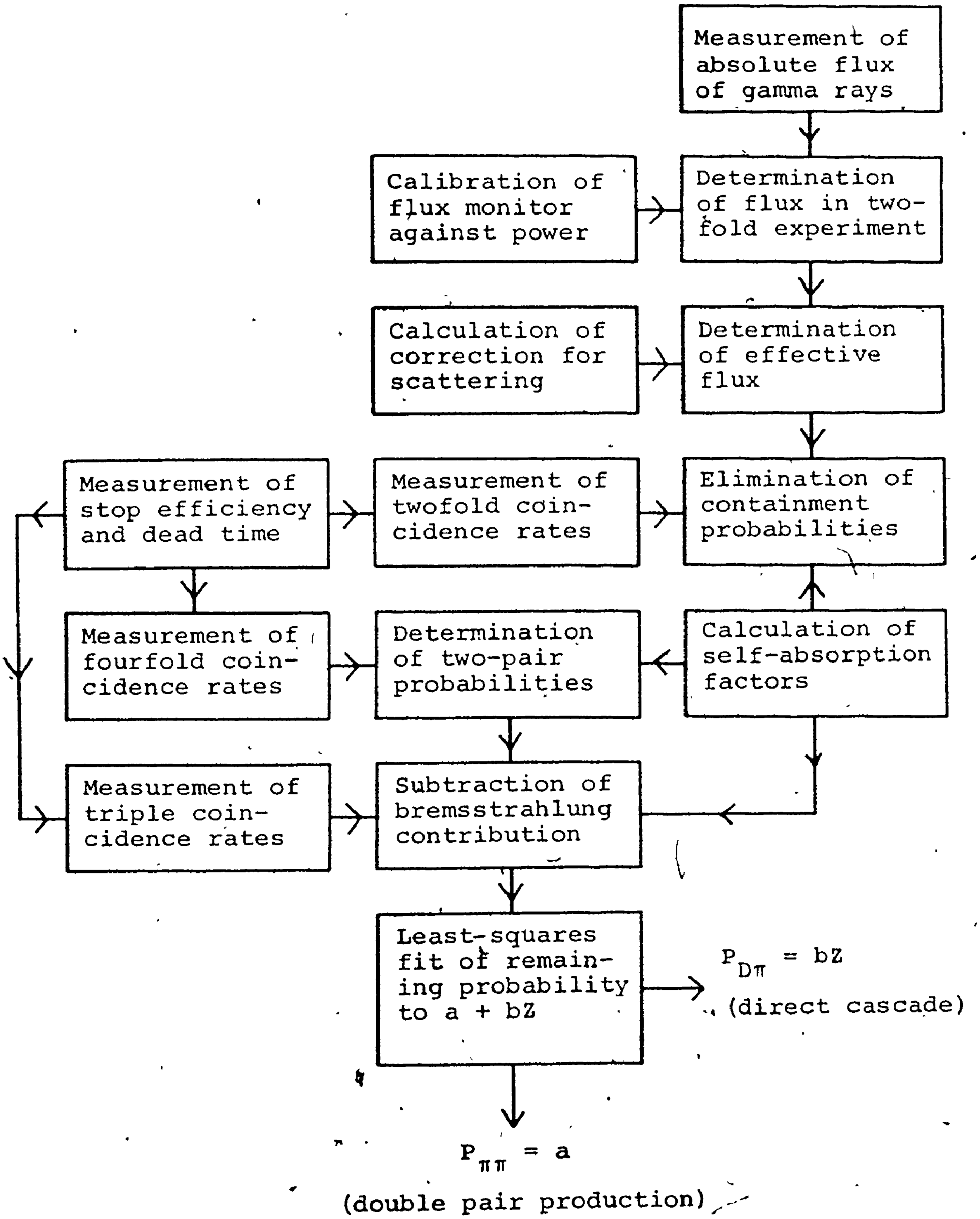

FIG. 3-10 SUMMARY OF EXPERIMENTAL APPROACH

# CHAPTER IV

# EXPERIMENTAL PROCEDURES

## 4.1 ABSOLUTE MEASUREMENT OF GAMMA-RAY FLUX

As intimated in section 3.7, the flux of gamma rays issuing from the external collimator was too intense to be measured directly. It was therefore necessary to measure a known fraction of the beam strength. The method chosen entailed using a NaI(Tl) spectrometer, under conditions of good geometry, to measure a portion of the flux which had been Compton-scattered by a target. A piece of aluminum plate approximately 0.64 cm in thickness, and 10 cm by 10 cm on edge, was selected as the scatterer. The lateral dimensions were purposely chosen to be much larger than the beam diameter of 1 cm to avoid any possibility of the beam striking an edge of the plate. The 0.64-cm thickness ensured a reasonable reaction rate without introducing either large self-absorption effects or unnecessary enlargement of the geometry of the source of scattered radiation. A scattering angle of roughly 30 degrees was chosen for several reasons. It permitted the detection system to be well removed from the direct beam, it provided a scattered flux of adequate intensity, and it determined the energy of 6.6-MeV photons to be approximately 2.5 MeV after scattering. The last reason given was significant in the context of the energy of the scattered $\gamma$ rays being well above the energy of the photons most commonly found in the general room-background. The prime background contributant was the 1.294-MeV photon following beta decay of $^{41}$Ar within the air of the reactor building. The experimental configuration is illustrated in figure 4-1.

The beam of gamma rays was allowed to pass, unimpeded, through the annulus described in section 3.3. The path of the direct beam was then located, at a position approximately 5 m behind the NaI(Tl) annulus, by means of a lead-shielded Geiger counter. In order that both the scatterer and the detection system could be positioned with accuracy, the path of the beam was delineated by a thin string stretched from the centre of the annular "nose-cone" to the appropriate position 5 m behind the annulus.

A Harshaw I2S 12/3 3-inch NaI(Tl) detector was loaded into a lead shield specially designed as form-fitting to firmly constrain the crystal, but open-ended to permit both direct viewing of the source and easy extraction of any resultant signals. The detector assembly was then placed on top of additional lead shielding, previously positioned on a movable table, and adjustments made until the axis of the detector was horizontally coplanar with the direct beam. A lead collimator, 15.1 cm in length and 3.8-cm inner diameter, was positioned coaxially in front of the NaI(Tl) crystal. Lead bricks and lead wool were

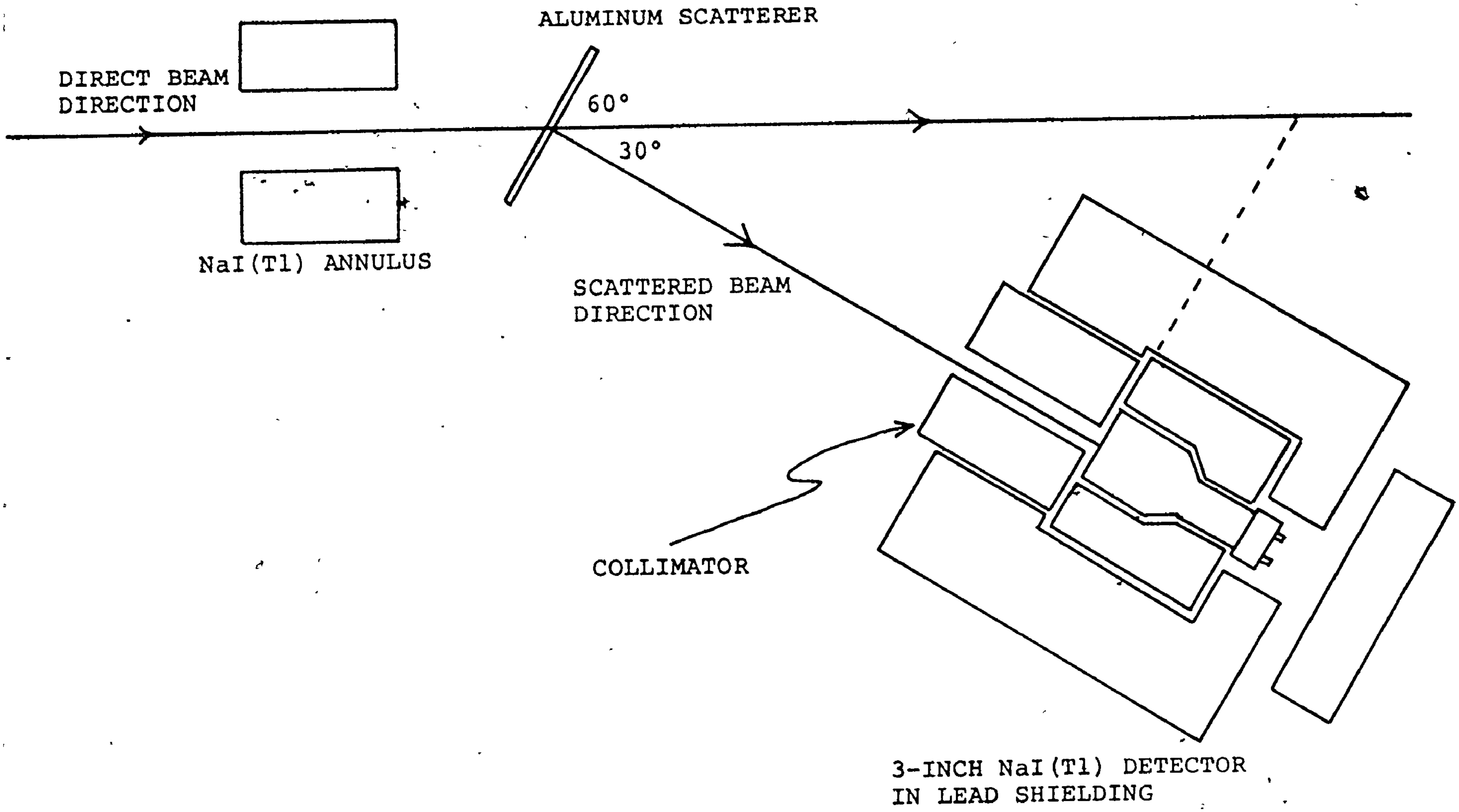

FIG. 4-1 EXPERIMENTAL CONFIGURATION FOR DETERMINATION OF ABSOLUTE GAMMA-RAY FLUX

then added to the table to surround the detector with shielding, as much as possible, to an approximate average thickness of 15 cm. No observable change in position of the detection system was induced by the large mass of shielding.

By careful adjustment of the movable supporting table, the axis of the NaI(Tl) spectrometer was oriented to intersect the beam direction at an angle of 30 degrees. The angular setting was achieved through use of a large set square, and confirmed by means of a triangulation method which involved linear measurement of the dimensions of the right-angled triangle shown in figure 4-1. The angle of scattering, although important, was not absolutely critical since it could be determined in the average, by calibration of the energy of the scattered radiation detected in the experiment. The face of the NaI(Tl) crystal was found to have been positioned 83.8 cm from the point of intersection of the detector axis with the beam direction. A large set square was then used to orient the aluminum scattering plate, abouts its point of intersection with the beam, until the plane of the plate was parallel to the face of the detector. Thus the plate was positioned vertically but at an angle, measured in the horizontal plane, of 60 degrees with respect to the beam direction.

Approximately 600 volts were applied to the detector by means of an Atomic 312 high voltage supply, and signals were extracted via a Cosmic 901 amplifier and preamplifier system. The signals, which were predominantly derived from scattered radiation, were then fed into a 4-K ADC associated with a Nuclear

Data 3300 pulse-height analyser. Since a 256-word spectrum proved suitable, only the eight most significant conversion bits were used.

Spectral data were collected for 400 minutes of live time. The experiment was then continued for an additional 400 minutes of live time with the analyser operating in the subtraction mode and the scatterer repositioned in the beam at a point upstream of the initial placement, but outside of the field of view of the NaI(Tl) detector. Correction was thus largely achieved for background radiation and scattering of the direct beam by air molecules. The complete experiment was conducted with no concrete absorbers in the beam and the reactor operating at a 5-MW power level throughout.

An energy calibration of the system was accomplished by means of a $^{22}$Na source and a $^{56}$Co source obtained from proton-irradiation of $^{56}$Fe.

The results of this investigation, and all subsequent experiments, are reported in full in Chapter V.

## 4.2 FLUX MONITOR

The need for a reliable method of measuring the integrated flux, incident upon individual targets, was expressed in section 3.7. The components of the system employed as a flux monitor, and their arrangement, are illustrated in figure 4-2.

A 1.5 inch Harshaw 6S 8/2 NaI(Tl) detector was mounted in a lead sheath which had a wall thickness of 5 cm and a viewing aperture of 2.5-cm diameter. The detector was positioned against

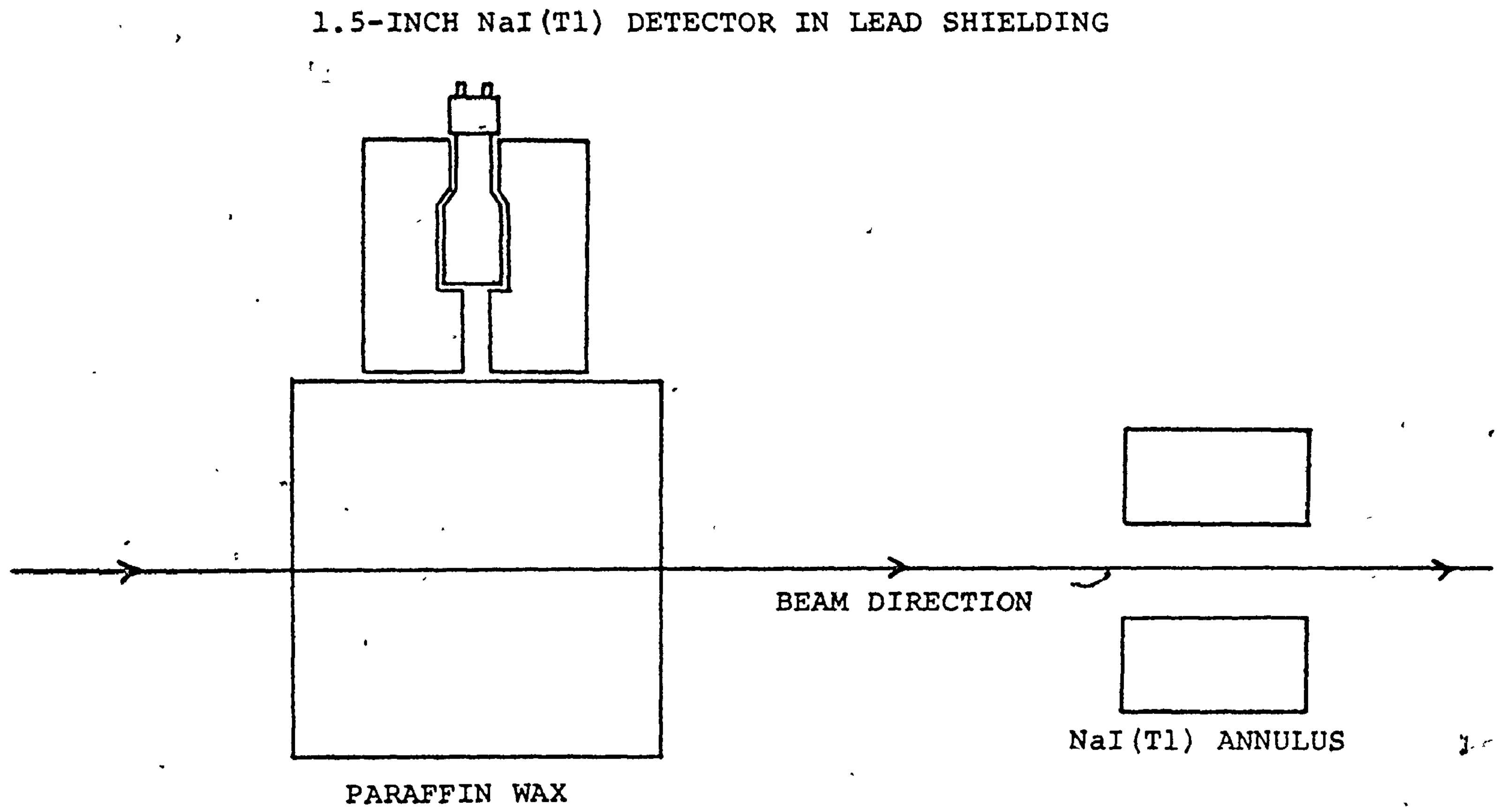

FIG. 4-2 EXPERIMENTAL CONFIGURATION FOR FLUX MONITOR

the paraffin shield, but perpendicular to the gamma beam. In a fashion similar to that employed in the absolute flux measurement discussed above, it was intended to determine the relative flux strength by monitoring that fraction of the beam of 6.6-MeV gamma rays which was Compton-scattered by the paraffin wax into the 1.5-inch NaI(Tl) crystal. Since it was necessary to sample the beam before it reached the vicinity of the annular pair spectrometer, the paraffin wax was selected as a suitably placed scatterer. High voltage for the detector was provided by an Atomic 312 supply, and all signals extracted were fed into a lower-level discriminator designed and built in this laboratory. In brief, the main components of the discriminator were an SN72710N integrated-circuit comparator fabricated by Texas Instruments, and some shaping circuitry. The comparator was set to trigger for only those scattering events associated with original gamma-ray energies of several MeV. The output pulses of the discriminator were then accepted for direct scaling.

The above setup constituted the means of monitoring the relative flux intensity under a variety of conditions of reactor power and beam attenuation. Since the monitor rate corresponding to a reactor power of 5 MW was of order $10^3$ counts/sec, the effect of any combination of concrete absorbers could be ascertained very quickly. However, before the monitor could be used with any degree of confidence, it was necessary to check its linearity of response to changes in reactor power. To that end, an experiment was designed around the multiscaling capability of the Nuclear Data 3300 pulse-height analyser. The logic pulses from the discriminator were fed to the input of the multiscaling circuitry, and the necessary channel-advance gating achieved via a BNC PB-2 pulser. The dwell time for scaling in each channel was determined from the pulser frequency to be 8.812 seconds. Thus a record of the counts scaled in each consecutive time period was stored in consecutive channels, or memory locations, of the analyser. It was then a simple matter to change the power level of the reactor and record the consequent change in counting rate. The monitor rate was actually investigated for reactor power levels of zero to 5 MW, in 0.5-MW steps above the 1.5-MW level. The time spent in counting at any one level was at least fifteen minutes. This permitted the reactor operations staff to stabilize the power output, with good accuracy, at the desired levels. The dwell time chosen (∿ 9 sec), and the 16-K memory capacity available, allowed the complete experiment to be conducted in one continuous operation.

When the reactor was at the 5-MW power level, concrete absorbers were introduced to determine the variation in monitor rate induced by different combinations of attenuators. In each instance the flux monitor was scaled for 90 seconds.

## 4.3 EFFICIENCY AND DEAD-TIME MEASUREMENT

In the analysis of the experimental approach to the measurement of fourfold rates it quickly became apparent that an evaluation of the efficiency of the stop-side quadrants, for coincident detection of annihilation quanta, was essential for correct interpretation of the empirical data. Although the electronic configuration in figure 3-8 had been designed to be gated off during the times of pulse-height analysis and data recording, to eliminate most of the total dead time, some inherent dead-time effects remained for the stop-side quadrants and electronics. It was conceived that an examination of coincidence rates from a suitable positron source, decaying in time, could lead to a determination of both the efficiency and the dead-time effects within the same experiment.

An $^{18}F$ source proved to be eminently suitable for several reasons. Since it was solely a positron emitter no corrections were required for coincidence summing of annihilation quanta with other photons. The half-life of 109.8[98)] minutes was sufficiently short for the decay of the source to be conveniently examined over many half-lives, but sufficiently long to permit any necessary changes in the experimental setup without the need for haste. The Q-value of 0.635 MeV[98)] required that only a small amount of material be used to stop all of the positrons. Furthermore, it was possible to make the source by neutron-irradiation of $^{6}Li_2CO_3$.

Some lithium carbonate powder was irradiated to produce the reaction $^{6}Li(n,t)^{4}He$. The resulting tritons then interacted with the oxygen in the carbonate radical to produce fluorine via the reaction $^{16}O(t,n)^{18}F$. The activated powder was dissolved in sulphuric acid and subsequently distilled. The distillate consisted almost completely of $^{18}F$ dissolved in water.

Since a single drop of distillate provided sufficient source strength it was contained in a simple fashion. Two small pieces of plexiglass were fabricated, one with a small indent in the centre. One drop of the radioactive fluid was inserted in the depression and the other piece of plexiglass glued in place as a lid. The resulting contained source was in the form of a cylinder 0.8 cm in length and 0.8 cm in diameter. This provided more than an adequate thickness of plexiglass to prevent even the most energetic positrons from escaping since the range for 0.635-MeV positrons in a material of density 1.2 gm/cm$^3$ is approximately 0.20 cm.

The source was positioned in the centre of the NaI(Tl) annulus shown in figure 3-4 by means of a holder similar to the one illustrated in figure 3-5. The collimated beam of gamma rays from the titanium sample beside the reactor core was completely blocked off by four 2-inch-thick lead bricks. Since the stop efficiency was to be measured, only that part of the electronic configuration, shown schematically in figure 3-8, which was associated with stopping the TAC, was used in this experiment. However, now the TAC was started by the widened fast-logic pulse from one SCA and stopped by the narrow fast-logic pulse from the other. The monopolar pulse-height spectra from both amplifiers were allowed to entrain through the delay amplifiers and linear gates to two ADCs of the Nuclear Data 3300 analyser. Suitable coincidence pulses for the linear gates and the ADCs were derived from the pulse-height spectrum issuing from the 1-Ω output of the TAC. It was therefore ensured that the electronics used in this experiment duplicated the stop-side electronics designed for investigations of fourfold coincidences. This was important both for dead-time considerations and determination of the stop efficiency.

The basic intent of the efficiency experiment was to measure concurrently the rate of detection of 511-keV photons in each quadrant and the corresponding coincidence rate for annihilation quanta. The efficiency could then be obtained from the ratio of the square of the coincidence rate to the product of the singles rates. Fortunately the Nuclear Data 3300 analyser had an inherent capability of sampling the two input signals to the ADCs , firstly, for a fraction of a second in the coincidence mode, and then for the remainder of the second in the singles mode. This MPA-SS (multiparameter analysis-singles sampling) capability thus permitted practically simultaneous acquisition of doubles and singles spectra in the 16-K analyser memory. Data were consequently recorded in a 128×128 two-parameter matrix in which the axial locations were reserved for accumulation of the two singles spectra. The fraction of time spent in the coincidence mode, and the total live time in the same mode, could be controlled. However, in MPA-SS mode it was not possible to include the pulse-height spectrum from the TAC as a third parameter. The small incidence of chance events was therefore reduced by selecting only those TAC pulse heights which corresponded to time-correlated events. The SCA logic pulses so derived were then used to open the linear gates and the coincidence circuitry of the ADCs.

A few differences in requirements between the efficiency determination and the dead-time investigation should be pointed out. Since the efficiency experiment required sampling of both the singles and the coincidence rates for 511-keV quanta, the MPA-SS operational mode was essential. In turn, since the MPA-SS mode required that singles rates be presented at the inputs of the ADCs, the linear gates had to be disabled during the efficiency experiment. Also, since it was necessary to overcome dead-time effects in establishing the "true" singles and doubles rates for 511-keV quanta, in the efficiency investigation, some method of recording live time was required. Pulses of low frequency (105.15 Hz) from a BNC PB-2 pulser were fed into the stop-side preamplifiers to be mixed with those signals coming from the respective photomultiplier tubes. Since the pulser signals, in advancing through the electronics, experienced the same dead time as the random signals from decay of the source, the number of pulser events recorded in memory as coincidence and singles events effectively established the respective live times. By comparison, the dead-time investigation did not require analysis of singles rates. However, the MPA-SS mode of operation was retained since there was no disadvantage in measuring coincidence rates by that method. Moreover, the presence of pulser signals had no effect on the dead-time experiment since the pulser rate was sufficiently low to be negligible. In order to examine the dead-time effects over a wide range of counting rates, the experisource was still great. The consequently high rates were greatly reduced before reaching the ADCs by reintroduction of the coincidence conditioning of the linear gates. Thus excessive dead time within the analyser was avoided. In fact, to ensure that results indicated only the dead time associated with the stop-side electronics, the analyser was operated for preset live times.

The analyser was set to sample the input signals for coincident events during 86.34% of each second of clock time. The remaining 13.66% of each second was spent in sampling both input signals for singles events. The total live time for coincidence sampling was set to be two minutes. Data were then accumulated in memory, under the requirements of the dead-time experiment explained above, for the preset live time. The collected data were then encoded on magnetic tape. Periodically the procedure was repeated but for changes in preset live time to four and eight minutes when required. The decay of the source was followed in this fashion for approximately ten half-lives. When dead-time losses had subsided to what later proved to be less than 1%, the experimental conditioning was altered to that required by the efficiency investigation. Data were acquired for four minutes of coincidence live time. In order to establish the stop efficiency with greater confidence, this procedure was repeated an hour later.

Although the problem of random adding has not been mentioned until now, it was always recognized that such summing could cause trouble in any experiment involving excessively high rates. In this particular experiment very high rates were obviously encountered. Consequently the important efficiency measurements were not made until rates had dropped enough to make random-adding effects completely negligible. Moreover, the pulse height associated with pulser events was purposely made large enough to clearly isolate such events, when collected in the two-dimensional memory configuration, from those arising from the decay of the $^{18}F$ source. Hopefully, any dispersion of events about the vicinity of the pulser data could then be translated into an estimate of the extent of random adding, and the variation with rate of input signals ascertained.

## 4.4 INVESTIGATION OF FOURFOLD COINCIDENCES

This experiment has been substantially described in Chapter III where experimental philosophy and planning have been discussed.

One of the targets listed in table 3-1 was centred axially within the NaI(Tl) annulus. The collimated beam of high-energy gamma rays from $^{49}Ti$ was allowed to strike the target and, if required, concrete absorbers were carefully positioned in the beam to reduce the flux to a reasonable value. Here "reasonable" was conceived to mean that no more than several thousand events per second were detected, without regard to energy, by any one quadrant. The intention was to keep any necessary corrections for random-adding and dead-time effects to a minimum without unduly increasing the already long run-time required. The position of the target was adjusted to optimize the coincidence rate for 511-keV events in two opposite quadrants. Although this caused the centre of the target to be only slightly displaced from the geometric centre of the annulus the position was carefully noted for future calculations.

The electronics shown schematically in figure 3-8 were used to investigate fourfold coincidence events. As explained in greater depth in section 3.5, a TAC was started by a fast-logic pulse signifying the coincident detection of annihilation quanta in one set of opposite quadrants. The TAC was then stopped by another fast-logic pulse corresponding to the coincident detection of two photons of any energy in the other pair of opposite quadrants. If a stop pulse was not received within 750 nanoseconds of the start time the TAC was stopped automatically, and if a start pulse arrived during a conversion period it was rejected by the TAC. If the conditions for a valid start-stop event were met a pulse of height proportional to the time difference was put out by the TAC for processing by the Nuclear Data 3300 analyser. The satisfaction of the conditions also led to the respective pulse heights from the two stop-side amplifiers being gated through to the analyser. The three pulse heights were then analysed in coincidence by three ADCs. Any fourfold coincidence event detected in the above fashion was therefore characterized by a three-parameter description. Such events were then "address-recorded" in a buffer memory which, when full, automatically caused the collected data to be encoded on magnetic tape. Several rates of concern, including the rate of true start events, were scaled during the experiment.

The above procedure was repeated, in turn, for each of the targets listed in table 3-1. Because the probability of occurrence of fourfold coincidences was extremely small, acquisition periods were typically a week per target. Furthermore, in order to eliminate any fourfold coincidences which did not correspond to interactions within the targets, the experiment was repeated with the target container empty.

## 4.5 INVESTIGATION OF TWOFOLD COINCIDENCES

The purpose of this investigation was to determine the containment probability, $f_s$, for positrons created by gamma rays of average energy 6.6 MeV interacting with each target used in the fourfold coincidence experiment. It was hoped that the probability of the positrons being stopped within each target could be shown to be high since it would then be possible to make arguments for ignoring the various containment probabilities found in equation (3.4). Although the experiment required accurate knowledge of absolute flux intensities, stop efficiencies, and self-absorption factors, in addition to twofold coincidence rates, it was deemed preferable to modelling the situation theoretically.

One of the targets listed in table 3-1 was therefore positioned, as for the fourfold coincidence experiment, within the annulus. Three concrete absorbers were then used to attenuate the collimated beam of gamma rays before it was allowed to illuminate the target. Since data were to be corrected for variations in incident flux, via the flux monitor, the fact that the number of absorbers was not varied to duplicate those used in the fourfold coincidence investigation was of no import. Indeed, since sufficient data could be collected in a very short period of time, it was believed much more important that dead-time and random-adding effects be kept to a minimum.

Once again the stop-side electronics used in the fourfold coincidence experiment were required. The only major change in the use of the electronics was that the TAC was started by the fast-logic pulse widened by the EG&G differential discriminator, and stopped by the other fast-logic pulse associated with the opposite stop-side quadrant. Three-parameter (time-energy-energy) data were acquired and encoded on magnetic tape, as for the fourfold coincidence investigation, to permit elimination of chance and background contributions. Typically, an adequate statistical sampling was accrued in several minutes of recorded live time. The total number of flux monitor events, twofold coincidence events, and valid start events were also recorded. The experiment was then repeated until all of the targets listed in table 3-1 had been investigated.

This experiment also afforded the opportunity to investigate the attenuative effects of the concrete absorbers on the high-energy gamma rays in the incident flux. Since the gamma rays of approximate energy 6.6 MeV were predominant in the spectrum of figure 3-3, and since the pair-production cross section increases with energy, by repeating the above procedure for one target under conditions of constant reactor power and different numbers of absorbers, one could determine the variation induced in the flux of gamma rays of average energy 6.6 MeV. Such an experiment was conducted by using the sulphur target.

## 4.6 INVESTIGATION OF THREEFOLD COINCIDENCES

This investigation involved the use of the NaI(Tl) annulus. The conditioning of the experiment required that two 511-keV quanta be detected in coincidence in one pair of opposite quadrants at the same time as an event of any energy was detected in a third quadrant. Since the resultant energy spectrum associated with the third quadrant was envisaged to be almost solely derived from bremsstrahlung events, it was hoped that information relating to the contribution of bremsstrahlung-cascade events to the fourfold coincidence rates could be extracted. In order to validly establish a direct relationship between bremsstrahlung-cascade contributions and the bremsstrahlung spectra found in this experiment, it was necessary to investigate targets over a wide range of atomic number. The targets selected have been listed in table 4-1.

Each of the targets was centred in turn in the NaI(Tl) annulus, to be illuminated by the collimated beam of gamma rays.

TABLE 4-1 TARGETS FOR BREMSSTRAHLUNG INVESTIGATION

| TARGET | ATOMIC NUMBER | TARGET LENGTH (cm) | TARGET LENGTH (gm/cm$^2$) |
|---|---|---|---|
| Be | 4 | 4.45 | 8.29 |
| B | 5 | 4.89 | 4.12 |
| C | 6 | 4.45 | 7.33 |
| Al | 13 | 4.45 | 12.0 |
| S | 16 | 5.06 | 6.37 |
| Ti | 22 | 4.90 | 8.39 |
| Fe | 26 | 4.98 | 20.0 |
| Co | 27 | 4.90 | 17.5 |
| Cu | 29 | 4.98 | 14.3 |
| Cu | 29 | 4.45 | 39.9 |
| Zn | 30 | 4.98 | 20.5 |
| Se | 34 | 4.98 | 11.4 |
| Mo | 42 | 4.98 | 14.6 |
| Cd | 48 | 4.98 | 20.8 |
| Sb | 51 | 4.98 | 13.7 |

Several absorbers were placed in the beam to control the interaction rate. The actual incident flux was not of major concern since the experiment involved only the high-energy gamma rays required for pair production and since the flux strength would be eliminated by taking the ratio of triple-coincidence data to the number of 511-keV twofold coincidences recorded. The electronics for the fourfold coincidence investigation were used once more. The TAC was started on the condition of coincident detection of annihilation quanta in the two start-side quadrants but was stopped by the widened fast-logic pulse associated with one of the stop-side quadrants. Use of the TAC permitted an investigation of chance events. The pulse-height spectra from the TAC and the stop-side quadrants were then fed to two ADCs and a two-parameter analysis conducted using a Nuclear Data 3300 analyser. Since no structure was to be expected in the bremsstrahlung spectra, a 128×128 memory configuration was employed, and data were collected for several hours for each target. The gain of the stop-side amplifier used was of course changed to accommodate events of energy a little greater than the maximum possible energy of 5.6 MeV. Several quantities of interest, including the number of start events and the analyser live time, were recorded.

Energy calibration of the system was achieved in part by using the aforementioned stop-side quadrants and electronics to examine the emanations from a $^{22}$Na source. However, since 1.27 MeV98) was the highest gamma-ray energy from $^{22}$Na, another source was needed to calibrate the system up to 5.6 MeV. The most suitable source that could be obtained was $^{49}$Ca which decays to give[98)] a 3.1-MeV gamma ray 89% of the time, a 4.1-MeV gamma ray 10% of the time, and a 4.7-MeV gamma ray for only 0.3% of the time. The $^{49}$Ca source was made by irradiating 0.5 gm of calcium carbonate with a flux of $10^{13}$ thermal neutrons/cm$^2$/sec for 1 minute. Following neutron activation of $^{48}$Ca, the source was allowed to decay for a short time to eliminate the short-lived activities, associated with other nuclides, before the sample could be handled. The half-lives corresponding to the other active nuclides were typically of order of several seconds compared to the half-life of 8.8 minutes[98)] for $^{49}$Ca. The source was then positioned within the annulus and an energy calibration obtained in a standard fashion.

# CHAPTER V

# EXPERIMENTAL RESULTS AND ANALYSES

## 5.1 ABSOLUTE MEASUREMENT OF GAMMA-RAY FLUX

The data acquired during this experiment are presented graphically in figure 5-1. The feature corresponding to Compton scattering of 6.6-MeV gamma rays, on average, is located in the neighbourhood of channel number 180. The small amount of structure within this feature can be attributed to the scattering of gamma rays of energy ~~6417, 6557,~~ and 6762 keV. Other features in the spectrum are also understandable. For instance, the peak at channel number 38 corresponds to 511-keV photons from positron annihilation within the aluminum scatterer. This peak was unaffected in the subtraction mode of the experiment since the view afforded the detector no longer encompassed the aluminum plate. For the same reason, the peak at channel number 75, corresponding to Compton scattering of 1.38-MeV gamma rays in the incident beam, shows no evidence of subtraction. By contrast, the dip at channel number 93 can be associated with the subtraction of events arising from decay of $^{41}$Ar($E_\gamma \sim 1.29$ MeV) within the air of the reactor building. The slight over-subtraction in this

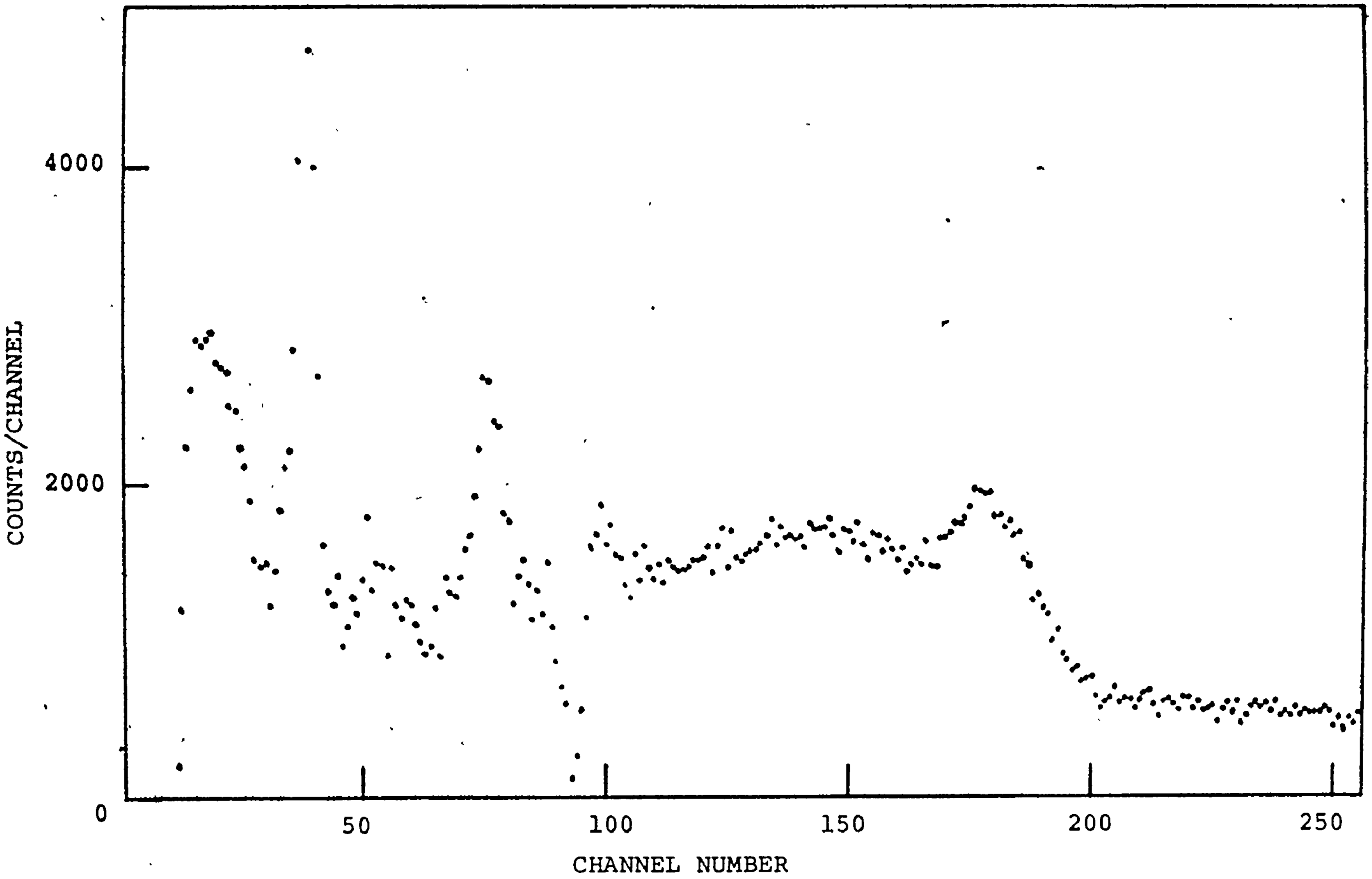

FIG. 5-1 SPECTRUM FROM COMPTON SCATTERING OF GAMMA BEAM

region stems in part from the fact that in the second half of the experiment the field of view of the detector no longer contained an aluminum attenuator.

The first part of the analysis of the data required that the total number of counts included in the peak at channel number 180 be determined. The region between channel numbers 173 and 247 was therefore fitted by means of a non-linear least-squares code to a model consisting of a Gaussian distribution for the peak and a straight line for the background. The centroid of the peak was determined by this model to be located at channel number 177.98. In accordance with a method indicated by Heath97), the background was then fitted to a straight line, in the region of channel number 205 to channel number 247, for extrapolation into the region of the peak of interest. The number of counts in excess of the linear model of the background was calculated for that part of the peak to the right of the centroid, and then doubled. The total content of the peak was thus extracted as 28859±359 counts. This value was corroborated somewhat by statistical agreement with the content found via the original Gaussian model.

The energies noted in figure 5-1 were obtained by calibration of the system with $^{22}$Na and $^{56}$Co sources. The calibration spectra are shown in figures 5-2 and 5-3. Since it is well known that the pulse-height response of a NaI(Tl) detector to gamma rays of different energies is not linear, the relation-

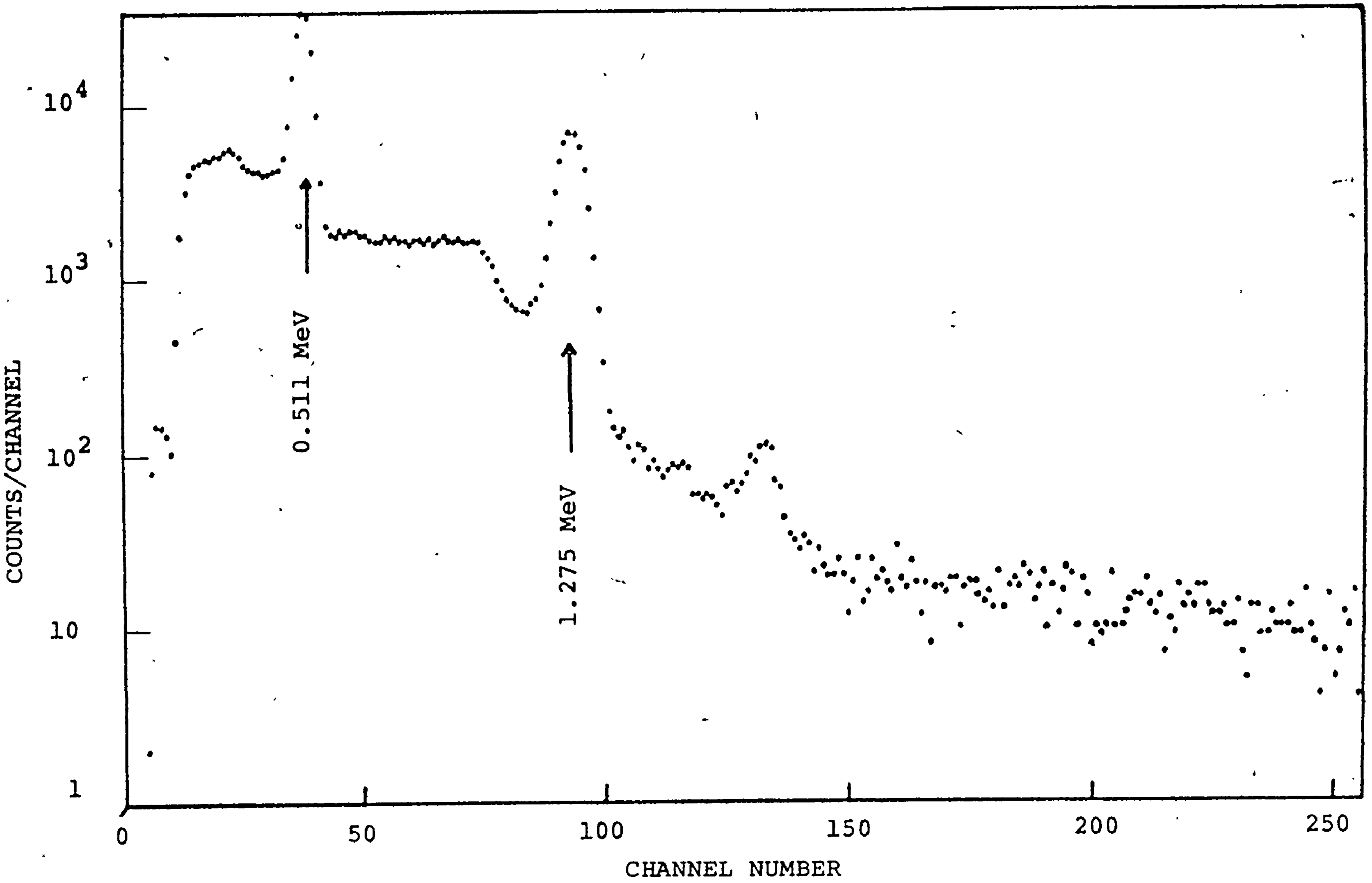

FIG. 5-2 SPECTRUM FROM $^{22}$Na FOR ENERGY CALIBRATION

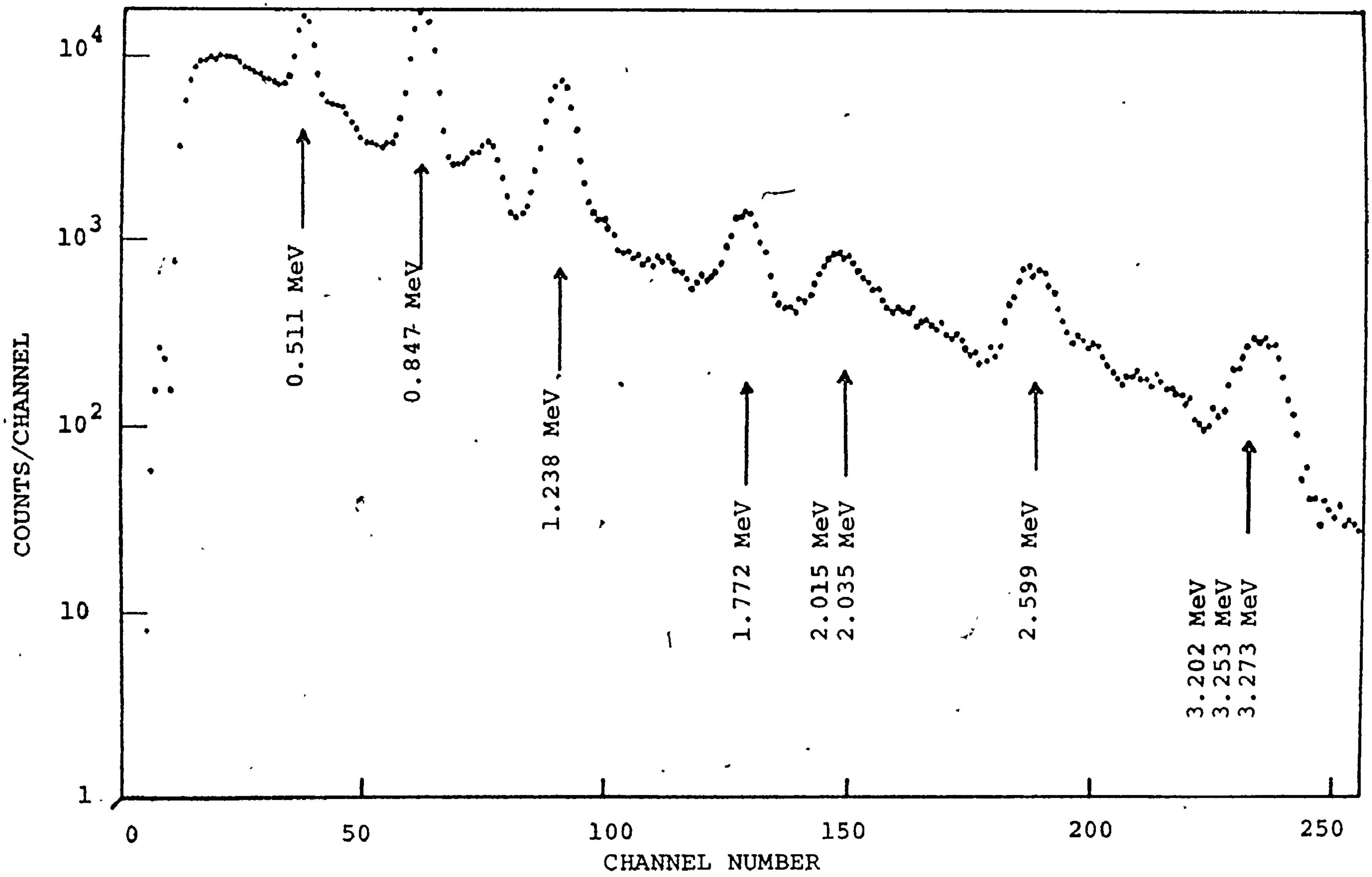

FIG. 5-3 SPECTRUM FROM $^{56}$Co FOR ENERGY CALIBRATION

ship between energy and channel number was modelled by the least-squares method to a polynomial. The resulting weighted fit of the data to the model can be expressed as

$$E = -1.05017 + 13.156986X + 0.007013X^2 - 0.17664\times10^{-4}X^3 , \quad (5.1)$$

where X stands for channel number and E represents energy in units of keV. The centroid of the distribution of Compton events was found to correspond to 2.46 MeV, by application of equation (5.1). Thus the average angle of scattering was inferred, via equation (2.46), to be approximately 29.5 degrees.

The second part of the experimental analysis required that the fraction of 6.6-MeV gamma rays scattered into the detector be calculated. A realistic picture of the experimental geometry is presented in the scaled diagram of figure 5-4. Several accurate measurements were needed for the calculation. The aluminum thickness t was measured, by micrometer, as 0.6365±0.00005 cm, the collimator diameter as 3.81±0.01 cm, and the lengths TD, TS and DS in the diagram as 83.8±0.1 cm, 96.2±0.1 cm and 46.8±0.1 cm respectively. The angle of scattering was then estimated as 29.2, 29.1, and 29.4 degrees from the above measurements and the respective definitions of arctan, arcsin and arccos. The angle was also measured directly as 29.3 degrees. It therefore seemed reasonable to accept the average value of 29.3±0.2 degrees. By contrast, the orientation of the aluminum plate with respect to the beam direction could only be measured, at best, as 60±1 degrees.

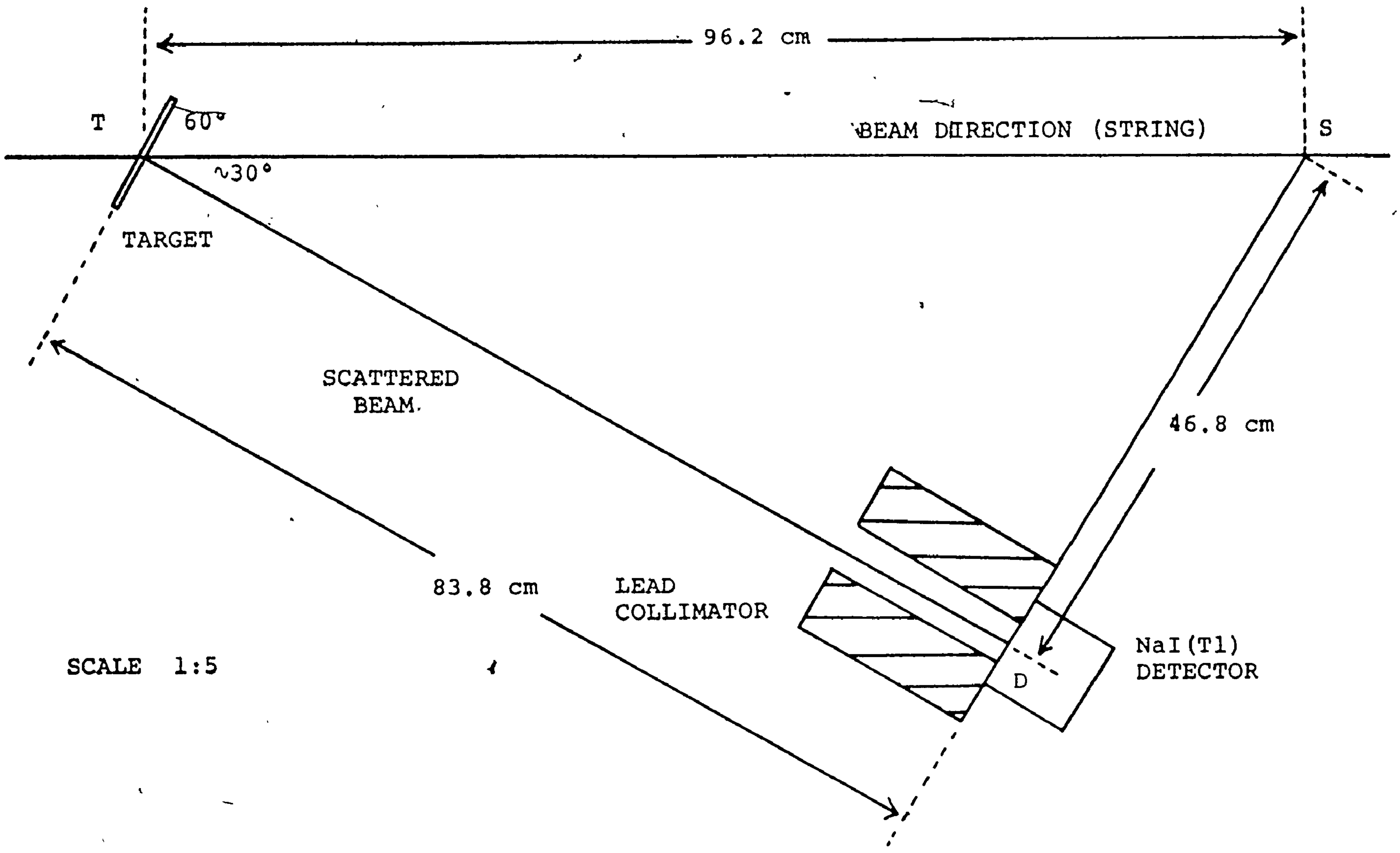

FIG. 5-4 SCALED DIAGRAM OF EXPERIMENTAL GEOMETRY FOR FLUX MEASUREMENT

The calculation was conducted under several simplifying assumptions.

1. The gamma rays in the incident beam were assumed to have the average energy of 6.6 MeV.
2. The angle of scattering was taken as the average value of 29.3 degrees.
3. The total interaction rate of the incident beam with the aluminum scatterer was assumed to be concentrated at a point in the middle of the target. This followed from the probability of interaction with the target being small for both the incident and the scattered gamma rays.
4. The scattered beam was assumed to strike the face of the NaI(Tl) detector at right angles. This amounted to ignoring a spread of up to ± 1.3 degrees about perpendicularity.

In a later, more complicated, calculation in which the aluminum plate and the surface of the NaI(Tl) detector were treated as if divided into many small sections, the total change introduced by the above assumptions was found to be $\sim 0.5\%$. The simpler model was therefore used since the error involved was of little consequence when compared with the 5% uncertainty involved in listed values[99)] of necessary cross sections.

The reaction rate was therefore estimated as

$$R = 1 - \exp(-\mu_1 t/\cos 30°), \qquad (5.2)$$

with $\mu_1$ representing the linear coefficient for absorption of 6.6-MeV photons by aluminum. The self-absorption factor for the target was taken to be

$$S = \exp(-\mu_2 t/2) , \tag{5.3}$$

where $\mu_2$ stands for the linear coefficient of absorption for the scattered radiation in aluminum. The fraction of events scattered into the detector was assumed to be

$$F = Z\left(\frac{d\sigma}{d\Omega}\right)_{29.3°} \frac{\Delta\Omega}{\sigma_T} \quad . \tag{5.4}$$

Here Z is the atomic number of aluminum, $(d\sigma/d\Omega)$ is the Klein-Nishina formula (equation (2.50)) applied for a scattering angle of 29.3 degrees, $\Delta\Omega$ is the small solid angle extending from the scatterer to the back of the collimator aperture, and $\sigma_T$ is the total interaction cross section for 6.6-MeV gamma rays in aluminum. The interaction rate of the scattered radiation with the 3-inch NaI(Tl) detector was expressed as

$$I = 1 - \exp(-7.62\ \mu_3) \tag{5.5}$$

where $\mu_3$ is the linear coefficient for absorption of the scattered radiation by NaI. In total then, the probability of an event being found in the appropriate full-energy peak was estimated as

$$P = pRSFI \tag{5.6}$$

where p represents the photo-fraction of 0.236 deduced from the curves of Heath[97)] for a 3-inch NaI(Tl) detector. The flux of 6.6-MeV gamma rays could therefore be simply calculated from the measured value of M counts/sec as

$$\phi_\gamma = M/P. \tag{5.7}$$

In order to make the discussion of the above calculation factually complete, mention must be made of a first-order correction for transmission of the scattered radiation through small thicknesses of the lead collimator. This was viewed as introducing a small enlargement of the solid angle between the point-source scatterer and the detector. The geometry for the calculation is illustrated in figure 5-5. The path length through the lead can be seen to be

$$L = \left(\frac{r-R}{\sin\theta}\right) \tag{5.8}$$

$$= (r-R)\,\frac{\sqrt{r^2+(TD)^2}}{r} \quad . \tag{5.9}$$

If unit flux is considered to be incident within the collimator aperture the flux per unit area can be approximated by

$$\frac{d\phi}{dA} = \frac{1}{\pi R^2} \quad . \tag{5.10}$$

If it is assumed that the same intensity of flux would strike the detector, outside the radius R, but for the lead shielding, the transmission through the walls of the collimator can be approximated by

$$T = \int \frac{dA}{\pi R^2} \exp\{-\mu_4 L\} , \tag{5.11}$$

$$= \int_R^{R_1} \frac{2rdr}{R^2} \exp\{-\mu_4 (r-R)\sqrt{r^2+(TD)^2}/r\} , \tag{5.12}$$

where $\mu_4$ is the linear absorption coefficient for the scattered

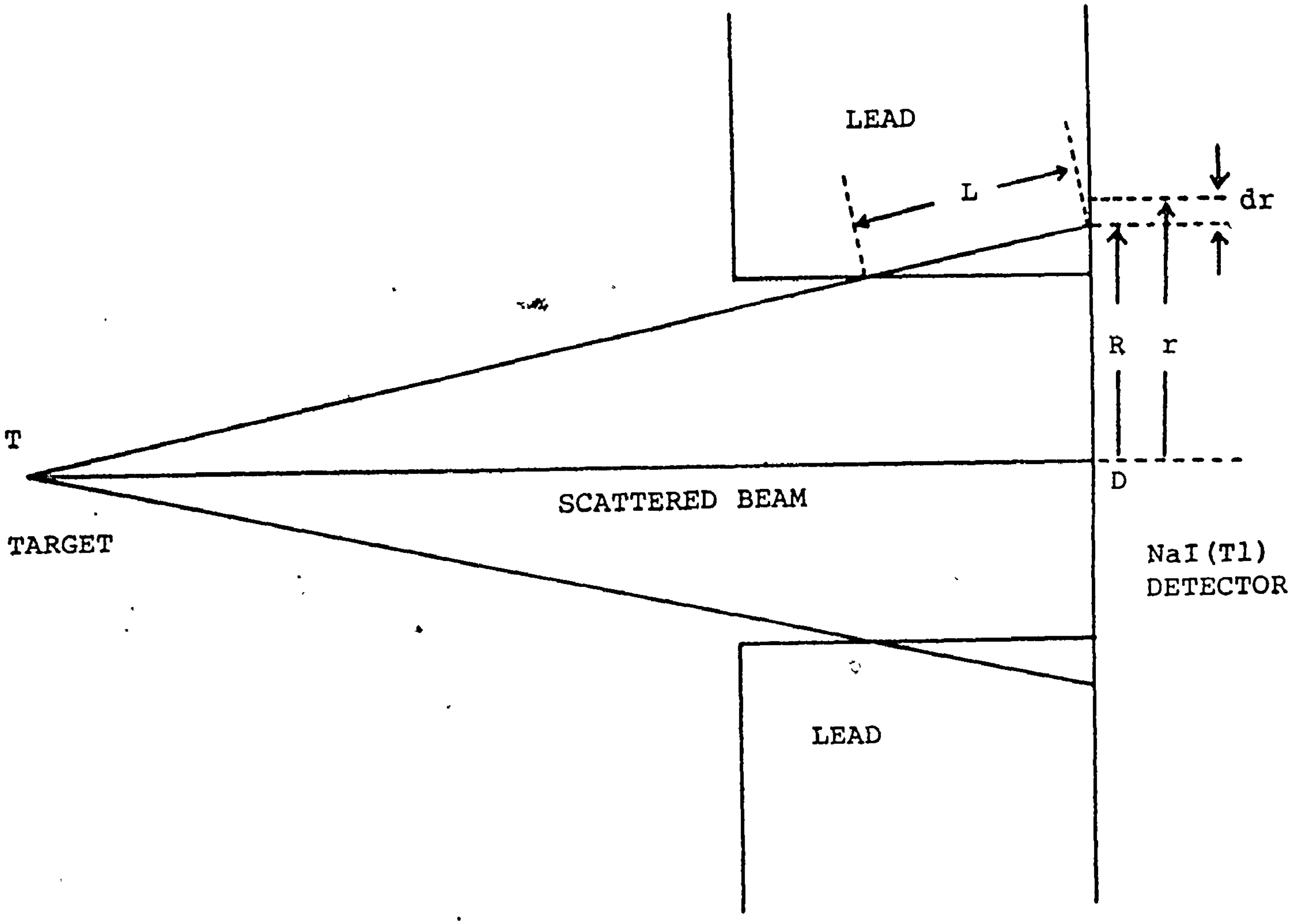

FIG. 5-5 GEOMETRY FOR CALCULATION OF TRANSMISSION THROUGH LEAD COLLIMATOR

radiation in lead, and $R_1$ is the maximum radius for significant contribution to the integral.

When all of the above aspects were taken into account, the measured rate of 28859±359 counts/400 minutes, or 1.202±0.015 counts/sec, was found to correspond to a flux of 6.6-MeV gamma rays of $(5.36 \pm 0.32) \times 10^5$ per second. This value must of course be interpreted as the flux for conditions of no concrete absorbers in the beam and the reactor operating at a 5-MW level of power.

## 5.2 FLUX MONITOR

The response of the flux monitor to changes in reactor power was investigated by multiscaling the output pulses from the monitor while stepping the power slowly from 0 to 5 MW. The dwell-time in consecutive channels of the analyser was measured as 8.812 seconds, within negligible error, by scaling the address-advance pulses. Although the errors in power settings are not truly known, it has been estimated by the reactor staff that the length of time allowed for stabilization at each step in power permitted achievement of an accuracy of order of 1%. The data collected during this experiment are presented in figure 5-6.

Several of the features seen in figure 5-6 are to be noted. A long extent of low level but constant counting rate, corresponding to zero reactor power, can be seen previous to the onset of the increments in power. Since the reactor had been shut down for approximately one day before the start of

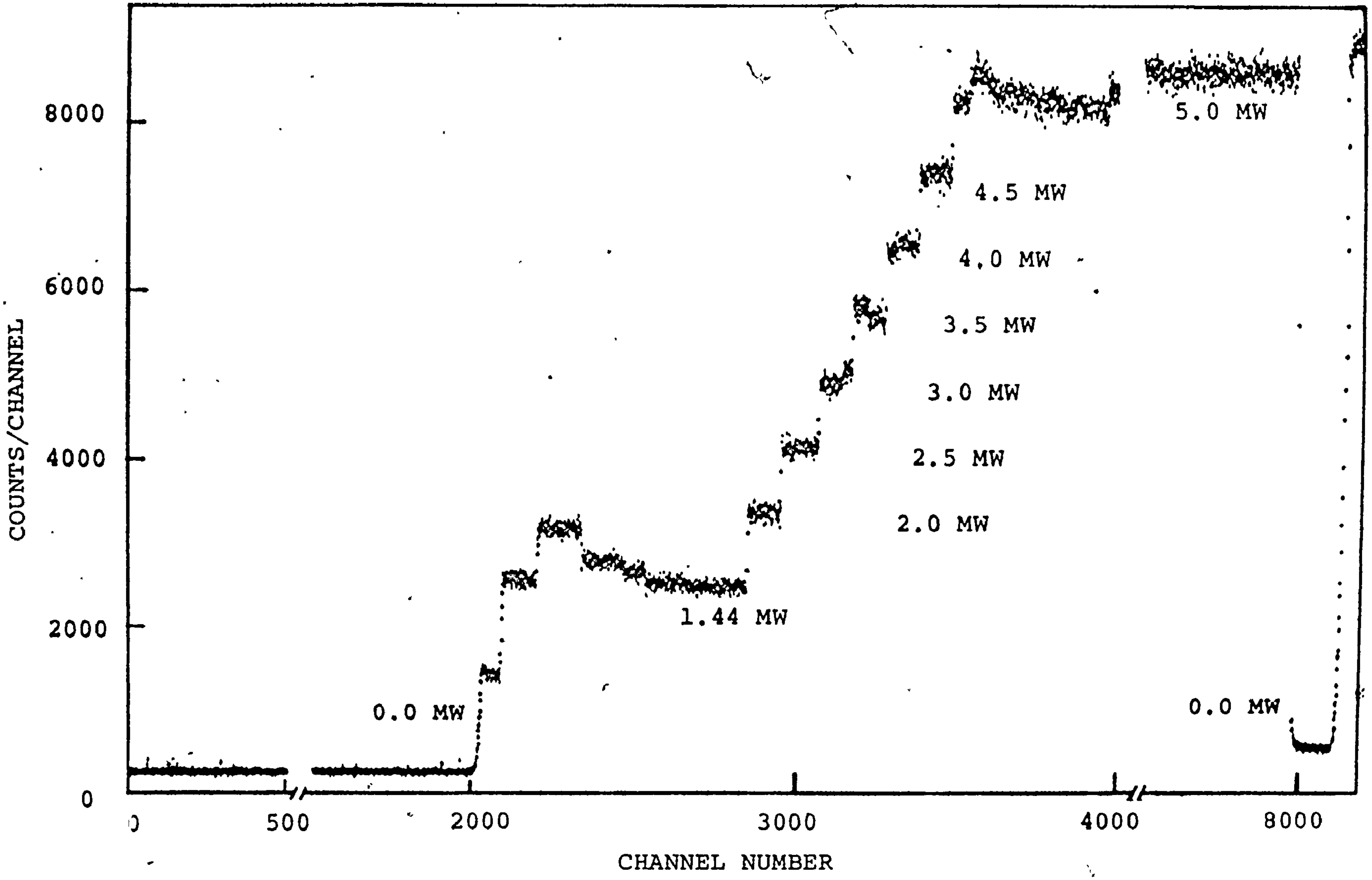

FIG. 5-6 DATA FROM MULTISCALING OF FLUX-MONITOR OUTPUT

this investigation, practically all of the 109.8-minute activity from $^{41}$Ar had disappeared. The low counting rate observed is ascribable to activity from the surrounding walls, shielded sources in the neighbourhood of the monitor, and long-lived residual activity associated with the tangential irradiation facility itself. The steps in power and the quality of power stability at each level can also be seen. The final level, which corresponds to 5 MW of power, was maintained for approximately 660 minutes. The sharp dip towards the end of the 660 minute duration is associated with a reactor "scram" in which the reactor power dropped almost instantaneously to zero. The difference in the number of counts/channel registered at that time of zero power and those registered during the initial zero power level give indication of the $^{41}$Ar activity associated with a reactor power of 5 MW.

The data shown in figure 5-6 were analysed by finding the average number of counts/channel for several channels associated with each level of power. To enable the extraction of information relevant to the gradual increase in $^{41}$Ar activity ($T_{1/2}$ = 109.8 m), the channels used in the averaging procedure were always chosen as corresponding to relatively small durations of time towards the end of each period of operation at a different level of power. The various reactor powers and the associated average number of counts per channel are shown in the first two columns of table 5-1. The final column presents data corrected for both the constant general background activity and also that due to $^{41}$Ar in the air. Correction was achieved

## TABLE 5-1 DATA FROM FLUX MONITOR

| Power (MW) | <Counts>/Channel | Corrected <Counts>/Channel |
|---|---|---|
| 0.00 | 239.8±0.4 | 0.0 |
| 1.44 | 2524.6±5.5 | 2251.3±5.6 |
| 2.00 | 3410.1±8.6 | 3134.5±8.7 |
| 2.50 | 4197.1±9.6 | 3919.1±9.7 |
| 3.00 | 5100 ±14 | 4820 ±14 |
| 3.50 | 5742 ±14 | 5460 ±14 |
| 4.00 | 6588 ±17 | 6304 ±17 |
| 4.50 | 7466 ±14 | 7180 ±14 |
| 5.00 | 8511.5±7.1 | 8046.6±8.9 |
| 0.00 | 464.9±5.4 | 0.0 |

as follows.

The constant background was first subtracted from the data recorded in the second column. The 225.1 counts/channel remaining from the final datum was treated as arising from the concurrent creation and decay of $^{41}Ar$ in accordance with the equation

$$N = PK[1 - \exp(-0.693t/T_{1/2})]. \qquad (5.13)$$

Here N represents the counts/channel, P the power in megawatts, K a constant of proportionality, t the length of time during which the power was applied,and $T_{1/2}$ the 109.8-minute half-life of $^{41}Ar$. Since the power level of 5 MW was maintained for greater than six half-lives the $^{41}Ar$ activity had effectively achieved its saturation value. Consequently, application of equation (5.13) gives

$$5K = 225. \qquad (5.14)$$

From this it can be clearly seen that the constant of proportionality, K, must have the value 45. The correction for $^{41}Ar$ activity was achieved in the case of the 5-MW level by subtracting the 225 counts/channel from the associated datum. For the other levels of power the correction term was calculated from

$$\Delta N = 45\ \Delta P[1-\exp(-0.693t/T_{1/2})], \qquad (5.15)$$

where ΔN and ΔP are the respective increments in the number of counts/channel and reactor power, and t represents the duration of the appropriate step in power. Since the argon activity was obviously accumulative, the term for subtraction was also taken to be accumulative.

The final corrected data are shown in figure 5-7 plotted against reactor power. The solid curve was obtained by modelling the relationship to a straight line in a least-squares calculation. The variance-covariance analysis indicated a slope of 1593.7±7.4 counts/channel/MW, an intercept of -0.2±2.4 counts/channel, and a general error in the fitted line of less than 0.5%. It can be seen that the adjudgement of a 1% error in the power level, by the reactor staff, is consistent with the data graphed in figure 5-7 where vertical error bars are no bigger than the size of the dots shown.

A general relationship between counts/channel recorded from the monitor and reactor power can be written to include the constant background component and the saturation $^{41}$Ar activity, for no absorbers in the beam, as

$$N = 240 + 45P + 1594P \, . \qquad (5.16)$$

Since the monitor output pulses were merely scaled in subsequent experiments, equation is better restated in terms of recorded rate, in units of counts/sec, as

$$R = (240 + 1639P)/8.812. \qquad (5.17)$$

Consequently the average power during an experiment in which no concrete absorbers were used, can be predicted as

$$P(o) = 0.00538R - 0.146. \qquad (5.18)$$

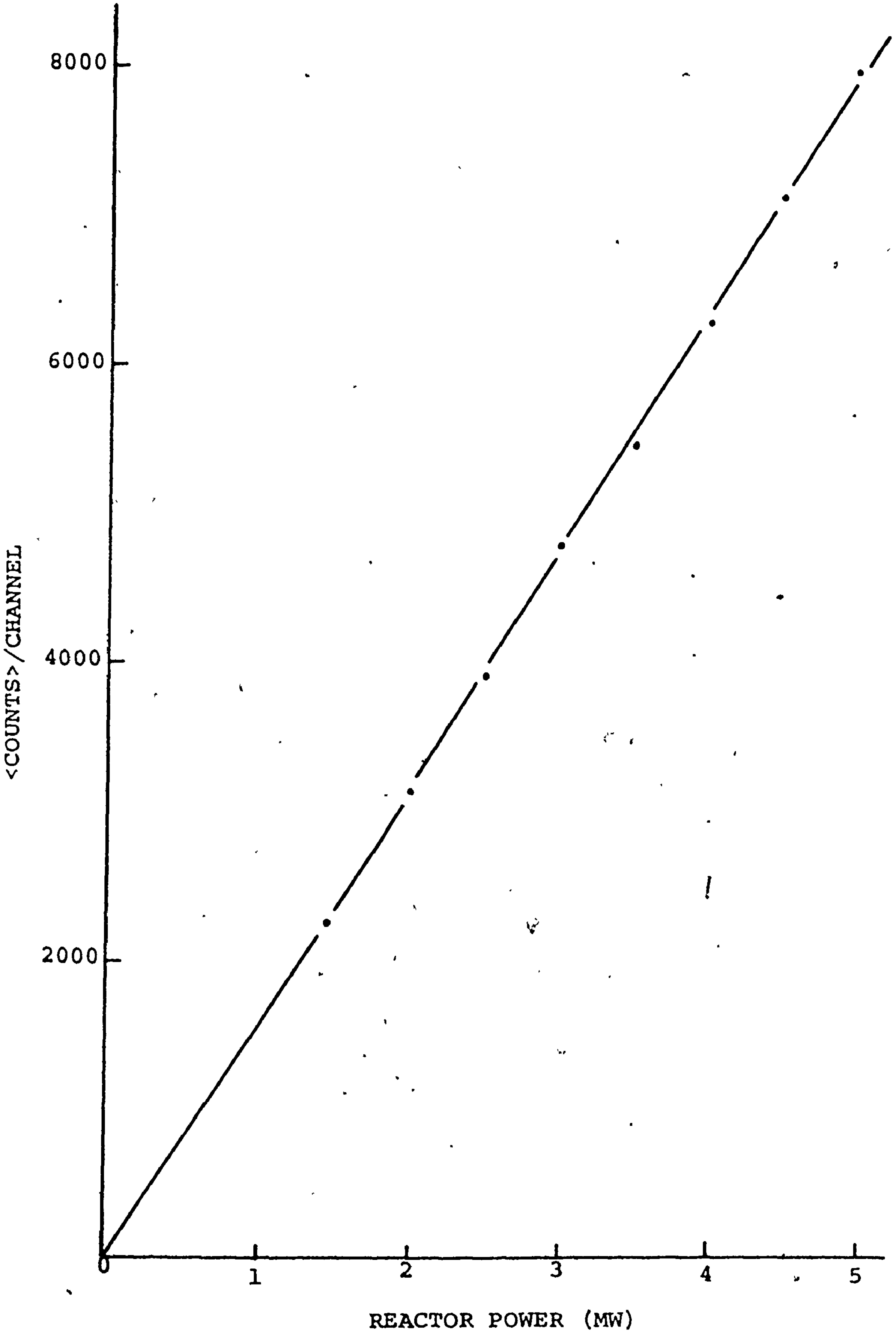

FIGURE 5-7 LINEARITY OF RESPONSE OF POWER MONITOR

In reality then, application of equation (5.18) leads to the monitor being interpreted as a power monitor instead of a monitor of the flux of 6.6-MeV gamma rays. However, although a portion of the monitor rate stems from undesirable events, a linear relationship between the flux of 6.6-MeV photons and the reactor power can safely be assumed. Therefore, the result of the absolute flux measurement discussed in section 5.1 can be taken into account to give the flux of 6.6-MeV gamma rays, for a condition of no absorbers in the beam, as

$$\phi_\gamma(o) = \left(\frac{5.36\pm0.32}{5}\right)P(o)\times10^5 \qquad (5.19)$$

gamma rays per second. Since errors propagate in quadrature, the assumption of a 1% error in the average power calculated via equation (5.18) has little effect on the original error in the value of the absolute flux.

In order to measure the effect of the concrete absorbers on the power monitor, the number of attenuators was varied from none to three while the reactor power was kept at a constant nominal level of 5 MW, and the monitor rate scaled in each instance. It was reasoned that the multiscaling procedure was not required in this part of the experiment since the relationship between the corrected average number of counts per channel and reactor power was already established as linear. Consequently it was believed that the introduction of different numbers of concrete attenuators into the beam would merely lead to curves similar to that shown in figure 5-7, but with smaller slopes. The monitor rates for no absorbers up to three absorbers were measured to be respectively, 1019.8, 880.5, 714.2, and 562.1 counts per second. Since these rates were to be used in a relative fashion, it was not important that the power available was only approximately 5 MW. In brief, when background and $^{41}$Ar activities were taken into account expressions for the average power, in terms of the monitor rate, were developed for geometries including a set number of absorbers. The equations are

$$P(1) = 0.00626\ R - 0.171, \tag{5.20}$$

$$P(2) = 0.00778\ R - 0.212, \tag{5.21}$$

and

$$P(3) = 0.01000\ R - 0.272. \tag{5.22}$$

However, conversion of these equations to ones which express the 6.6-MeV gamma flux, under the respective conditions, must await results which will be discussed in section 5.5.

## 5.3 EFFICIENCY AND DEAD-TIME MEASUREMENT

In this experiment many sets of data were collected in accordance with the procedure outlined in section 4.3 for following the decay of $^{18}$F. A typical set of data acquired with the analyser in the MPA-SS mode is shown in figure 5-8. The figure is basically composed of singles spectra presented along the two base axes and a coincidence spectrum throughout the remaining domain. The large peak found in the vicinity of channel number 18 in each singles spectrum corresponds to 511-keV events. The peak resulting from the coincident detection of 511-keV quanta

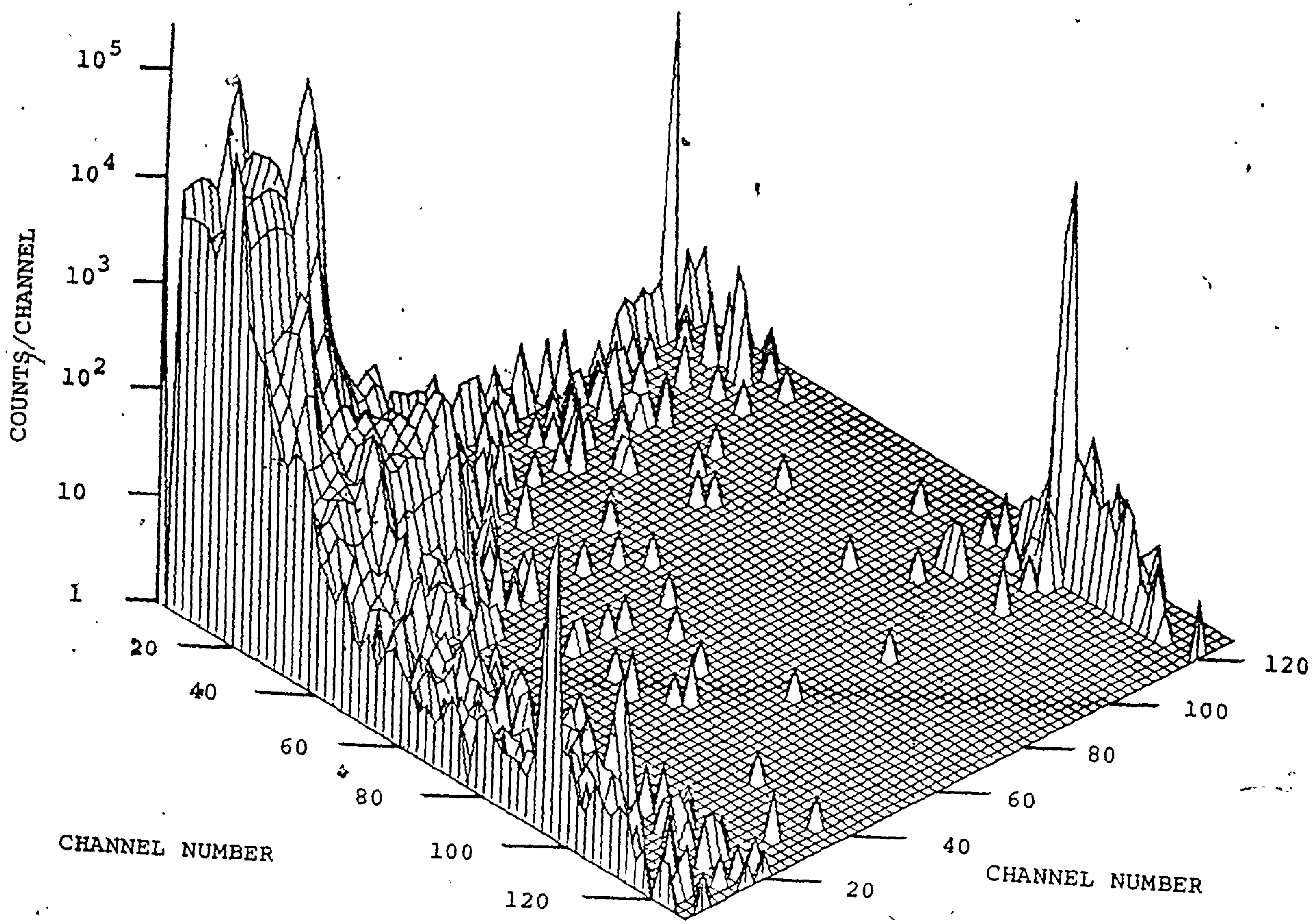

FIG. 5-8 TYPICAL SPECTRUM FROM FLUORINE EXPERIMENT.
The data correspond to a mean time of 1349 minutes.

is clearly seen in the coincidence spectrum. Similarly it can be pointed out that the peaks found isolated at much higher channel numbers correspond to pulser events. The other peaks which are noticeable arise from Compton scattering of the 511-keV photons. In particular, when a 511-keV quantum is back-scattered in one NaI(Tl) quadrant it can leave behind 341 keV of energy while exiting with 170 keV of energy which may possibly be deposited in the opposite quadrant. Thus one can expect peaks in the singles spectra associated with energies of 170, 341, 511 and 681 keV. The 341-keV "peak" is really a Compton edge and the 681-keV feature arises from coincidence summing of the energies of 170 and 511-keV photons. Consequently, in addition to the large 511-511-keV peak seen in the coincidence spectrum, one can expect to perhaps see small prominences which can be ascribed to 170-170, 170-341, 341-341, 341-511, and 341-681-keV coincidences.

The coincidence-summing effect mentioned above is inherent to all experiments in which a source of annihilation quanta is positioned within the NaI(Tl) annulus. Furthermore, since the fraction of 511-keV events lost to coincidence summing is independent of the rate of annihilation, all experiments involving similar geometries will suffer to essentially the same extent. Therefore the incidence of coincidence summing, which can be seen from figure 5-8 to be relatively negligible, is effectively included in efficiency considerations.

However, the possibility of random-summing effects is not so quickly dismissed. A small amount of random summing can be detected in figure 5-8 in the neighbourhood of the isolated pulser peaks. Although the effect is clearly small, the fact that it is rate dependent necessitates a closer examination. It is well known that, to a first-order approximation, the fractional loss to random summing is given by

$$F_s = 2N_s\tau \ , \tag{5.23}$$

where $N_s$ is the rate of singles events and $\tau$ is the resolving time. Therefore, for a coincidence experiment in which singles rates are not excessive, and in which the two detection channels are identical, the fraction of events lost to random summing can be written as

$$F_C = 4N_s\tau \ . \tag{5.24}$$

The number of events in the immediate vicinity of the coincidence pulser peak was therefore ascertained for each collection of data to determine the fraction of the total number of pulser events lost to the effect. An estimate of the resolving time was then obtained via equation (5.24) and the scaled stop (singles) rates. The appropriate numbers are shown in table 5-2 where the mean time for each experiment is given as relative to some arbitrary start time, and the errors in the singles rates are negligible. Since the duration of each counting period (∿ 4 to 10 minutes) was much smaller than the half life of $^{18}F$ (109.8 minutes), the central time could be used with considerable accuracy as the time-reference for each experiment. The calculated resolving times are relatively constant and give rise to a weighted average value of 0.76±0.02 microseconds. This compares favourably with the 0.75 μs clipping time of the DDL amplifiers involved, as predicted by Kennett et al[100]. Therefore it can be seen from equation (5.23) that even for a count rate as high as $10^4$ cps the fractional loss of events to random summing is effectively negligible (∿ 1.5%).

In order to investigate possible dead-time effects, it was necessary to determine the content of the 511-511-keV coincidence peak in each set of acquired data. This required the subtraction of a two dimensional background in each instance. To that end, each coincidence spectrum was considered to be composed of several one-dimensional spectra each corresponding to a channel number in the other dimension. The content of the full-energy peak in each of the one-dimensional spectra was ascertained by fitting the background content to a polynomial. The same bounds for the 511-keV peak were used throughout the procedure. Both this and the polynomial modelling of the background ensured a high degree of objectivity. The result of stripping off the background in one dimension is typified in figure 5-9. The content of the full-energy coincidence peak was then extracted by fitting the small residual background content, in the other dimension, to a polynomial. The information extracted in the above fashion is presented in the second column of table 5-3 where the observed full-energy coincidence rate is given as counts per minute of analyser live time. The errors listed in this column are solely statistical. These data are shown as dots in figure

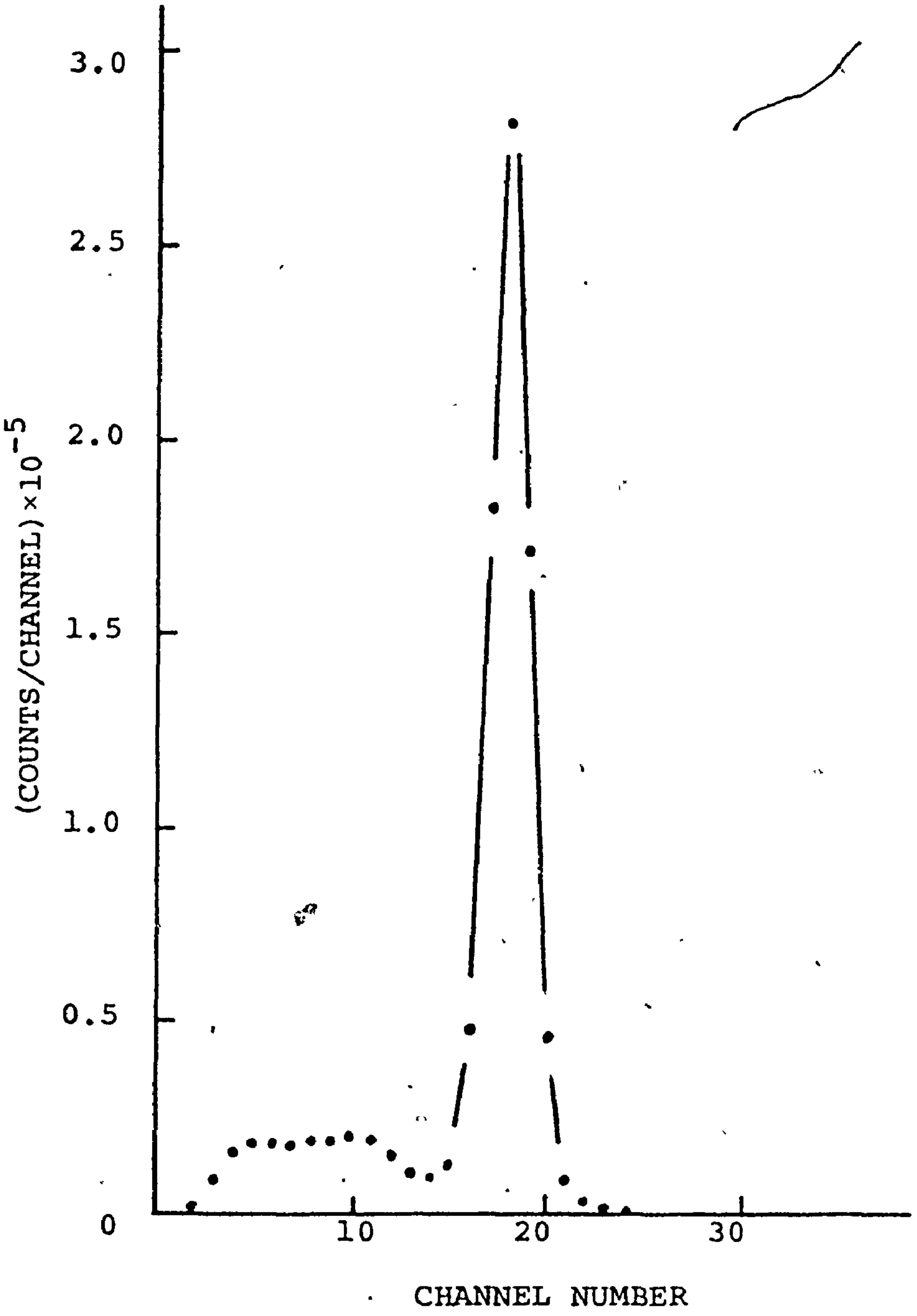

FIG. 5-9 FLUORINE COINCIDENCE SPECTRUM AFTER STRIPPING IN ONE DIMENSION. Data correspond to a mean time of 1349 minutes.

TABLE 5-2 RESOLVING TIME FOR RANDOM-SUMMING LOSSES

| Mean Time (minutes) | Singles Rate ($10^3$ cps) | % Loss in Pulser Coincidence Rate | Resolving Time τ (μs) |
|---|---|---|---|
| 1056.8 | 58.3 | 17.8 ±0.8 | 0.76±0.03 |
| 1160.7 | 33.2 | 9.3 ±0.6 | 0.70±0.04 |
| 1206.9 | 25.6 | 7.7 ±0.5 | 0.76±0.05 |
| 1247.1 | 20.3 | 6.1 ±0.4 | 0.75±0.05 |
| 1299.8 | 15.0 | 4.1 ±0.3 | 0.69±0.04 |
| 1349.4 | 11.3 | 4.0 ±0.3 | 0.87±0.06 |
| 1399.1 | 8.63 | 2.6 ±0.2 | 0.74±0.06 |
| 1463.9 | 6.16 | 2.1 ±0.2 | 0.84±0.07 |
| 2096.8 | 1.07 | 0.55±0.07 | 1.28±0.15 |
| 2112.8 | 1.02 | 0.42±0.06 | 1.04±0.14 |

## TABLE 5-3 COINCIDENCE RATES FROM DEAD-TIME INVESTIGATION

| Mean Time (minutes) | Observed Coincidence Rate $R_o$ ($10^3$ cpm) | True Coincidence Rate $R_T$ ($10^3$ cpm) | $R_o/R_T$ |
|---|---|---|---|
| 1056.8 | 868.7±1.1 | 1163 ±18 | 0.747±0.012 |
| 1160.7 | 531.6±0.8 | 603.6±9.3 | 0.881±0.014 |
| 1206.9 | 414.2±0.7 | 451.0±6.9 | 0.918±0.014 |
| 1247.1 | 329.6±0.6 | 349.8±5.4 | 0.942±0.015 |
| 1299.8 | 241.9±0.4 | 250.9±3.9 | 0.964±0.015 |
| 1349.4 | 178.2±0.3 | 183.4±2.8 | 0.972±0.015 |
| 1399.1 | 132.0±0.3 | 134.0±2.1 | 0.985±0.016 |
| 1463.9 | 88.3±0.7 | 89.0±1.4 | 0.992±0.018 |
| 2080.4 | 1.85±0.03 | 1.82±0.03 | 1.017±0.024 |
| 2096.8 | 1.59±0.03 | 1.64±0.03 | 0.970±0.025 |
| 2112.8 | 1.50±0.03 | 1.48±0.02 | 1.014±0.025 |

5-10 where the observed coincidence rate is plotted against mean time. The last three data in the second column of table 5-3 were used to determine the least-squares exponential decay curve since it was obvious that no losses in rate were experienced at the corresponding mean times and since the half-life of decay was known to be 109.8 minutes. The amplitude at zero mean time for the fitted exponential was found to be $(91.83\pm1.41)\times10^7$ cpm. True coincidence rates were then evaluated at the appropriate mean times and listed in the third column of table 5-3. The ratios of the observed to the calculated full-energy coincidence rates are also listed. Comparison of the fractional loss of events expressed in these ratios with the appropriate results in column three of table 5-2 reveals that losses can largely be explained in terms of random summing. Although it is realized that the complete spectrum of random-summing events should be considered, if one assumes that the percentage losses listed in table 5-2 can be used directly to take into account random-summing losses from the 511-511-keV coincidence peak, the only statistically significant losses remaining are the 7.5±1.4% and 2.6±1.5% associated with mean times of 1056.8 and 1160.7 minutes respectively. One can treat these as losses attributable to dead-time effects in a paralysable system by application of the equation

$$R_{OD} = R_{TD}\exp(-R_{TD}T_D) \quad , \qquad (5.25)$$

in which the observed rate, $R_{OD}$, is related to the true rate, $R_{TD}$, and the resolving time, $T_D$, for dead-time effects. Equation (5.25)

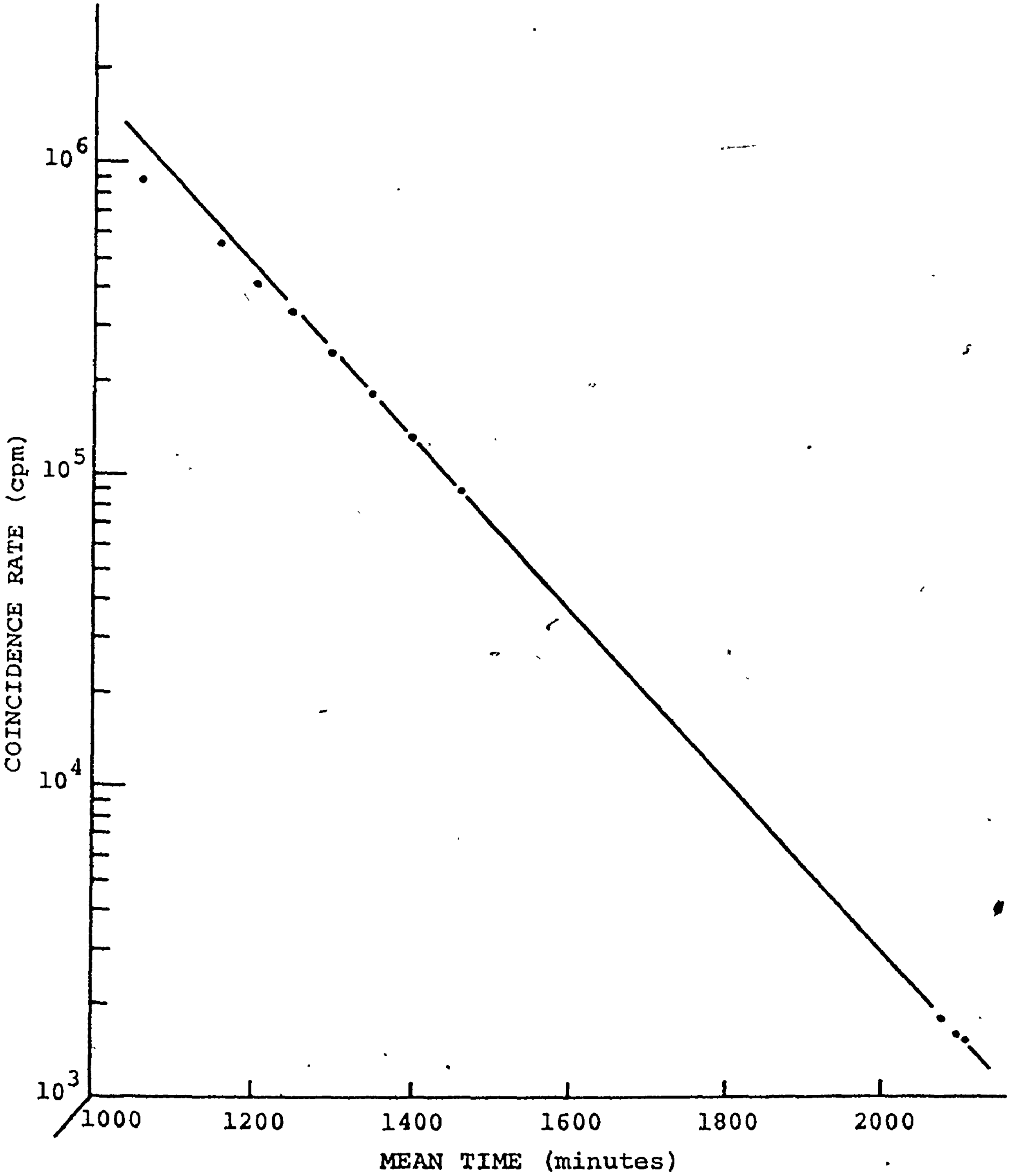

FIG. 5-10 DECAY OF FLUORINE COINCIDENCE RATE WITH TIME. The solid line represents the true variation in coincidence rate with time for $^{18}F(T_{1/2}=109.8\ m)$.

was therefore used, for fractional losses of 0.075 and 0.026 and true rates of $1163 \times 10^3$ and $603.6 \times 10^3$ counts per minute respectively, to obtain estimates of the constant $T_D$. The weighted average of the resolving times was found to be 3.5±0.5 μs.

The contention that only the first two ratios of $R_O/R_T$ in table 5-3 showed statistically significant losses from dead-time effects was dramatically supported by an investigation of the pulser events in the coincidence spectra. It was reasoned that if all coincident pulser events were counted, including those displaced from the isolated pulser peak by random summing, any deviation from a constancy of pulser rate would be ascribable to dead time within the detection system. The results of these considerations are shown in table 5-4. It is self-evident from the table that a fairly constant pulser rate exists from the mean time of 1206.9 minutes onwards. Dead-time losses were therefore calculated about the weighted average value of 3642.5±2.7 counts per minute. It is clear that only the first two entries in the table show effective dead-time losses. Analysis of these for resolving times leads to the average value for $T_D$ of 4.8±1.2 μs.

However, the question of which complication led to which percentage loss is really academic since care was taken to limit the rates involved in subsequent experiments. As a result, the maximum total correction required was less than 5%. Small first-order corrections were made to all experimental results although almost invariably they fell within inherent experimental errors.

TABLE 5-4 DEAD-TIME LOSSES

| Mean Time (minutes) | Total Pulser Coincidence Rate (cpm) | Dead-Time Losses (%) |
|---|---|---|
| 1056.8 | 3246 ±17 | 10.89±0.47 |
| 1160.7 | 3527 ±13 | 3.17±0.36 |
| 1206.9 | 3636 ±12 | 0.18±0.34 |
| 1247.1 | 3636 ±11 | 0.18±0.31 |
| 1299.8 | 3641.0±6.1 | 0.04±0.18 |
| 1349.4 | 3640.8±6.0 | 0.05±0.18 |
| 1399.1 | 3638.1±4.8 | 0.12±0.15 |
| 1463.9 | 3650.9±4.4 | -0.23±0.14 |
| 2096.8 | 3633.8±1.6 | 0.24±0.09 |
| 2112.8 | 3649.0±1.4 | -0.18±0.08 |

In order to interpret the total losses from dead-time and random-summing effects, for 511-keV events, the $R_o/R_T$ ratios in table 5-3 were modelled to a parabolic relationship with both the observed 511-511-keV coincidence rates and the appropriate observed singles rates listed in table 5-2 since at least one or other of the two types of rates was available in all experiments. The resulting equations can be written as

$$R_o/R_T = 1.00 - 0.000118\ R_c - 0.0000002\ R_c^2 \qquad (5.26)$$

and

$$R_o/R_T = 1.00 - 0.00242\ R_s - 0.000034\ R_s^2 \qquad (5.27)$$

where $R_c$ is the observed rate for full-energy coincidences in thousands of counts per minute and $R_s$ the observed singles rate for detection of events of all energies, in thousands of counts per second. The correction divisors, $R_o/R_T$, obtained from equations (5.26) and (5.27) were good to better than five parts in a thousand. The above equations therefore formed the basis for all corrections although their application to individual experiments required specific interpretation.

By far the most important intent of the $^{18}F$ experiment was to obtain a reliable estimate of the stop efficiency. Relevant data extracted from the appropriate spectra accumulated in MPA-SS mode are listed in table 5-5. The data shown were analysed in accordance with the development presented in equations (3.6) through (3.10). The solid angle subtended by one quadrant of the NaI(Tl) annulus was calculated from geometry considerations to

## TABLE 5-5 DATA FOR EFFICIENCY CALCULATION

| Mean Time (minutes) | Number of Events in Pulser Peak | | | Number of Events in Full-Energy Peak | | |
|---|---|---|---|---|---|---|
| | x-axis | y-axis | Coincidence | x-axis | y-axis | Coincidence |
| 1412.1 | 2065 | 1931 | 14032 | 129135±525 | 140714±488 | 484932±1064 |
| 1475.8 | 2084 | 2000 | 14137 | 87923±444 | 97231±441 | 325351± 854 |

be 0.872 π steradians. Thus a fractional solid angle of 0.218 was used for Ω in equation (3.10). The resulting stop efficiencies, calculated from the two sets of data, were 0.1143±0.0007 and 0.1126±0.0009 respectively. However, the error (< 1%) attached to each result is not realistic since no error has been assigned to the number of pulser events, and since solid angle and intrinsic efficiency are not truly separable. If one takes the other extreme by assigning counting statistics to the pulser peaks, the efficiencies become 0.114±0.004 and 0.113±0.004 respectively. Furthermore, since the backgrounds in the spectra analysed were not truly known, but were simply modelled as polynomials, it is hard to justify the accuracy (< 0.5%) listed for the number of events in the full-energy peaks. It was therefore decided that 0.114±0.003 would be a more realistic evaluation of the stop efficiency.

However, it must be kept in mind that the above evaluation was specifically for a point source of annihilation radiation. Since, in the investigation of fourfold coincidences, the targets actually extended over approximately 5 cm of length, the proper stop efficiency could be expected to be slightly lower than reported above, from solid angle considerations. A quantitative estimate of the loss of efficiency was experimentally obtained by measuring the twofold coincidence rates for annihilation quanta from a 1-cm-diameter disc source of $^{22}$Na placed in several axial positions within the NaI(Tl) annulus. The acquired data are presented graphically in figure 5-11. The solid curve shown is a result

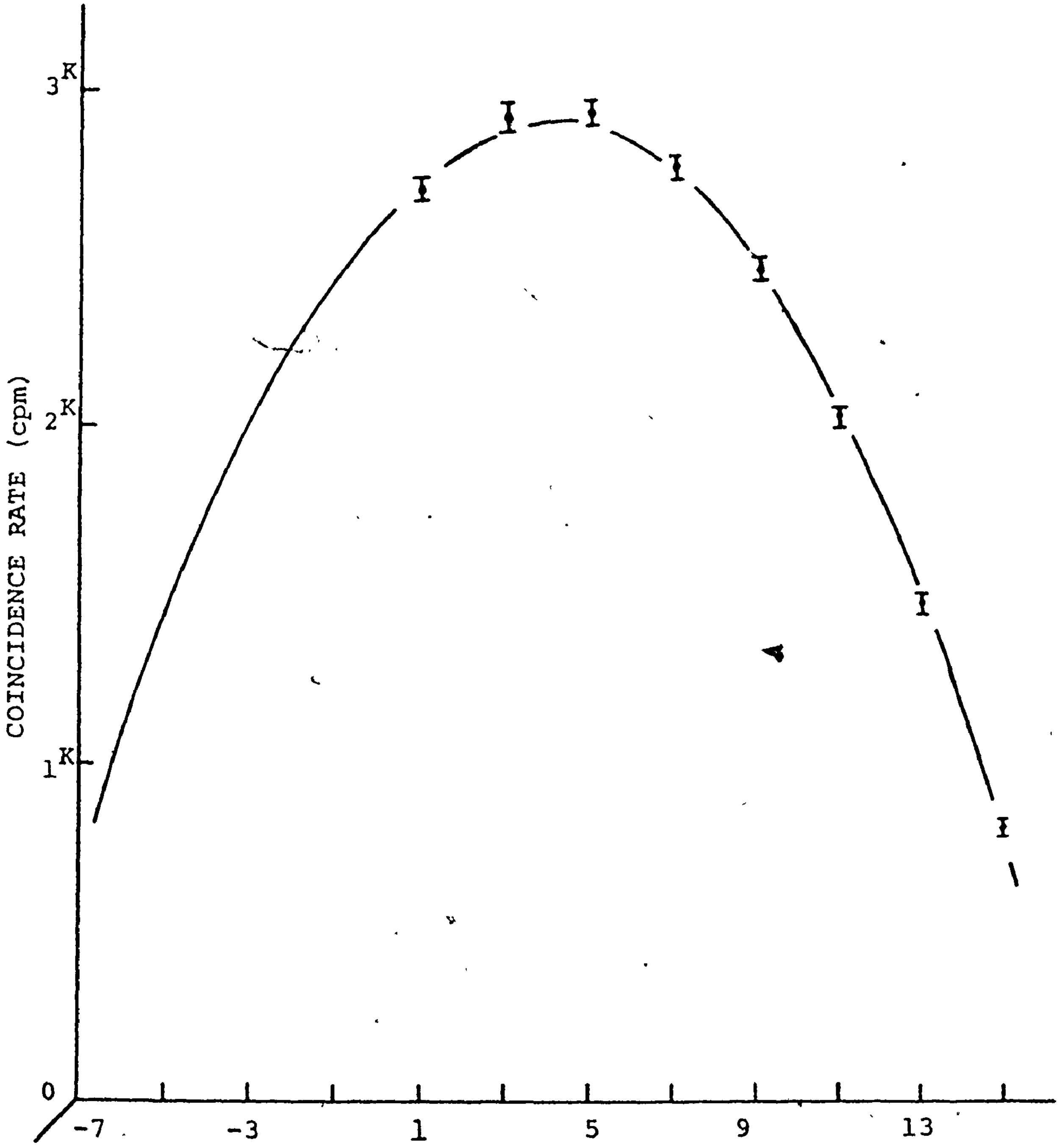

FIG. 5-11 VARIATION IN TWOFOLD COINCIDENCE RATE WITH POSITION ON AXIS OF ANNULUS

of modelling the relationship between rate and position to a parabola. The least-squares solution can be written as

$$R = 2610.9 + 149.18X - 17.992X^2 , \qquad (5.28)$$

where R and X represent rate and position respectively. It should be noted that the positions are recorded as the number of quarter inches from an arbitrary reference position. Although the source holder, which was similar to that shown in figure 3-5, did not permit measurements to be made throughout the full length of the annulus, a basic symmetry of rates about the central position could safely be assumed. Indication of the loss in efficiency associated with each target was obtained by comparing the maximum count rate of 2920 counts per minute predicted by the parabolic model with the average rate obtained by using equation (5.28) and the limits of position defined by the ends of each target. Since the density of annihilation centres along the length of most targets varied quite linearly with distance from the front face of the target, losses in efficiency could be typified for 4.5-cm and 5-cm targets by using an unweighted average. The respective decrements in efficiency were found to be 2.5% and 3.3%. Although these percentages are representative of the dimunitions experienced for most targets, more precise calculations could be made to take into account exact target lengths, and averages could be weighted in terms of the exponential distribution of annihilation centres with axial distance along each target. In addition, the effect of displacing a target along the axis of the annulus was determined by integrating equation (5.28) over positions defined by the extent of the target when displaced. For a 4.5-cm target displacements of 0.25 and 0.5 inches caused decreases in efficiency of 0.63% and 2.52% respectively. The corresponding values for a 5-cm target were calculated as 0.45% and 2.18%. However the important points to be extracted from the above discussion are that deviations of individual target efficiencies from that measured for a centrally located point source are both small and easily calculable. Moreover, the even smaller deviations stemming from off-axis centres of annihilation have been largely incorporated into the data through use of a $^{22}$Na source whose diameter was approximately the same size as the diameter of the beam of collimated gamma rays.

## 5.4 INVESTIGATION OF FOURFOLD COINCIDENCES

It should be recalled that three-parameter data (time-energy-energy) were "address-recorded" in this experiment to permit elimination of chance coincidence events and an expected large background component from bremsstrahlung events. The data for each target were analysed by firstly collecting together all events with the same "addresses" in time. The resultant spectrum invariably had a form similar to the time spectrum shown in figure 3-6, with the abscissa expressed in terms of address number or channel number. It is fairly obvious from figure 3-6 that such a spectrum permitted easy identification of both chance and true events. Consequently, in the computer code used for analysis of the data, appropriate "address"-windows were set to enable separation of events into those which would fall within the limits of the large peak of true coincidences in the "time" spectrum and those which would definitely correspond to chance coincidences. By this means it was possible to allocate an event to either a chance "energy-energy" spectrum or a true "energy-energy" spectrum. The true spectrum corresponding to a target of copper filings was previously presented in figure 3-7. However the large annihilation peak seen in figure 3-7 is not representative of the size of the peak to be seen for other targets. Most of the content of the annihilation peak in the case of the target of copper filings is derived from bremsstrahlung-cascade events. The probability for such cascade events increases approximately with the square of the atomic number of the target. By comparison, a target of carbon, with atomic number of 6 as opposed to Z=29 for copper, provides the true spectrum shown in figure 5-12. In this figure the axis units of channels were obtained by selection of the six most significant bits of the 12-bit address words associated with the "energy-energy" dimensions.

The next step in the analysis was predicated on the realization that the true "energy-energy" spectrum really contained a small number of chance coincidences since any window set around the peak of true time-correlated events, typified in figure 3-6, would necessarily include background events arising from accidental coincidences. Since the spectrum of chance events could be seen to be flat in time, from figure 3-6, it was a simple matter to subtract an appropriate fraction of the chance

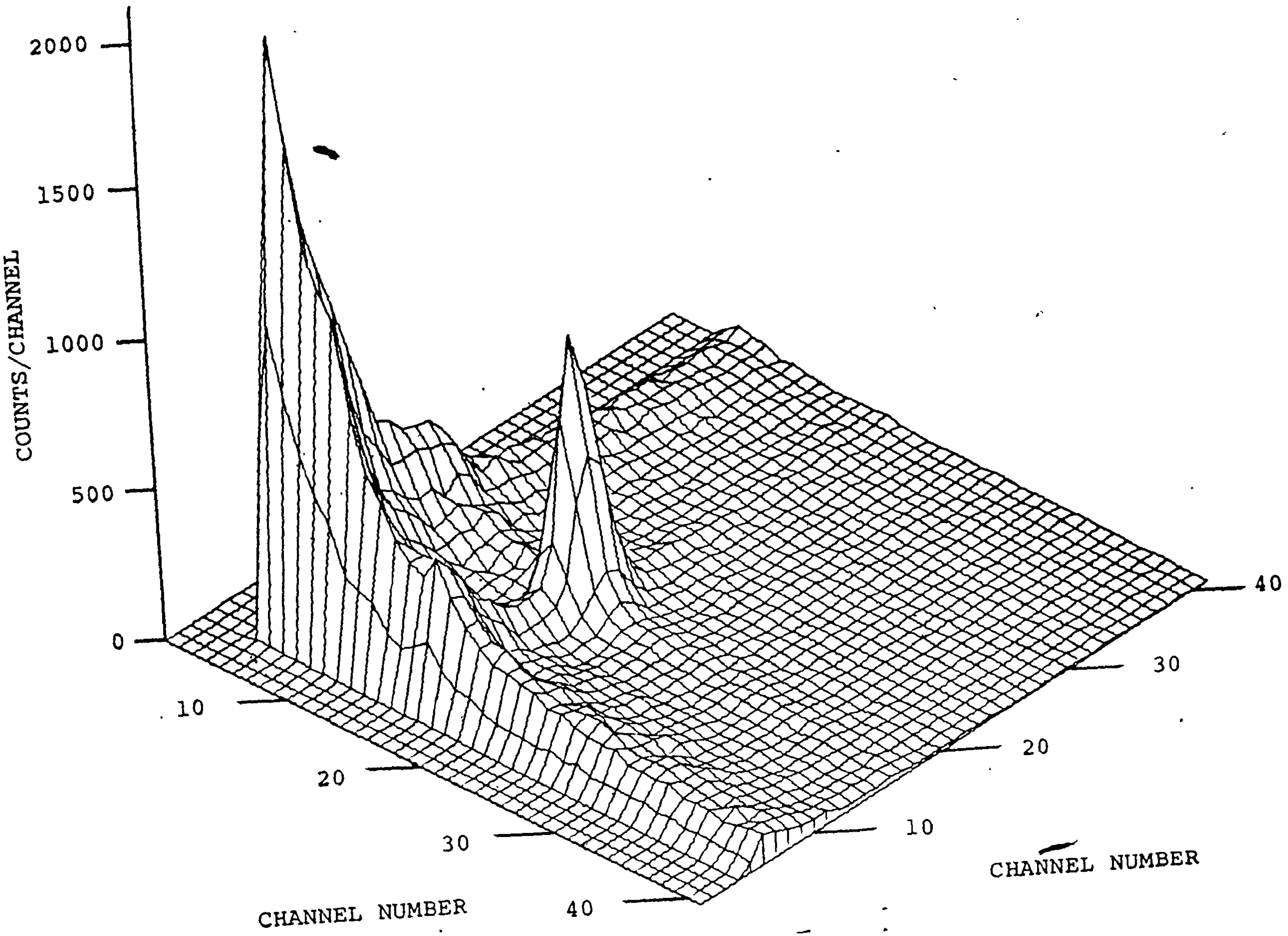

FIG. 5-12 FOURFOLD COINCIDENCE SPECTRUM FROM CARBON TARGET

"energy-energy" spectrum from the "energy-energy" spectrum labelled as true up to this point. The appropriate fraction was calculated in terms of the widths of the "address"-windows used for selection of chance and true events.

The residual spectrum, devoid of chance contributions, could then be correctly designated as the spectrum of true events. In a fashion identical to the stripping procedure outlined in section 5.3, the large two-dimensional background in the neighbourhood of the annihilation peak was then removed by modelling it to a polynomial in the one dimension followed by a similar modelling of the background remaining in the other dimension. The spectrum obtained for the carbon target, subsequent to subtraction of background in the first dimension, is shown in figure 5-13 by way of example. By the above procedure, the content of the full-energy peak of true stop-side coincidences was determined for each of the targets in table 3-1. In addition, data collected for the empty sample container as target were analysed to provide the small correction term of 9±4 events per 100 MW-hr. Results were also corrected for dead-time and random-summing effects. The ratio, $R_4$, of the number of full-energy fourfold coincidences to the number of true TAC-start events was calculated for each target, as required for equation (3.4). The corrected ratios are listed in table 5-6.

Before the analysis of the data could be extrapolated further it was necessary to calculate the self-absorption factor, $F_s$, for annihilation quanta in each target. The basic geometry

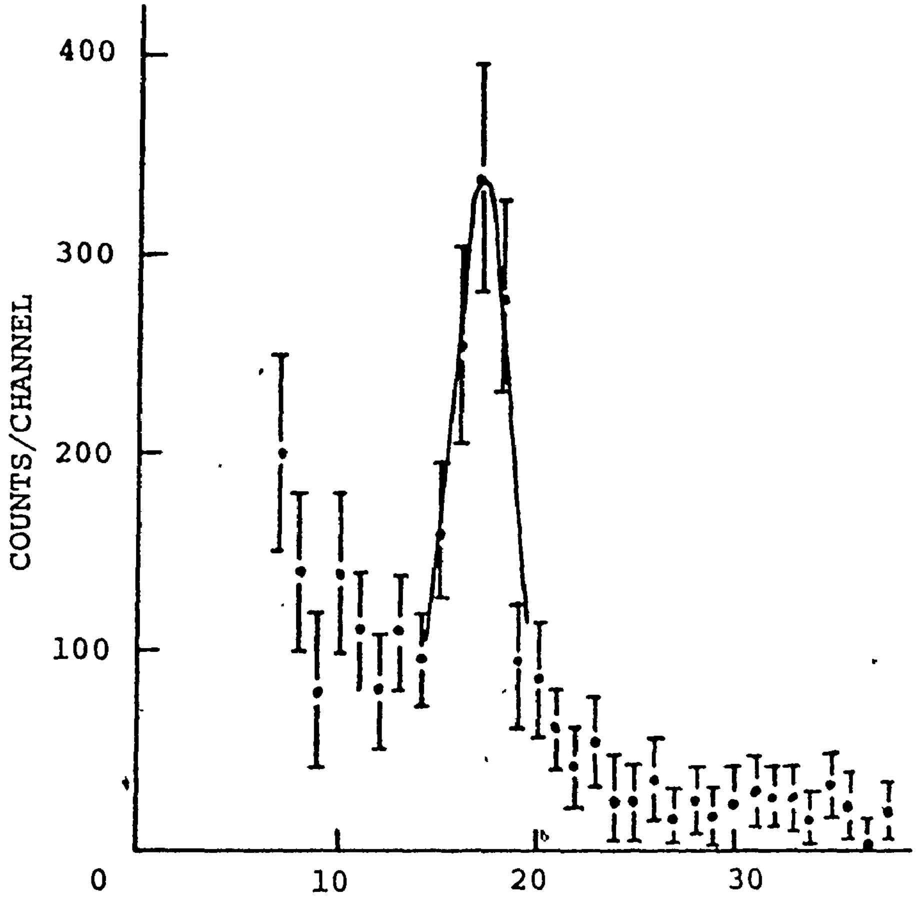

FIG. 5-13 FOURFOLD COINCIDENCE SPECTRUM FOR CARBON TARGET, AFTER STRIPPING IN ONE DIRECTION

TABLE 5-6 RATIOS OF FOURFOLD COINCIDENCES TO START EVENTS

| TARGET | COINCIDENCES/START ($R_4 \times 10^6$) |
|---|---|
| Be | 3.04±0.67 |
| B | 3.78±0.67 |
| C | 4.62±0.62 |
| Al | 14.05±0.74 |
| S | 17.01±0.98 |
| Cu-F* | 53.1 ±1.0 |
| Cu-S* | 37.10±0.90 |

*Cu-F refers to a target composed of copper filings whereas Cu-S refers to a solid target of copper.

involved in the calculation is shown in figure 5-14. The target was envisaged as divided into small cells of volume $rd\phi drdz$ and a uniform distribution of annihilation centres was assumed initially throughout the target but within the 0.5-cm radius of the incident beam. A solid angle of $\sin\theta d\theta d\phi'$ was assigned to describe the intensity of annihilation quanta emanating from a particular cell in a direction specified by $\theta$ and $\phi'$. Path lengths within the target and the NaI(Tl) annulus, for the two correlated 511-keV quanta from each annihilation, were expressed in terms of $r$, $\phi$, $z$, $\theta$ and $\phi'$. Since the cross sections involved were well known, it was then possible to calculate the average of the product of self-absorption and efficiency, I, by evaluating the expression

$$I = \int\!\!\int\!\!\int\!\!\int\!\!\int Drd\phi drdz e^{-\mu_s L_s} p^2 (1-e^{-\mu L_1})(1-e^{-\mu L_2}) \sin\theta d\theta d\phi' \qquad (5.29)$$

over the appropriate limits of integration. Here D is the distribution of annihilation centres and $e^{-\mu_s L_s}$ is the total transmission factor for escape of two annihilation quanta from the sample. The expressions in brackets are the respective interaction factors for correlated annihilation quanta in opposite NaI(Tl) quadrants, and p is the photo-fraction for 511-keV photons, deduced from the data of the $^{18}F$ experiment to be 0.63. The fivefold integral in equation (5.29) was actually evaluated by numerical quadrature. Probably the most difficult part of the calculation was in obtaining the many limits of integration and the various path lengths involved since they were conditioned by

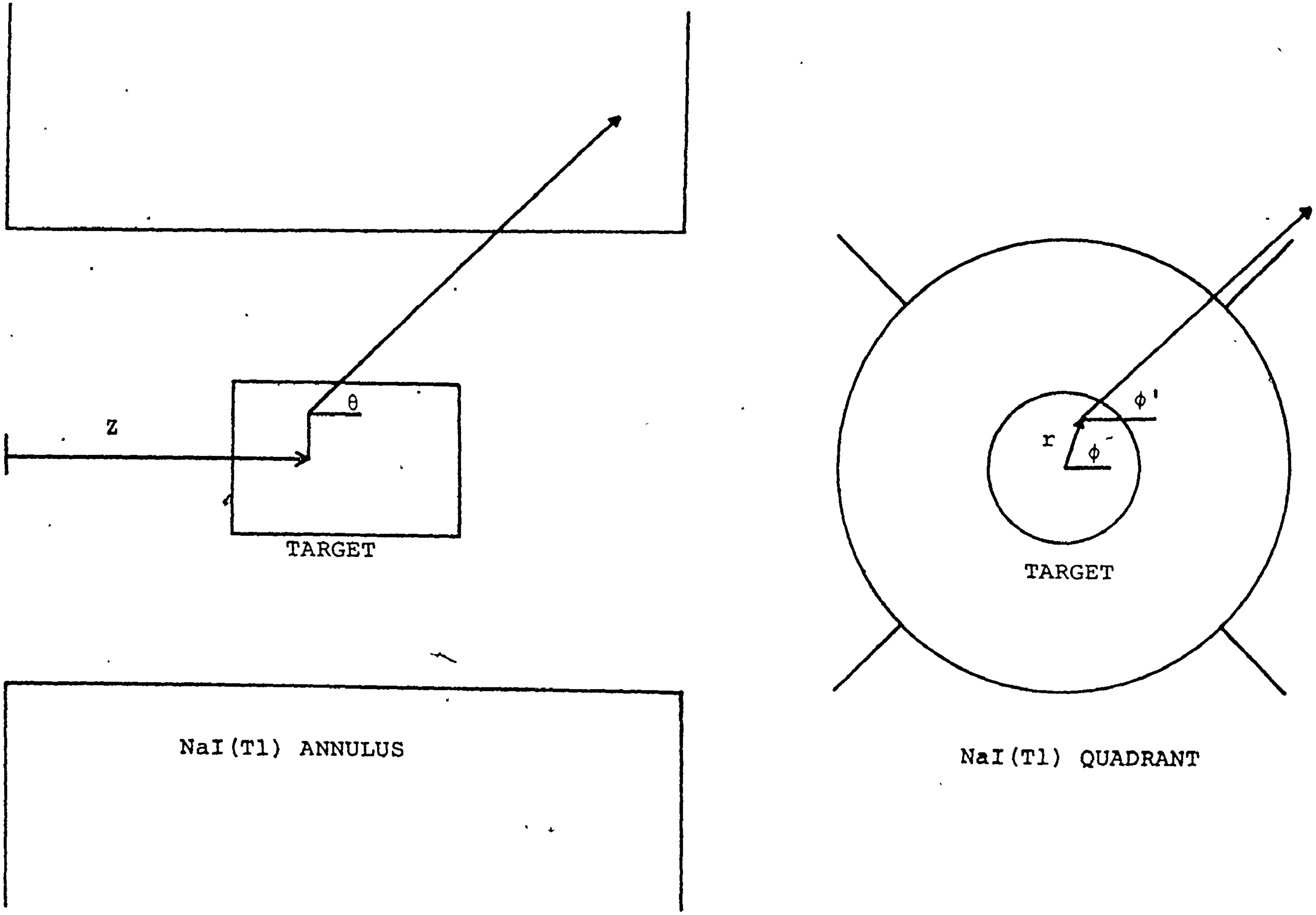

FIG. 5-14 GEOMETRY FOR CALCULATION OF SELF-ABSORPTION AND EFFICIENCY

sample and annulus geometries which required consideration of edge effects. They were also conditioned by the correlation of the two annihilation quanta which constrained the solid angles possible for coincident detection. Several other summations were conducted concurrently with the aforementioned fivefold summation. The evaluation of equation (5.29) was normalized by dividing the summation of the source distribution over volume and solid angle. Since it was realized that quantities such as self-absorption and detector efficiency were not truly separable, the self-absorption factor for a target was treated as that seen by the detector. Consequently it was obtained as the ratio of the above summation to a summation in which the target was seen as transparent to 511-keV quanta. An estimate of the efficiency could then be obtained by dividing the average of the product of efficiency and self-absorption by the average self-absorption.

As a check of the sensitivity of the results to the initially assumed uniform distribution of annihilation centres, the self-absorption factors for the carbon and solid copper targets were calculated for distributions varying between that of a line source and that of a fully illuminated target. Results are shown graphically in figure 5-15. It is clear from the figure that the self-absorption factor for carbon varies very little across the whole range of radii and that the factor for copper shows large deviations from the value at zero radius only when unrealistically large radii are considered. In fact, in the

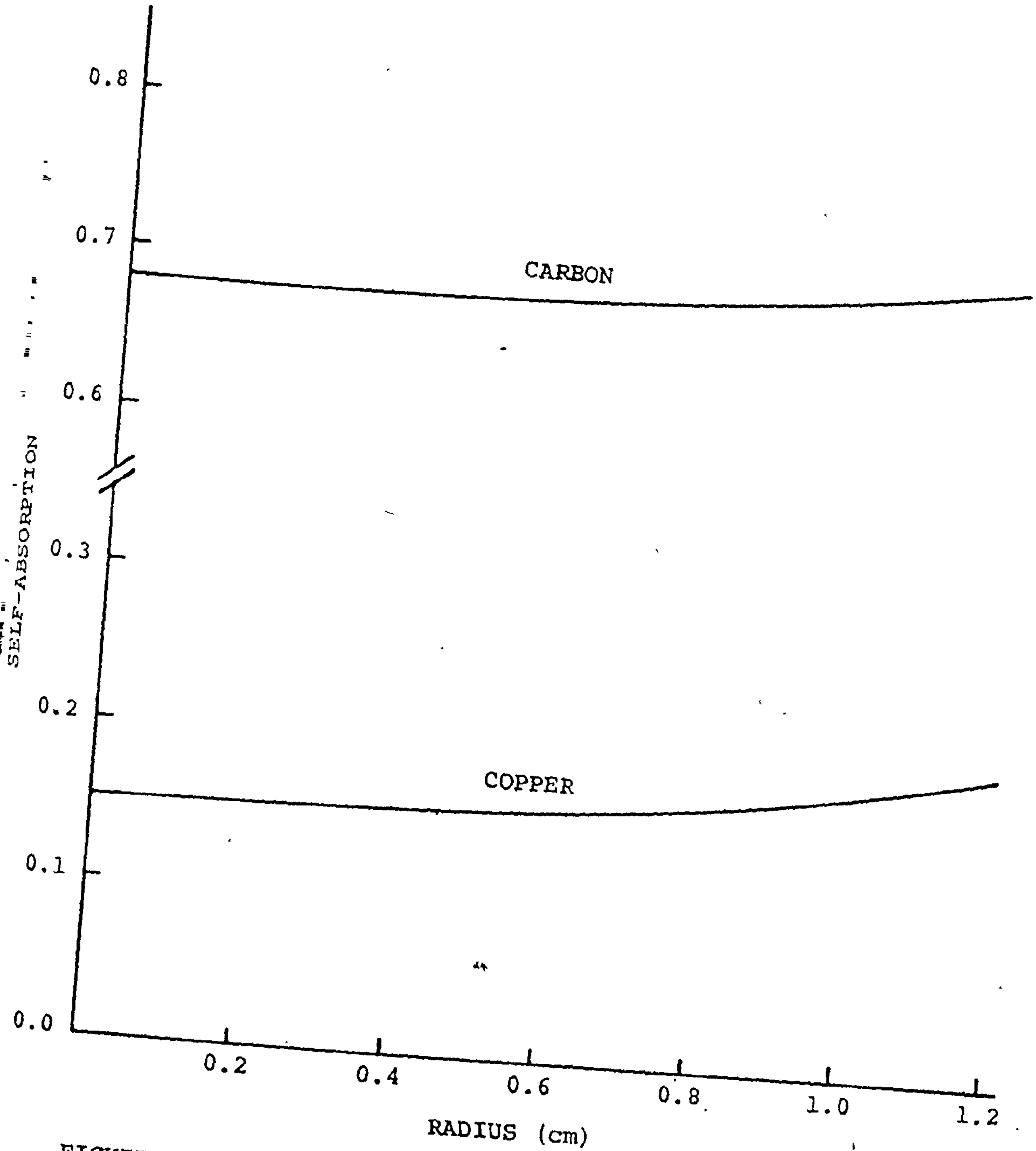

FIGURE 5-15 VARIATION OF DOUBLE-ESCAPE SELF-ABSORPTION FACTOR WITH RADIUS OF UNIFORM DISTRIBUTION OF ANNIHILATION CENTRES

neighbourhood of the 0.5-cm radius associated with the collimated beam of gamma rays very little variation in the self-absorption factor is evident for either target. This is ascribable to the self-absorption factor being concerned with the escape of both of the correlated annihilation quanta. Not only are possible solid angles therefore somewhat restricted but also, since the two annihilation quanta are oppositely directed, a given path of escape gives rise to the same total transmission factor for all possible locations of annihilation centres along that path.

However, although the uniform distribution of annihilation centres provided self-absorptions that were remarkably insensitive to the radius used it was decided to employ a more realistic distribution. In the radial direction, the areal density of annihilation centres was assumed to fall off as for a Gaussian distribution centred about the target axis, to take into account the diffusion of positrons previous to annihilation. The variance of the Gaussian distribution was taken to be the sum of the variance of the uniform distribution terminated at the beam radius and the variance of a spreading-function. The latter variance was assumed, from the angular distribution theory of Bethe, discussed on page 35 of this thesis, to be given by the square of the product of the average positron range and $\sin(2m_oc^2/\sqrt{3}\hbar\omega)$. In the axial or z direction the linear density of formation of positrons was known to decrease exponentially. However, the general tendency of energetic positrons to drift in the forward direction before annihilating had to be incorporated into the distribution. Convolution involving the exponential distribution of formation, an assumed rectangular distribution of positron energies (figure 2-3), and positron ranges proportional to positron energies (equation (2.83)), led to the description of the distribution of annihilation centres in the z direction as

$$D(Z) = 1 - e^{-\mu_6 Z} \qquad (5.30)$$

for Z less than or equal to the maximum positron range $R_m$, and

$$D(Z) = e^{-\mu_6 Z}(e^{\mu_6 R_m}-1) \qquad (5.31)$$

for $Z>R_m$. In these equations $\mu_6$ is the linear coefficient of absorption of 6.6-MeV photons by the particular target involved. Equations (5.30) and (5.31) appear sensible since they indicate a distribution which increases with Z to a maximum at $Z = R_m$ and then decreases exponentially thereafter. Moreover, for materials with a small maximum range for the positrons, that is with good stopping power, the maximum of the distribution is located very close to the front face of the target.

The above calculation of self-absorption and efficiency was improved even further by the valid introduction of two additional factors. Firstly, the attenuation of annihilation quanta in materials located between the target and the NaI(Tl) detector was taken into account. Such materials included the sample container, the sample holder and the inner aluminum wall of the annulus. Secondly, a first-order correction was made for

511-keV gamma rays which were Compton scattered within the target but still contributed to the full-energy peak. The need for such a correction is evident from figure 2-5 where the distribution of Compton electrons scattered by 0.511-MeV gamma rays is seen to peak sharply at zero energy of recoil. The complementary distribution for Compton-scattered photons therefore peaks sharply at a photon energy of 511 keV. Correction was achieved via considerations involving convolution of the distribution of Compton-scattered photons with spectral lineshapes simply modelled in terms of photo-fraction and detector resolution.

As a check of the model and the computer code, the efficiency for a centrally located point source of annihilation radiation was calculated. The calculated efficiency of 0.117 compared favourably with the measured value of 0.114 within the experimentally assigned error of 0.003. One could have expected the calculated value to be slightly higher than the measured value since it was possible in the calculation to achieve a source which represented a point geometry better than did the $^{18}F$ source used experimentally. Furthermore, small errors in cross section and photofraction of the NaI(Tl) detector, as well as an error attributable to numerical quadrature, could lead to an error in the calculated efficiency. In the calculations to follow, efficiencies were therefore normalized in terms of the measured point-source efficiency of 0.114.

Efficiencies, self-absorption factors, and average values of the product of efficiency and self-absorption factors were calculated, in accordance with the above discussion, for all targets used in the investigation of fourfold coincidences. The results are listed in table 5-7. The efficiency results give further credence to the correctness of the calculations since they are lower than the point-source efficiency of 0.114 by amounts which agree with those predicted experimentally in section 5.3. Also, calculations are further validated in figure 5-16 where the calculated self-absorption factors for the various targets are compared with results calculated analytically for a line source axially imbedded in an infinitely long cylinder and those extracted from work reported by Case et al[96)] for a uniformly illuminated infinite cylinder. As expected, the results calculated for the targets used in the fourfold coincidence experiment lie within the bounds provided by the two extreme models just mentioned.

The experimentally determined fourfold coincidence ratios, corrected for efficiency and self-absorption, are listed in table 5-8.

## 5.5 INVESTIGATION OF TWOFOLD COINCIDENCES

Three-parameter (time-energy-energy) data were acquired in this experiment for each of the targets used in the fourfold coincidence investigation. Chance contributions were eliminated

TABLE 5-7 CALCULATED SELF-ABSORPTION AND EFFICIENCY FACTORS

| Target | <Efficiency×Self-Absorption> $\varepsilon_2 F_s$ | $\langle F_s \rangle$ | Efficiency $\varepsilon_2$ (±0.003) |
|---|---|---|---|
| Be | 0.0751 | 0.676 | 0.111 |
| B | 0.0917 | 0.822 | 0.112 |
| C | 0.0757 | 0.679 | 0.112 |
| Al | 0.0600 | 0.549 | 0.109 |
| S | 0.0817 | 0.737 | 0.111 |
| Cu-F | 0.0579 | 0.524 | 0.111 |
| Cu-S | 0.0169 | 0.153 | 0.111 |

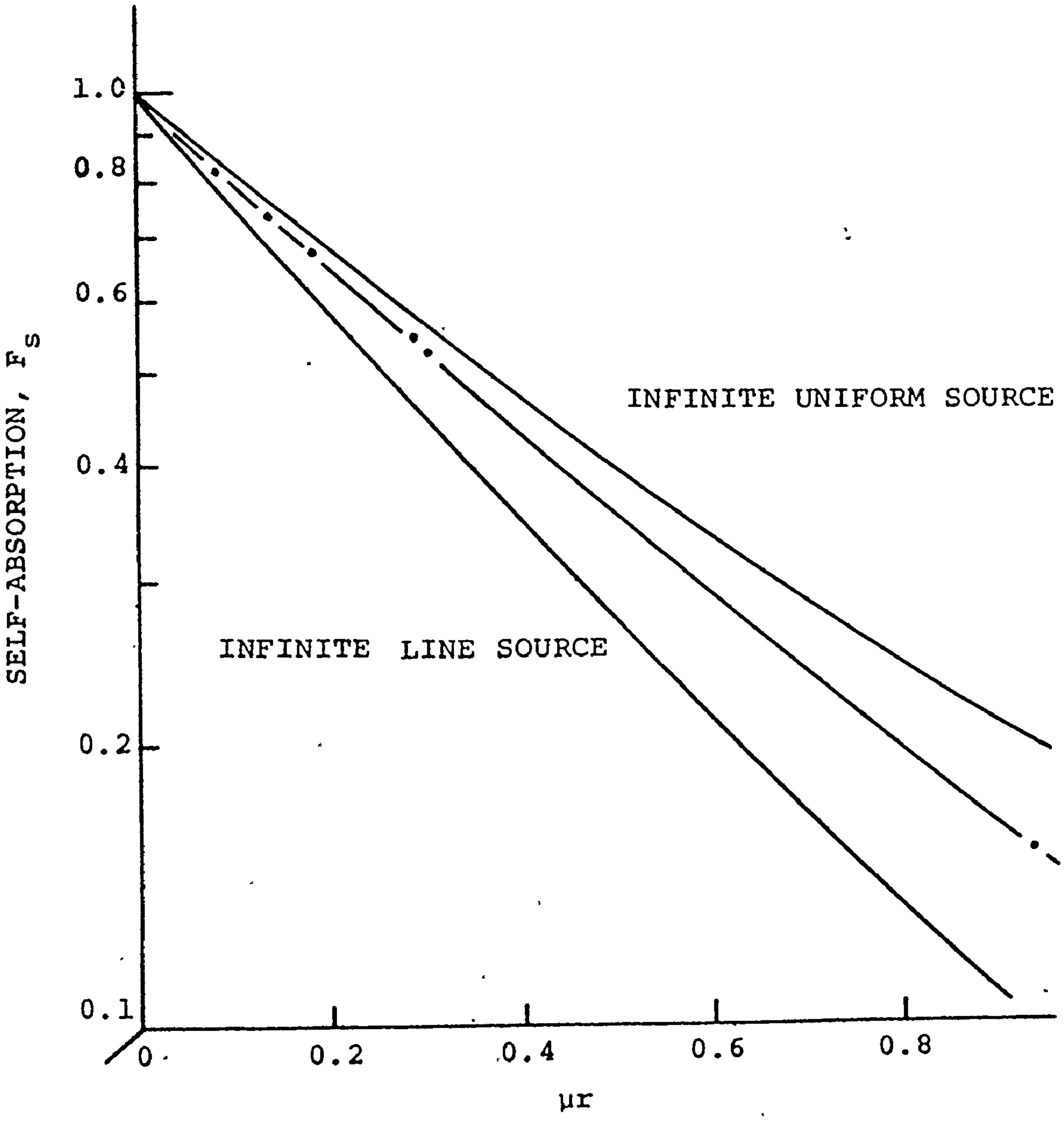

FIG. 5-16 SELF-ABSORPTION FACTORS FOR ESCAPE OF BOTH ANNIHILATION QUANTA. Data are plotted against the product of linear attenuation coefficient and target radius.

TABLE 5-8 FOURFOLD RATIOS CORRECTED FOR EFFICIENCY AND SELF-ABSORPTION

| TARGET | $(R_4/\varepsilon_2 F_s)\times10^5$ |
|---|---|
| Be | 4.05±0.90 |
| B | 4.12±0.74 |
| C | 6.11±0.84 |
| Al | 23.4 ±1.4 |
| S | 20.8 ±1.4 |
| Cu-F | 91.6 ±3.3 |
| Cu-S | 219.5 ±8.5 |

through an analysis procedure identical to that discussed in the previous section. The resultant "energy-energy" spectrum of true coincidence events, obtained by means of the carbon target, is shown in figure 5-17 by way of example. The features evident in this spectrum are clearly similar to those seen in figure 5-8, and explained at length in section 5.3. Once again the contents of the full-energy coincidence peaks were extracted by polynomial fitting of the two-dimensional background. The rates of full-energy coincidences for the various targets are presented in table 5-9 where they are corrected for dead time, random summing and the interaction probability for pair production. The latter correction stems from equation (3.2) since the intent of the experiment is to isolate the respective containment factors, $f_s$. For the same reason, each rate must also be divided by the respective absolute flux of 6.6-MeV gamma rays, stop efficiency, and self-absorption factor.

Throughout the twofold coincidence investigation three concrete absorbers were stationed in the collimated beam of gamma rays. It was therefore necessary to relate the measured absolute flux for a condition of no absorbers in the beam to that for three. Since the part of the experiment involving the sulphur target was repeated immediately with no attenuators in the beam, it was reasoned, through equation (3.2), that the only quantity altered was indeed the flux of 6.6-MeV gamma rays. Subsequent analysis of the full-energy coincidence rates for the two measurements revealed the attenuation ratio in going from

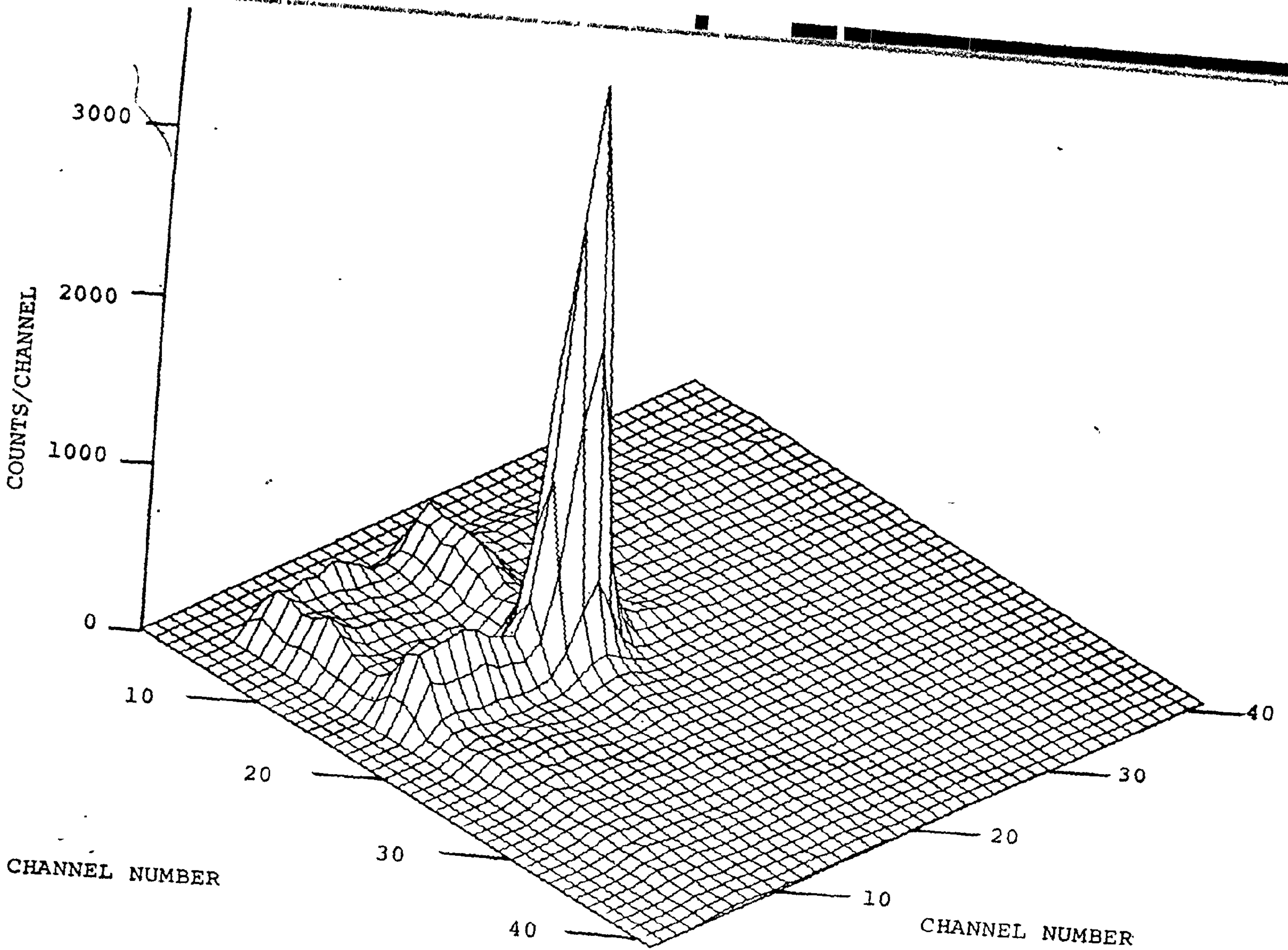

FIG. 5-17 TWOFOLD COINCIDENCE SPECTRUM FROM CARBON TARGET

TABLE 5-9 TWOFOLD COINCIDENCE RATES FOR FULL-ENERGY EVENTS

| Target | Rates Corrected for Dead-Time and Random Summing Effects, $N_2$ (cps) | Interaction Probability $\frac{\sigma_\pi}{\sigma}$ $[1-e^{-n\sigma}]$ | $N_2/\frac{\sigma_\pi}{\sigma}$ $[1-e^{-n\sigma}]$ ($10^3$ cps) |
|---|---|---|---|
| Be | 95.6±0.7 | 0.0133 | 7.20±0.05 |
| B | 58.6±0.5 | 0.0088 | 6.63±0.06 |
| C | 125.7±0.9 | 0.0192 | 6.56±0.05 |
| Al | 317 ±2 | 0.0600 | 5.28±0.03 |
| S | 81.6±0.6 | 0.0427 | 1.91±0.01 |
| Cu-F | 624 ±5 | 0.140 | 4.45±0.04 |
| Cu-S | 520 ±5 | 0.278 | 1.87±0.02 |

no absorbers to three absorbers to be 5.16±0.05. Consequently by analogy with equations (4.18) and (5.19), and through use of equation (5.22), the appropriate relationship between gamma-ray flux and monitor rate was established as

$$\phi_\gamma(3) = \left(\frac{1.04\pm0.06}{5}\right)[0.01R-0.272]\times10^5 \qquad (5.32)$$

gamma rays per second. Coincidence rates were therefore normalized to unit flux by means of equation (5.32) and the recorded monitor rates.

The possibility of some gamma rays having sufficient energy, following Compton scattering, to create a positron-electron pair was also considered. The probability of such an eventuality was calculated via a simple model in which the incident 6.6-MeV gamma rays were seen to travel along the axis of a cylindrical target. Only those gamma rays which scattered into an angle less than ∿ 40° were considered since for greater angles the energy of the scattered photon was less than $2m_oc^2$. The possibility of escape of the positrons created by scattered radiation was disregarded since multiple interactions could only be significant in targets of high density. Essentially, the Compton effect varies directly with density whereas the range of positrons in a material varies inversely with density. Moreover, the average energy of positrons created by scattered radiation must be lower than that for positrons created directly by 6.6-MeV gamma rays. The probability of a Compton scattering resulting in the production of a positron-electron pair was therefore calculated relative to normal pair production as

$$P_m = \frac{\int_\Omega \int_{Z=0}^{L} e^{-\mu z} dz \left(\frac{d\sigma}{d\Omega}\right)_\theta d\Omega_\theta \frac{\sigma_\pi(\theta)}{\sigma(\theta)} \left(1-e^{-\mu(\theta)\ell(\theta)}\right)}{\int_{Z=0}^{L} e^{-\mu z} \sigma_\pi dZ} . \qquad (5.33)$$

Here $\mu$ is the linear coefficient of absorption for 6.6-MeV gamma rays, Z is the distance from the front face of the target of length L at which the primary interaction occurs, and $\sigma_\pi$ is the pair production cross section for 6.6-MeV photons. The differential Compton cross section for scattering of an incident gamma ray into a solid angle $d\Omega_\theta$ at an angle $\theta$ is represented by $(d\sigma/d\Omega)_\theta$, and, for the scattered photon, the pair production cross section, the total cross section, the linear absorption coefficient and the path length are given as $\sigma_\pi(\theta)$, $\sigma(\theta)$, $\mu(\theta)$ and $\ell(\theta)$ respectively. The maximum correction provided by equation (5.33) was approximately 7% for the solid copper target.

The containment probabilities, $f_s$, for the various targets are presented in table 5-10 where results have been further corrected for gamma flux, multiple interactions, stop efficiency and self-absorption. It is heartening to note that the containment factor for the solid copper target is 0.99 as this suggests that the absolute flux measurement and the various correction factors have been accurately applied since one would expect a value very close to 1.0 for such a dense (8.96 gm/cm$^2$) sample.

TABLE 5-10 CONTAINMENT PROBABILITIES, $f_s$, VIA CORRECTION OF TWOFOLD COINCIDENCE RATES

| Target | Rate Corrected Gamma Flux | Rate Corrected for Multiple Events | Rate Corrected for Efficiency and Self-Absorption, Giving Containment Probability |
|---|---|---|---|
| Be | 0.069±0.004 | 0.068±0.004 | 0.91±0.06 |
| B | 0.064±0.004 | 0.063±0.004 | 0.69±0.05 |
| C | 0.063±0.004 | 0.062±0.004 | 0.82±0.06 |
| Al | 0.051±0.003 | 0.050±0.003 | 0.83±0.05 |
| S | 0.061±0.004 | 0.060±0.004 | 0.74±0.05 |
| Cu-F | 0.043±0.003 | 0.042±0.003 | 0.73±0.06 |
| Cu-S | 0.018±0.001 | 0.0168±0.0009 | 0.99±0.07 |

Although the containment factors for the other targets are fairly high, and therefore supportive of general expectations, they are not sufficiently large to permit immediate dismissal of the effect of all containment factors found in equation (3.4). The ratio, $f_d/f_s$, of containment probabilities for double pair production and single pair production, found in equation (3.4), is of primary importance. Consider the following model for the case of single pair production. If one assumes a uniform distribution of pair productions throughout the sample, and a propogation of positrons in the forward direction, one can write the fraction of positrons of a particular energy that are stopped within the target as

$$f_s(E) = 1 - \frac{R(E)}{L} \qquad (5.34)$$

where L represents the total length of the target and R(E) the range associated with the positrons of energy E. The ratio R(E)/L in equation (5.34) is based on the assumption that only those positrons which experience a path length less than one range escape from the target. The fact that in reality some positrons escape through the sides of a target is counterbalanced in part by the assumption of a uniform distribution of creation centres throughout the length of the target. Since the centres are really exponentially, or practically linearly, distributed along the target, fewer positrons than predicted by the model should escape in the forward direction. The average containment probability for all possible ranges can be expressed from equation (5.34) as

$$\langle f_s \rangle = \int_0^{R_m} (1 - \frac{R}{L}) P(R) dR \ . \tag{5.35}$$

Here $R_m$ signifies the maximum positron range and P(R) stands for the probability of obtaining the general range R. Since positron energies are fairly uniformly distributed and since a positron's range is effectively directly proportional to its energy, one can assume a uniform distribution of positron ranges. Equation (5.35) then becomes

$$\langle f_s \rangle = \int_0^{R_m} (1 - \frac{R}{L}) \frac{dR}{R_m} \tag{5.36}$$

$$= 1 - \frac{R_m}{2L} \ . \tag{5.37}$$

The calculated values of the containment factors for positrons created in single-pair productions are listed in the third column of table 5-11. They compare favourably with the measured values when the errors listed for the latter are considered. The anomolously low value measured for the non-solid copper target can perhaps be attributed to the use of filings instead of a fine-mesh powder.

Calculation of containment probabilities for positrons created in double-pair productions is made difficult by the lack of knowledge of how the total energy should be distributed amongst the four particles created. If one accepts the faute mieux assumptions of Wilkinson and Alburger$^{20)}$ that the energy

TABLE 5-11 COMPARISON OF CONTAINMENT PROBABILITIES

| Target | Measured $f_s$ | Calculated $f_s$ | Calculated $f_d$ | Calculated Ratio $f_d/f_s$ |
|---|---|---|---|---|
| Be | 0.91±0.06 | 0.827 | 0.863 | 1.044 |
| B | 0.69±0.05 | 0.653 | 0.732 | 1.121 |
| C | 0.82±0.06 | 0.805 | 0.847 | 1.051 |
| Al | 0.83±0.05 | 0.881 | 0.905 | 1.027 |
| S | 0.74±0.05 | 0.776 | 0.824 | 1.062 |
| Cu-F | 0.73±0.06 | 0.900 | 0.920 | 1.022 |
| Cu-S | 0.99±0.07 | 0.964 | 0.971 | 1.007 |

is randomly shared between created pairs, and that for each pair the Hough parameterization (equation (2.28)) applies, one can calculate the containment probabilities, $f_d$, associated with double pair production in a fashion similar to the above modelling. Consider that in sharing the total energy $E_o$, one pair receives an energy of $E_1$ while the other receives $E_o - E_1$. The probability of a positron from the first pair being contained can then be written, via equation (5.37), as

$$P_1 = 1 - \frac{R_1}{2L} , \tag{5.38}$$

where the range $R_1$ can be directly associated with the energy $E_1$. Similarly the containment probability for the positron in the second pair can be expressed as

$$P_2 = 1 - \frac{(R_o - R_1)}{2L} . \tag{5.39}$$

The probability of both being contained can then be written as

$$\langle f_d \rangle = \int_o^{R_o} [1 - \frac{R_1}{2L}] [1 - \frac{(R_o - R_1)}{2L}] P(R_1) dR_1 , \tag{5.40}$$

where the probability of getting a maximum range $R_1$ for the positron of the first pair, $P(R_1)$, can be assumed to be uniformly distributed between 0 and $R_o$ since the energy received by the first pair, $E_1$, is uniformly distributed between 0 and $E_o$. Equation (5.40) can therefore be integrated to give

$$\langle f_d \rangle = 1 - \frac{R_o}{2L} + \frac{1}{6} \left(\frac{R_o}{2L}\right)^2 . \tag{5.41}$$

Results calculated from equation (5.41) are listed in table 5-11 where the calculated ratios of $f_d/f_s$ are also shown. It can be seen that, but for the boron sample, all ratios are reasonably close to unity. The average 4.8% error introduced by an assumption of unity for $f_d/f_s$ can easily be accommodated, although it is systematic, by the much larger errors to be encountered later in the present work.

At this juncture one can also consider the containment probability ratios of $f_D/f_s$ and $f_a f_b/f_s$ found in equation (3.4) as corresponding to the direct-cascade and the bremsstrahlung-cascade effects respectively. As in the case of double pair production, the total energy available must be shared amongst the four created particles. However now the second pair produced can be spatially separated from the position of creation of the first pair. Although it is difficult to construct a very simple model for each of the cascade effects, one can make the general argument that since the energetics involved are practically identical to those found in double pair production, the ratio of containment probabilities must be similarly close to unity. In fact, since there is a spatial separation of the two pairs in the cascade effects one can envisage there being a slightly greater probability of positron escape compared to that for two pairs produced at effectively the same position. This would imply that the ratios of containment probabilities for the cascade effects were even closer to unity than those for double pair production. As such, they will be ignored in future considerations.

## 5.6 INVESTIGATION OF THREEFOLD COINCIDENCES

The data from this investigation were acquired in "time-energy" configurations of 128 by 128 channels. Chance events were eliminated by means of the time encodement which permitted data to be selectively analysed for truly time-correlated events. The subsequent spectra obtained for the various targets were characteristically similar. The spectra associated with the carbon and solid copper targets are presented in figure 5-18 to typify the range of spectral shapes. Clearly the spectra in figure 5-18 are very similar despite the great differences in atomic number and density for the two targets involved. If one ignores the broad peaks at high energies, the spectral shapes are typical of external bremsstrahlung spectra. The spectrum associated with the solid copper target however shows evidence of greater attenuation of photons than does that for the carbon target. The high-energy limit for each spectrum is approximately 5.6 MeV, as one would expect for 6.6-MeV gamma rays losing $2m_oc^2$ of energy to pair creation. Energy calibration of the bremsstrahlung spectra was achieved by means of the $^{22}$Na and $^{49}$Ca spectra shown in figure 5-19.

The broad peak found near the high-energy limit of each bremsstrahlung was intriguing since it was quite unexpected. A thorough check of equipment for possible malfunction firmly established the peak as representing a real phenomenon. In the spectra of all targets used, the peak extended from approximately

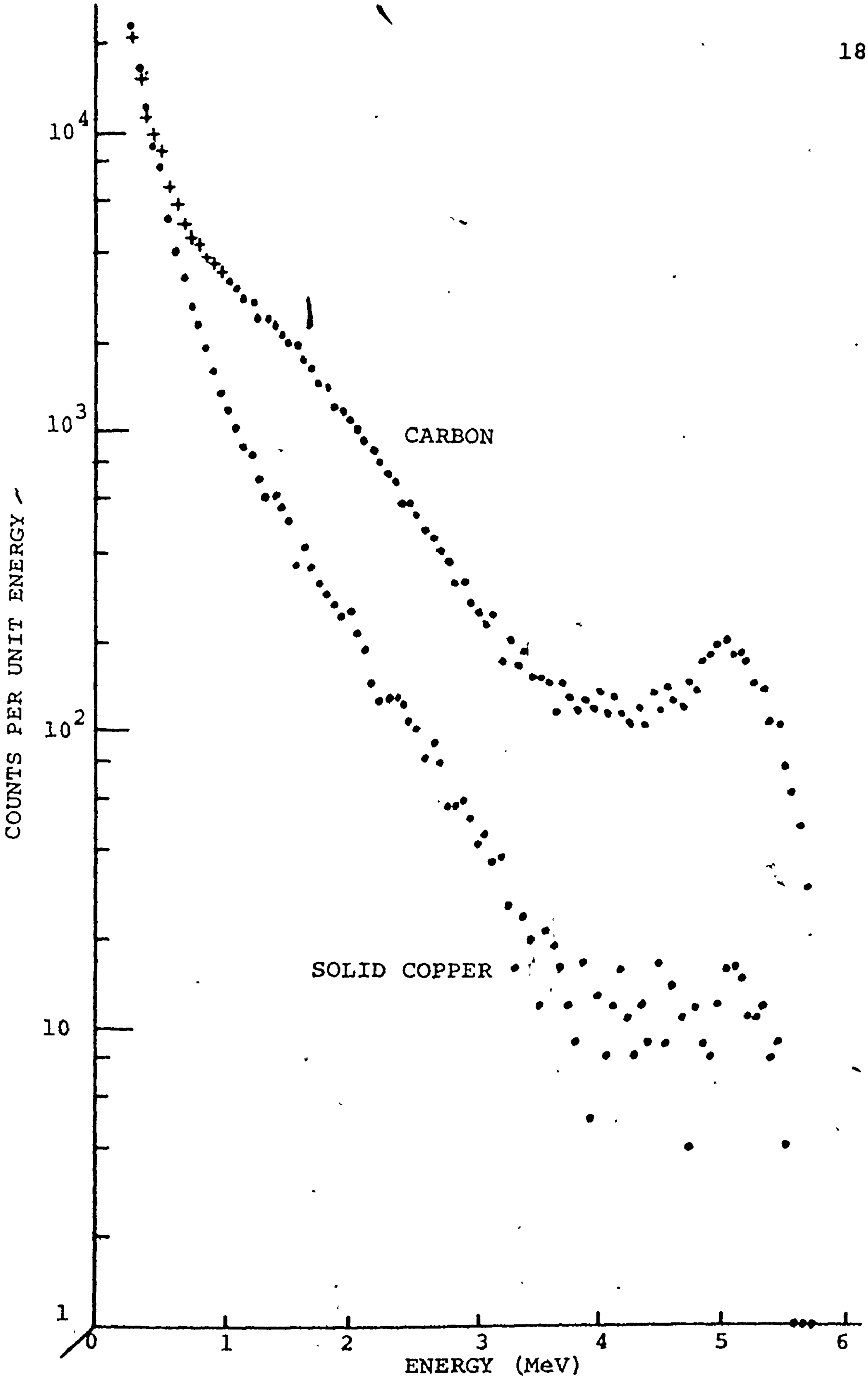

FIG. 5-18 TYPICAL TRIPLE-COINCIDENCE SPECTRA

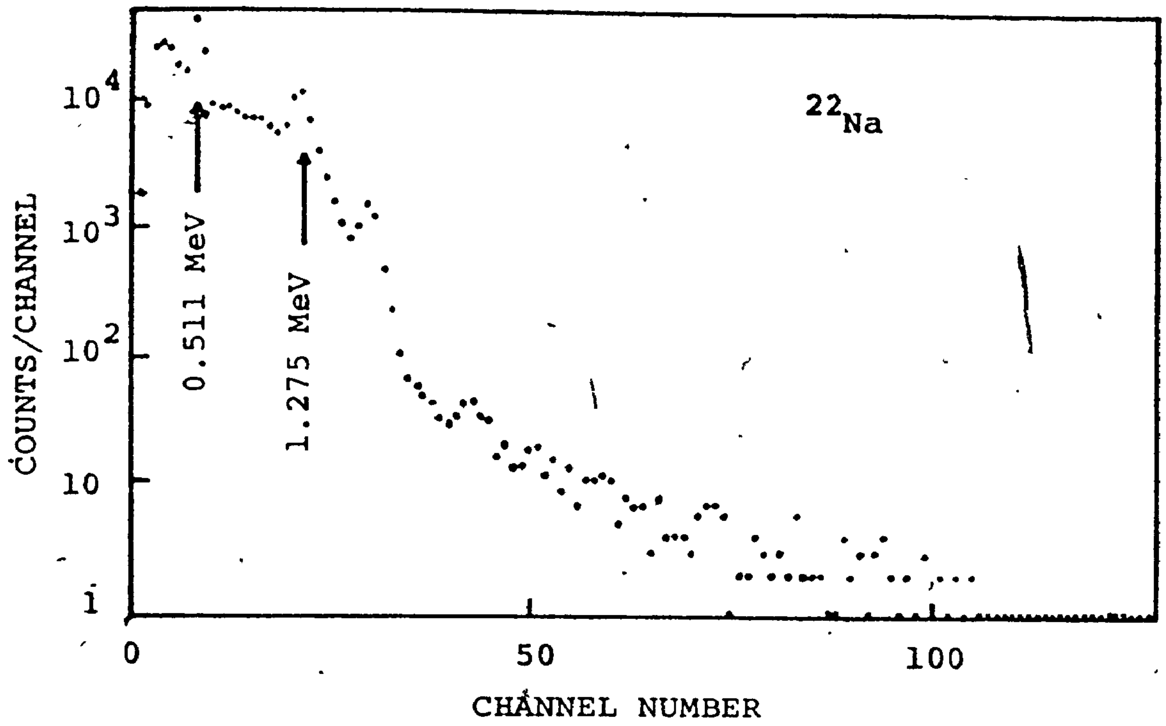

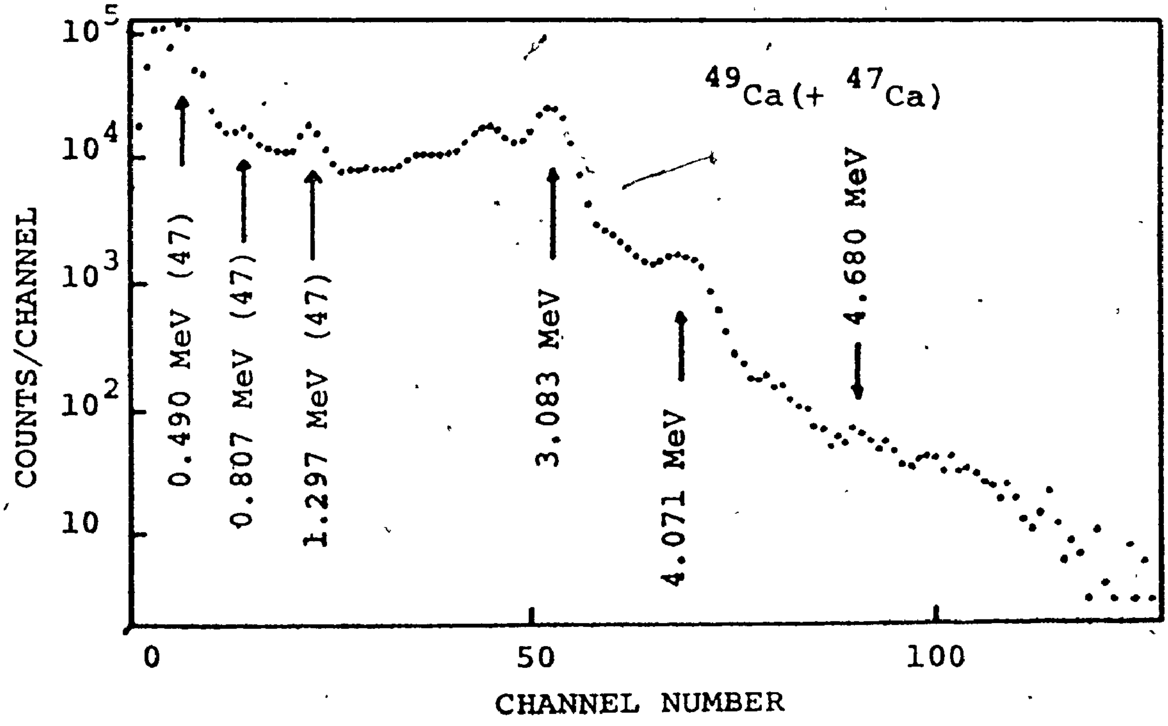

FIG. 5-19 SPECTRA FOR ENERGY CALIBRATION

4.2 MeV to 5.6 MeV with a modal value at roughly 5.1 MeV. The peak content in each spectrum was determined by extrapolating the bremsstrahlung data from energies below 4 MeV for use as a background. The values obtained for the respective targets are listed in table 5-12. It quickly became apparent that the peak content was directly correlated with the integrated reactor power for each target. This can be seen from additional listings within table 5-12 where, despite the wide variety of targets used, the peak content per MW-hr is found to be fairly constant. The weighted average value is actually 23.5±0.6 counts/MW-hr. Also, since there is no strong indication of the targets having attenuated the photons involved, it would therefore appear that the phenomenon does not occur within the targets. One possible clue to the identity of the mechanism is provided by the shape of the peak which is reminiscent of peaks arising from Compton scattering of photons. If the high-energy peak is treated as corresponding to Compton scattering, the angle of scattering is found to be roughly 7±3 degrees. However, detector geometry would appear to preclude direct viewing of all 6.6-MeV gamma rays scattered through angles less than 9 degrees. The range of angles obtained from the data could however be well matched to those angles possible for scattering into the space between a target and the inner wall of the NaI(Tl) annulus. One could perhaps envisage a 6.6-MeV gamma ray being scattered, by the paraffin wax in front of the detector, at the appropriate angle to enter the aforementioned

## TABLE 5-12 CONTENT OF PEAK IN TRIPLES SPECTRA

| Target | Peak Content (counts) | Integrated Reactor Power (MW-hr) | Peak Content/MW-HR |
|---|---|---|---|
| Be | 2496±67 | 96.00 | 26.0±0.7 |
| B | 2109±74 | 92.50 | 22.8±0.8 |
| C | 2071±72 | 90.42 | 22.9±0.8 |
| Al | 556±36 | 22.25 | 25.0±1.6 |
| S | 225±22 | 12.38 | 18.2±1.8 |
| Ti | 250±25 | 11.67 | 21.4±2.1 |
| Fe | 259±23 | 11.00 | 23.5±2.1 |
| Co | 268±22 | 11.42 | 23.5±1.9 |
| Cu-F | 174±21 | 8.92 | 19.5±2.4 |
| Cu-S | 153±16 | 6.08 | 25.2±2.7 |
| Zn | 89±13 | 3.58 | 24.8±3.6 |
| Se | 204±25 | 9.17 | 22.2±2.7 |
| Mo | 88±15 | 3.03 | 29.2±5.0 |
| Cd | 60±15 | 2.93 | 20.4±5.0 |
| Sb | 56±12 | 3.12 | 17.8±3.9 |

space and create a positron-electron pair in air. The annihilation of the positron could conceivably be detected by the one set of diametrically opposite quadrants, while the electron entered the third quadrant. However, it is not clear how almost all of the kinetic energy of the created pair could be selectively delivered to the third quadrant, as required by the high-energy peak in each of the observed bremsstrahlung spectra. If the pair creation were to take place within the third quadrant itself, one could visualize almost all of the total kinetic energy being absorbed and the positron barely escaping into either an adjacent quadrant or the air within the annulus, before annihilating. This however would require transmission of the scattered gamma rays through the lead "nose-cone" of the detector. The necessary path lengths in lead would then range between approximately 4.3 and 15 cm. Since the half-thickness in lead for 6 MeV gamma rays is ∿ 1.3 cm perhaps this explanation is not altogether implausible. However, although the mechanism leading to the high-energy peak is not fully understood, it should be noted that the peak content is both sample-independent and quantitatively insignificant with regard to further interpretation of the experimental data.

Subsequent analysis was predicated on the following reasoning. Since, to a good approximation, the energy spectra for bremsstrahlung within different targets can be assumed to be functionally identical but for an amplitude factor, one need only determine the relative amounts of bremsstrahlung at a specific energy. An energy of 511 keV was chosen for two reasons. Firstly, a computer code was already available for calculation of self-absorption and efficiency factors at that energy. Secondly, if a high photon-energy were chosen, many of the photons would escape detection by the NaI(Tl) annulus as a result of the tendency of high-energy bremsstrahlung to be forward directed. However, 511-keV photons would be more readily detected since not only would they tend to be emitted at larger angles with respect to the direction of the radiating particle, but also, they could be emitted after the particle had suffered many collisions, and therefore lost much of its directionality.

The rate of detection of the 511-keV bremsstrahlung photons, in the triple-coincidence experiment, can be expressed as

$$N_3 = \phi_\gamma \frac{\sigma_\pi}{\sigma} (1-e^{-n\sigma})\varepsilon_1\varepsilon_3 F_s F_3 f P_B(E=511), \qquad (5.42)$$

where $\varepsilon_3$ and $F_3$ are the efficiency and self-absorption factors associated with detection of the bremsstrahlung photon by the third quadrant of the NaI(Tl) annulus. The containment factor for positrons is expressed as f, and $P_B(E=511)$ stands for the probability of radiation of a 511-keV photon by either member of the created pair. Equation (3.1) permits the ratio of triple coincidences to start events to be then expressed as

$$R_3 = \varepsilon_3 F_3 \frac{f}{f_s} P_B(511). \qquad (5.43)$$

Since only relative values of $P_B(511)$ are sought, one can ignore the efficiency factor, which is practically a constant, and the ratio of containment factors, which is essentially unity. Self-absorption factors were therefore calculated, for the several targets involved in this investigation, by appropriate modification of the computer code developed for evaluation of equation (5.29). Results are shown in Table 5-13 which also contains a listing of the respective values of $\mu r$, the product of the linear absorption coefficient for 511-keV photons and the target radius. These results are also presented in figure 5-20 where they are compared with those calculated for an infinite cylinder in which the source strength was uniformly distributed$^{96)}$, an infinite cylinder with a source along its axis, and a 5-cm long cylinder containing a similar linear source. In all instances a diameter of 2.54 cm was assumed. It can be seen that the results for the experimental targets fit sensibly within the bounds provided by the above models.

Before the $R_3$ ratios of equation (5.43) could be obtained, the response function of the detector had to be unfolded from the acquired data. The response was simply modelled as a delta-function peak and a rectangular Compton component. It was reasoned that, since the observed bremsstrahlung spectra were reasonably parallel in log-linear space (figure 5-18), and therefore functionally similar but for an amplitude factor, any operation performed identically on all spectra would leave the relative bremsstrahlung values virtually unchanged. Consequently, the above model was employed. Peak-to-total ratios given by Heath$^{97)}$ for a 3-inch

istics of a quadrant

TABLE 5-13 SELF-ABSORPTION FACTORS FOR TRIPLE COINCIDENCE INVESTIGATION

| Target | $\mu r$ | Self-Absorption Factor, $F_3$ |
|---|---|---|
| Be | 0.182 | 0.809±0.009 |
| B | 0.0851 | 0.906±0.006 |
| C | 0.180 | 0.811±0.009 |
| Al | 0.287 | 0.723±0.012 |
| S | 0.138 | 0.855±0.007 |
| Ti | 0.175 | 0.820±0.008 |
| Fe | 0.421 | 0.620±0.015 |
| Co | 0.370 | 0.657±0.014 |
| Cu-F | 0.301 | 0.709±0.012 |
| Cu-S | 0.941 | 0.368±0.018 |
| Zn | 0.436 | 0.610±0.015 |
| Se | 0.232 | 0.765±0.010 |
| Mo | 0.323 | 0.694±0.013 |
| Cd | 0.480 | 0.580±0.016 |
| Sb | 0.323 | 0.694±0.013 |

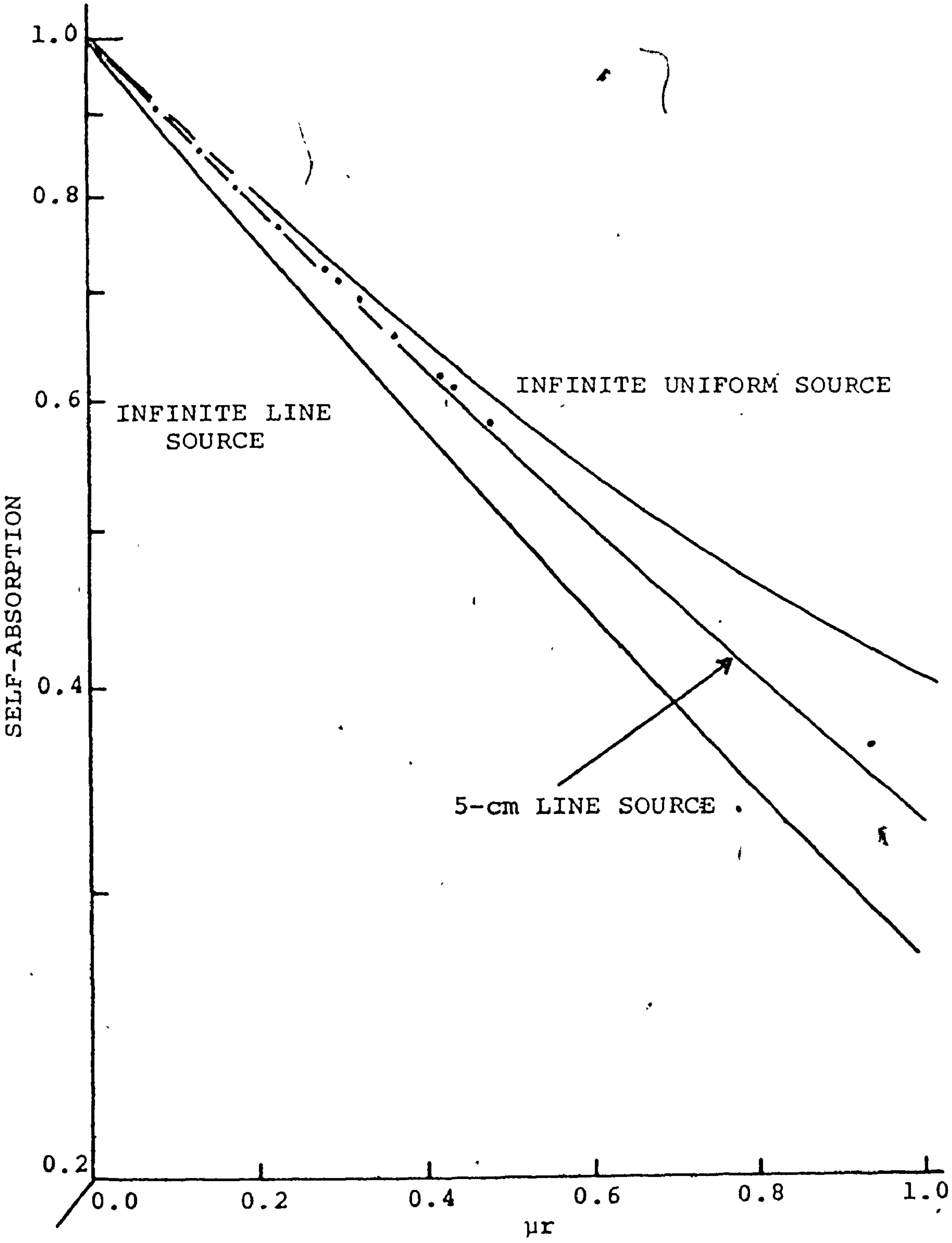

FIG. 5-20 SELF-ABSORPTION FACTORS FOR ESCAPE OF ONE ANNIHILATION QUANTUM. Data are plotted against the product of linear attenuation coefficient and target radius

of the NaI(Tl) were found to closely resemble those for a 3-inch detector. Heath's data were fitted to a polynomial in energy$^{-1}$ for convenience of use. After the spectra had been deconvolved, the $R_3$ ratios of bremsstrahlung events at 511 keV to start events were calculated. The relative values of $P_B(511)$ were then obtained by division of the $R_3$ ratios by the self-absorption factors given in table 5-13. The resulting values are listed in table 5-14 and presented graphically in figure 5-21. It is evident from the trend in the figure that the relative bremsstrahlung amplitude varies linearly with atomic number, as one might have expected from section 2.5.4. It is also evident that several of the graphed results are relatively high. In particular the value for the solid target of copper is considerably higher than that for the target made from copper filings, although one would have expected almost identical results. Since the high results invariably correspond to materials of high density it seems reasonable to assume that they contain a component stemming from Compton scattering. The $R_3/F_3$ ratios were therefore corrected through the relationship

$$R = T(1 + K\langle\text{Compton}\rangle). \tag{5.44}$$

Here R and T stand for the observed and true ratios respectively while K is a constant of proportionality for the contribution from Compton scattering. The average contribution was calculated in terms of

$$\langle\text{Compton}\rangle = \int B(E)\,\frac{\sigma_c(E)}{\sigma(E)}\,[1 - e^{-\mu(E)\langle\ell\rangle}]\,dE, \tag{5.45}$$

TABLE 5-14 RELATIVE BREMSSTRAHLUNG AMPLITUDES

| Target | Brem./Start $(R_3)\times10^3$ | $(R_3/F_3)\times10^3$ |
|---|---|---|
| Be | 2.23±0.05 | 2.76±0.06 |
| B | 2.52±0.04 | 2.76±0.05 |
| C | 2.80±0.04 | 3.45±0.06 |
| Al | 4.83±0.05 | 6.67±0.13 |
| S | 6.07±0.07 | 7.10±0.10 |
| Ti | 7.99±0.12 | 9.75±0.18 |
| Fe | 8.57±0.06 | 13.82±0.34 |
| Co | 9.41±0.08 | 14.32±0.32 |
| Cu-F | 9.90±0.06 | 13.96±0.25 |
| Cu-S | 8.44±0.07 | 22.94±1.16 |
| Zn | 9.90±0.05 | 16.23±0.41 |
| Se | 11.59±0.08 | 15.15±0.23 |
| Mo | 14.36±0.17 | 20.69±0.45 |
| CD | 13.88±0.17 | 23.93±0.71 |
| Sb | 15.36±0.10 | 22.13±0.43 |

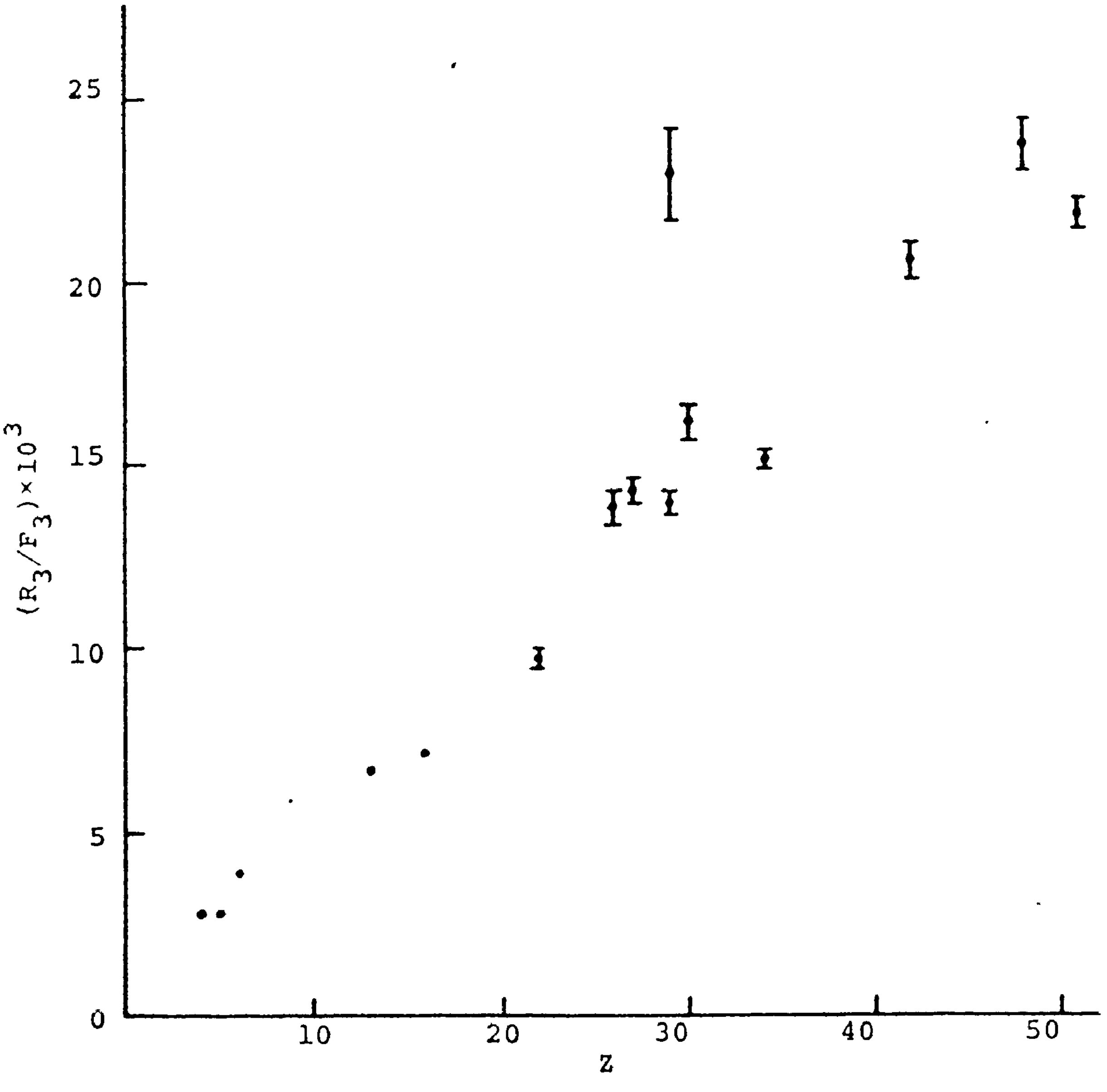

FIG. 5-21 VARIATION OF RELATIVE BREMSSTRAHLUNG AMPLITUDE WITH ATOMIC NUMBER

where $\sigma_c(E)$, $\sigma(E)$ and $\mu(E)$ are the Compton cross section, the total cross section and the total linear absorption coefficient at energy E. B(E) stands for the normalized bremsstrahlung distribution and $\langle \ell \rangle$ the average path length for interaction of the radiation with the target. The bremsstrahlung distribution was approximated by an exponential distribution whose exponent was deduced from the spectrum shown in figure 5-18 for the carbon target. It is interesting to note that even when B(E) was represented by a uniform distribution the maximum change found in the relative values of <Compton> for the various targets was ∿ 5%. This probably comes from the Compton cross section decreasing fairly rapidly with increasing energy. The average path lengths were approximated, to the first order, by the values (∿ 1.45 cm) deduced from the self-absorption factors for 511-keV photons. A 30% change in each of the average path lengths failed to produce any dramatic changes in the relative values of the average Compton probability. The constant of proportionality, K, was determined, under the assumption that the two copper targets should have the same value for T, to be 3.78±0.93. The true ratios were then evaluated for each target. The new relative values are shown in table 5-15 and figure 5-22. A least-squares fit of the data in figure 5-22 to a straight line provided a slope of value $(0.24 \pm 0.006) \times 10^{-3}$ and an intercept of $(0.924 \pm 0.058) \times 10^{-3}$. The fit also revealed that, on the average, the error bars shown in figure 5-22 were 47% larger than they need be. One can interpret the results of the least-squares modelling as meaning that the

TABLE 5-15 RELATIVE BREMSSTRAHLUNG RATIOS CORRECTED FOR COMPTON EFFECT

| Target | Relative Bremsstrahlung Ratios×$10^3$<br>Calculated | <br>Fitted |
|---|---|---|
| Be | 1.82±0.16 | 1.89±0.04 |
| B | 2.20±0.12 | 2.13±0.04 |
| C | 2.27±0.19 | 2.37±0.04 |
| Al | 3.74±0.41 | 4.06±0.05 |
| S | 5.06±0.36 | 4.78±0.06 |
| Ti | 6.52±0.54 | 6.23±0.09 |
| Fe | 6.69±0.86 | 7.19±0.11 |
| Co | 7.33±0.89 | 7.44±0.12 |
| Cu-F | 7.82±0.85 | 7.92±0.13 |
| Cu-S | 7.82±1.32 | 7.92±0.13 |
| Zn | 7.81±1.01 | 8.16±0.13 |
| Se | 9.42±0.88 | 9.12±0.16 |
| Mo | 11.67±1.27 | 11.05±0.20 |
| Cd | 11.79±1.50 | 12.50±0.23 |
| Sb | 12.99±1.34 | 13.22±0.25 |

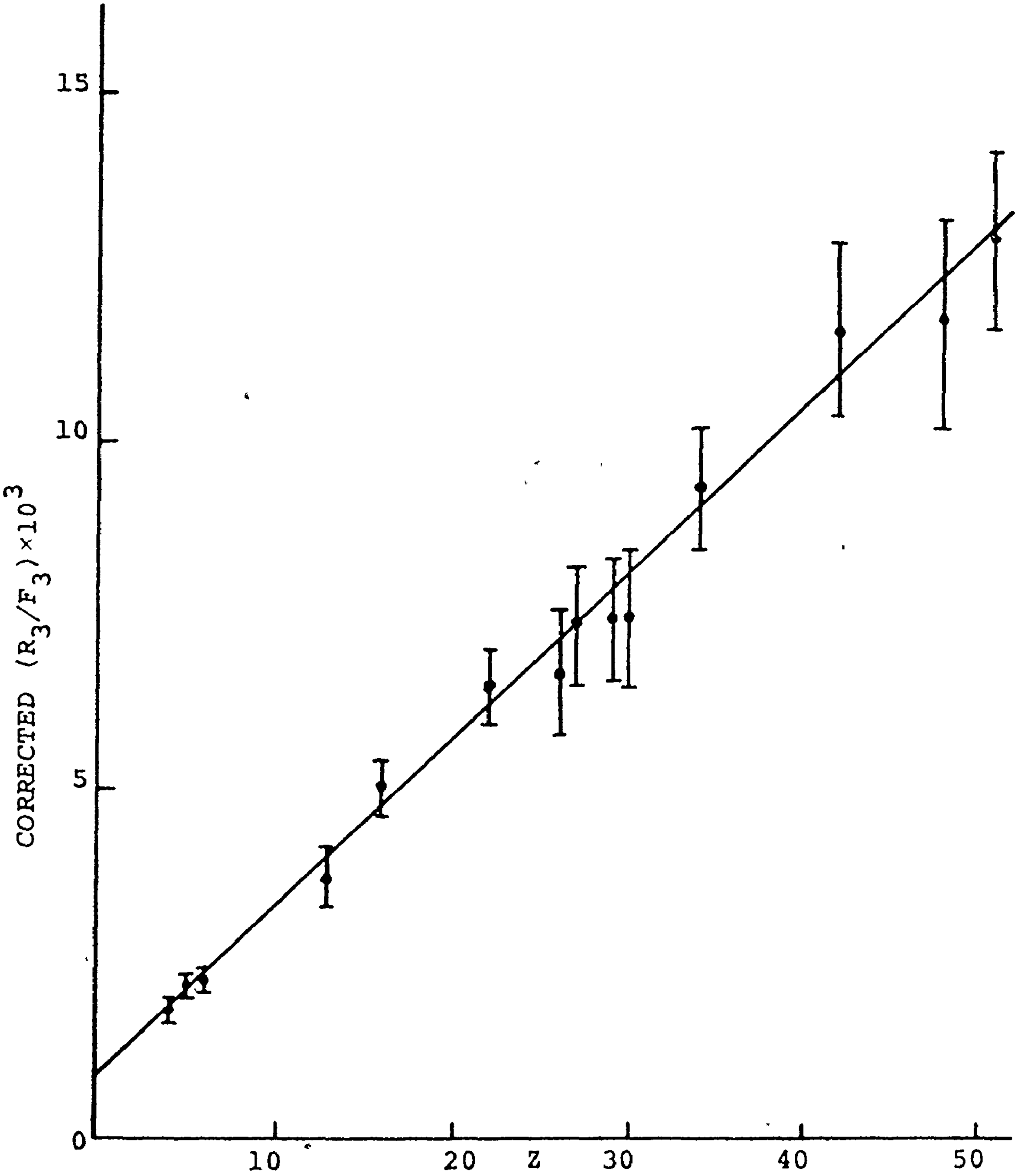

FIG. 5-22 VARIATION OF RELATIVE BREMSSTRAHLUNG AMPLITUDE WITH ATOMIC NUMBER, AFTER CORRECTION FOR COMPTON CONTRIBUTION. The solid curve represents a least-squares fit to a straight line.

relative bremsstrahlung ratios vary directly as Z + 3.83(±0.24), where Z represents atomic number.

Although it is not altogether surprising that the bremsstrahlung ratios vary with Z plus a constant, one would have expected electronic bremsstrahlung to contribute, at most, a constant of value 1.0. Perhaps the value of 3.83 can be mainly attributed to use of an incorrect response function. However, when a more correct response function, consisting of a parabolic peak of variable width and a trapezoidal Compton "tail", was used, the constant was found to be slightly larger than 3.83. Perhaps the large value of the constant is really indicative of a true phenomenon. A radiative pair-production (page 15) effect, in which a residual gamma ray accompanies the created pair, provides one possible explanation. Volkovyskii$^{29)}$ has indicated that, for a very high-energy photon simultaneously creating a photon of much lower energy and an ultrarelativistic pair, the differential cross section can be expressed as

$$d\sigma_{\pi\gamma} = \left(\frac{30.6\ r_o^2 Z^2 \alpha^2}{\pi}\right)\frac{d(h\nu_2)}{h\nu_2} \quad \ell n\left(\frac{h\nu_1}{m_o c^2}\right). \qquad (5.46)$$

Here $\nu_1$ and $\nu_2$ are the frequencies of the incident and the residual photon respectively. Although the energy conditions of this experiment are very different from those applied by Volkovyskii, a comparison of equation (5.46) with the expression for normal pair production, equation (1.14), reveals that the cross sections share the same $Z^2$ dependence. Since the above effect is also of order $\alpha/\pi$ weaker than normal pair production, it could provide a constant contribution of appropriate size. Moreover, the $1/h\nu_2$ dependence expressed in equation (5.46) should provide an energy spectrum which is similar to that for bremsstrahlung.

# CHAPTER VI

# CONCLUSIONS

## 6.1 THE BREMSSTRAHLUNG-CASCADE EFFECT

Before the probability of double pair production could be extracted from the results of the investigation of fourfold coincidences, it was required that all pairs produced by bremsstrahlung be taken into account. Since the threshold energy for normal pair production is 1.022 MeV ($2m_oc^2$), and since the associated cross section is significant only for photons of energy well above the minimum, the major contribution to the cascade effect could be expected to come from bremsstrahlung quanta with energy of a few MeV or greater. Such energetic photons could only come from those beta particles that were correspondingly energetic. In Chapter II it has been pointed out (equations (2.36) and (2.71)) that high-energy members of created pairs and high-energy bremsstrahlung photons have angular distributions which are peaked in the forward direction. It was therefore assumed, for the purpose of calculation of the relative effect of the cascade process in each target, that all bremsstrahlung radiation was forward-directed. The relative number of bremsstrahlung-produced pairs was consequently calculated for each target in accordance with the expression

$$N_{B\pi} = \int_{2m_oc^2}^{11m_oc^2} dE \int_0^L B(E) \frac{\mu e^{-\mu x}}{1-e^{-\mu L}} \frac{\sigma_\pi(E)}{\sigma(E)} (1-e^{-\mu(E)(L-x)})dx. \quad (6.1)$$

In this equation B(E) represents the form of the energy distribution of internal bremsstrahlung from created pairs and $\mu e^{-\mu x}/(1-e^{-\mu L})$ provides the exponential distribution in the number of primary pairs in terms of the axial depth x within a target of length L and the linear absorption coefficient, μ, for 6.6-MeV photons. The pair cross section, total cross section, and linear absorption coefficient for a photon of energy E are represented by $\sigma_\pi(E)$, $\sigma(E)$ and $\mu(E)$ respectively.

The functional form used for B(E) was derived from the assumption of a bremsstrahlung intensity (number of photons × photon energy) distribution of

$$I_o(E) = (E_o-E)^2/E_o \tag{6.2}$$

from a beta particle of energy $E_o$. The integrated intensity was therefore established as proportional to $E_o{}^2$ in accordance with equation (2.76). Although equation (6.2) provides a very simple expression for the intensity distribution, it leads to remarkably close agreement in shape with the theoretical distribution calculated by Zerby and Moran$^{101)}$. When an assumed uniform distribution of electron and positron energies was incorporated into equation (6.2), the distribution in the number of photons of energy E was found to be

$$N(E) = \frac{I(E)}{E} = \frac{1}{x} - 4 + 3x - 2x\ell nx. \tag{6.3}$$

Here x stands for $E/E_m$ where $E_m$ represents the maximum possible energy for either member of a pair. The function B(E) was consequently obtained for each target as the product of N(E) and the appropriate relative bremsstrahlung amplitude extracted from the investigation of triple coincidences. The results of the evaluation of equation (6.1) for the several targets are given in table 6-1 where they are presented as normalized to a value of 100 for the target of solid copper.

However, the possibility of pair production by a bremsstrahlung photon which had undergone Compton scattering also required consideration. An appropriate term was therefore added to equation (6.1) to provide the expression

$$N_{BC\pi} = N_{B\pi} + \int_{2m_oc^2}^{11m_oc^2} dE \int_0^L dx \int_0^{L-x} dy \int_0^{\theta_{max}} B(E) \frac{\mu e^{-\mu x}}{1-e^{-\mu L}} \frac{\mu(E)e^{-\mu(E)y}}{\sigma(E)} [\frac{d\sigma}{d\Omega}(E,\theta)] \times$$

$$\times\ 2\pi \sin\theta d\theta \frac{\sigma_\pi(E'(E,\theta))}{\sigma(E')} [1-e^{-\mu(E')\ell(x,y,\theta)}] \ . \qquad (6.4)$$

Here y represents the distance in the forward direction that the bremsstrahlung travels before interacting, and $d\sigma(E,\theta)/d\Omega$ is the differential cross section for Compton scattering of a photon of energy E into a solid angle $d\Omega$ about $\theta$, the direction of scattering. The path length for interaction of the scattered photon of new energy E' is represented by $\ell$. The results from evaluation of equation (6.4) for each target are also shown in table 6-1 as normalized values. The same normalization constant was used to obtain the relative values of $N_{B\pi}$ and $N_{BC\pi}$. The relative insignificance of Compton-produced pairs is evidenced in the ratios, $N_{BC\pi}/N_{B\pi}$, provided in the fourth column of table 6-1. However,

TABLE 6-1 RELATIVE NUMBER OF BREMSSTRAHLUNG-PRODUCED PAIRS

| TARGET | NORMALIZED $N_{B\pi}$ | NORMALIZED $N_{BC\pi}$ | $\frac{N_{BC\pi}}{N_{B\pi}}$ |
|---|---|---|---|
| Be | 0.859±0.018 | 0.870±0.018 | 1.014 |
| B | 0.648±0.012 | 0.653±0.012 | 1.008 |
| C | 1.603±0.027 | 1.625±0.027 | 1.014 |
| Al | 9.02 ±0.11 | 9.21 ±0.11 | 1.021 |
| S | 7.530±0.095 | 7.622±0.095 | 1.012 |
| Cu-F | 43.81 ±0.72 | 44.86 ±0.73 | 1.024 |
| Cu-S | 100.0 ±1.6 | 105.9 ±1.7 | 1.059 |

the ratios were used to correct the fourfold-coincidence results, listed in table 5-8, for pairs produced by Compton-scattered photons. The resulting values are listed in table 6-2 under the heading $P_{2\pi}$, the probability of two-pair production processes relative to normal pair production.

Fortunately, the dominant interference effect for $Z>20$ is the bremsstrahlung-cascade process[20)]. For the solid-copper target, it was estimated that the bremsstrahlung-cascade effect could account for approximately 95% of the $P_{2\pi}$ value. This followed from the assumption that the only other major process for targets of high atomic number, the direct-cascade effect, provided a contribution of roughly $(0.3 \text{ to } 0.4)\times 10^{-5}\, Z$[27)]. The bremsstrahlung-cascade probabilities, $P_{B\pi}$, given in table 6-2 were calculated relative to the value of solid copper, by means of the normalized $N_{B\pi}$ values of table 6-1.

## 6.2 DOUBLE PAIR PRODUCTION AND THE DIRECT-CASCADE EFFECT

The sum of the relative probabilities for double pair production and the direct-cascade process, $P_{\pi\pi} + P_{D\pi}$, were obtained by subtracting the $P_{B\pi}$ values from the corresponding $P_{2\pi}$ values. The results are listed in table 6-2. Figure 6-1 shows the same results plotted against atomic number. Since, for incident gamma rays of constant energy, $P_{\pi\pi}$ is predicted by theory to be constant and $P_{D\pi}$ to be directly proportional to atomic number, the relationship expressed in figure 6-1 was modelled to a straight line to separate the probability sums

TABLE 6-2 TWO-PAIR-PRODUCTION PROBABILITIES

| TARGET | $P_{2\pi}\times10^5$ | $P_{B\pi}\times10^5$ | $(P_{\pi\pi}+P_{D\pi})\times10^5$ |
|---|---|---|---|
| Be | 3.99±0.89 | 1.68±0.08 | 2.31±0.89 |
| B | 4.09±0.73 | 1.27±0.06 | 2.82±0.73 |
| C | 6.02±0.83 | 3.14±0.14 | 2.88±0.84 |
| Al | 22.9 ±1.4 | 17.6 ±0.8 | 5.3 ±1.6 |
| S | 20.6 ±1.4 | 14.7 ±0.6 | 5.9 ±1.5 |
| Cu-F | 89.5 ±3.2 | 85.6 ±3.9 | 3.9 ±5.1 |
| Cu-S | 206.5 ±8.0 | 195.5 ±8.2 | |

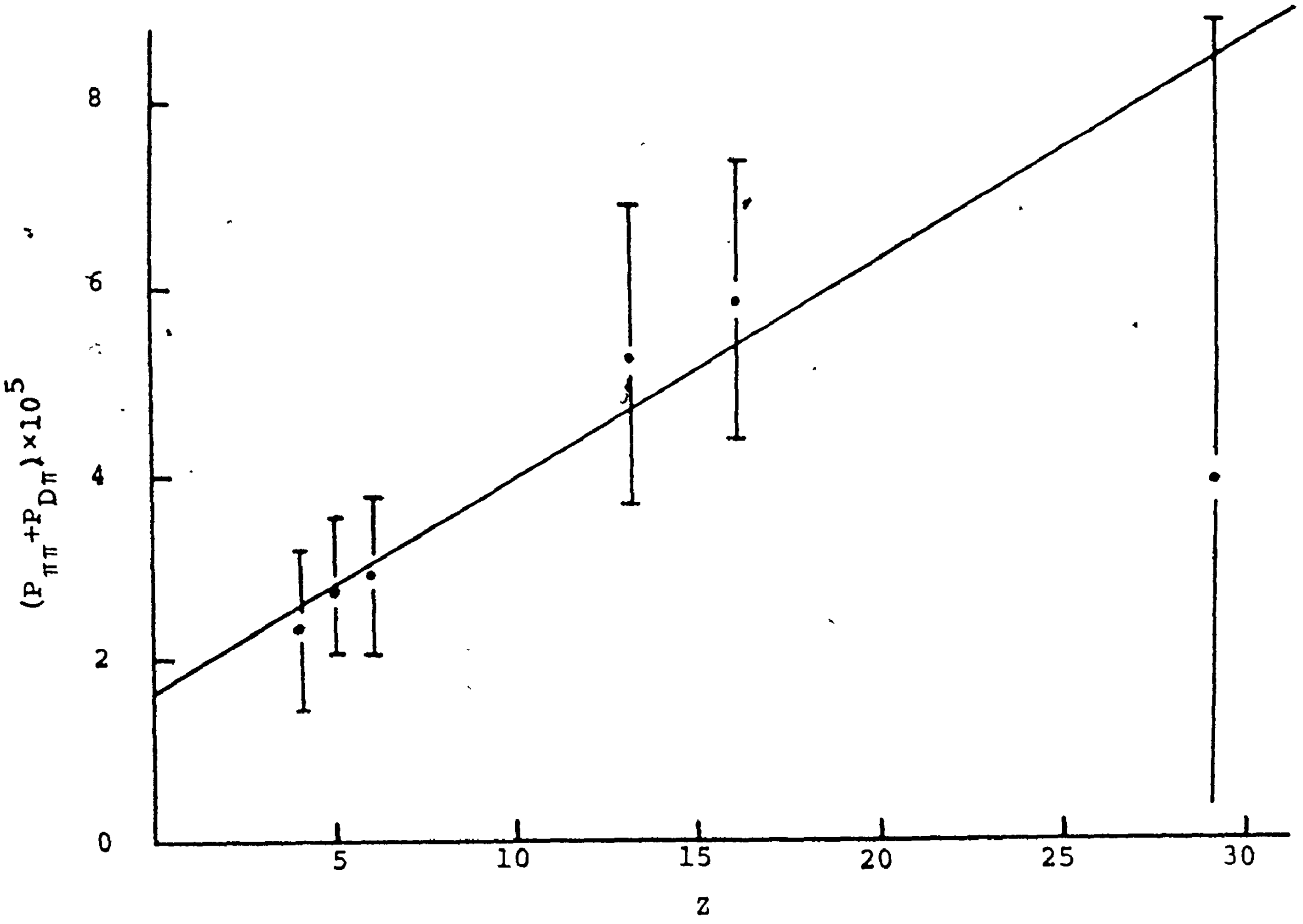

FIG. 6-1 VARIATION OF THE SUM OF DOUBLE-PAIR AND DIRECT-CASCADE PROBABILITIES WITH ATOMIC NUMBER

into the two component probabilities. The weighted least-squares solution provided a direct-cascade probability of

$$P_{D\pi} = (0.24\pm0.11)\times10^{-5}\ Z \qquad (6.5)$$

from the slope of the line, and a double-pair-production probability of

$$P_{\pi\pi} = (1.54\pm0.83)\times10^{-5} \qquad (6.6)$$

from the value of the intercept. The relationships stated in the above equations are, of course, for 6.6-MeV gamma rays on average.

## 6.3 DISCUSSION

The measured values of $P_{D\pi}$ and $P_{\pi\pi}$ are consistent with theoretically predicted values. A calculation of the direct-cascade probability from the expression of Wilkinson and Alburger[20], with gamma rays of 6.6-MeV energy, yields $P_{D\pi} \sim 0.31\times10^{-5}$ Z. The double-pair probability has been estimated[20] via equation (1.16) as $P_{\pi\pi} \sim 2\times10^{-5}$. Agreement also exists between the present results and the values of $P_{D\pi}$ and $P_{\pi\pi}$ reported[27] from a preliminary investigation in this laboratory as $(0.38\pm0.19)\times10^{-5}$ Z and $(2.4\pm1.6)\times10^{-5}$ respectively. However, discrepancies do exist between the $P_{2\pi}$ values of the present work and those from the preliminary investigation. These values are compared in table 6-3. It can be seen that there is agreement within stated error for most targets but that inconsistencies exist for the copper targets. One reason for the differences is that in the preliminary work the stop efficiency was measured as 0.121±0.006

TABLE 6-3 COMPARISON OF TWO-PAIR PROBABILITIES

| TARGET | PRESENT WORK | PRELIMINARY WORK[27) |  |
|---|---|---|---|
|  | $P_{2\pi} \times 10^5$ | $P_{2\pi} \times 10^5$ | Corrected $P_{2\pi} \times 10^5$ |
| Be | 3.99±0.89 | 5.1±1.5 | 5.5±1.6 |
| C | 6.02±0.83 | 5.8±1.1 | 6.2±1.2 |
| Al | 22.9 ±1.4 | 19.1±2.5 | 20.8±2.7 |
| Cu-F | 89.5 ±3.2 | 71.3±3.4 | 78.9±3.8 |
| Cu-S | 206.5 ±8.0 | 143.4±8.6 | 201.0±12.4 |

compared to 0.114±0.003 in the present work. The former, which was calculated from the results of an experiment involving a $^{22}$Na positron emitter, required an estimated correction for coincidence summing of a 1.28-MeV photon with the annihilation quanta. Although a smaller efficiency would undoubtedly make the preliminary values for $P_{2\pi}$ higher, it is clear that considerable disagreement would still exist for the copper samples. The major source of difference is found in the correction for self-absorption. The self-absorption factors for the preliminary work were extracted from a twofold coincidence experiment as relative values. The factors were not measured absolutely since that would have required accurate knowledge of containment probabilities and gamma-ray flux in addition to efficiency. After the relative values had been corrected for calculated containment probabilities, they were normalized to what was believed to be the correct value for the carbon target (0.7). However, the highly attenuative solid-copper target has a self-absorption factor which is particularly sensitive to absolute errors. The factor of 0.221 measured in the above fashion for the solid-copper target can be compared with the value of 0.157 used in the present work. That the latter value is more reasonable can be seen from calculated values of 0.202 for a uniform cylindrical source of infinite length$^{96)}$, 0.137 for a linear source imbedded in a cylinder 2.54 cm in diameter and 5 cm in length, and ∿ 0.20 for a similar cylinder containing a uniform distribution of source centres. The proper experimental value should of course fit somewhere between the latter two values with perhaps some bias towards the former of two. The results obtained from correction of the preliminary $P_{2\pi}$ values for efficiency and self-absorption are listed in table 6-3. A reasonable consistency with present $P_{2\pi}$ values is evident. However further analysis conducted with the corrected $P_{2\pi}$ values produces errors which are sufficiently large to preclude any significant value for $P_{D\pi}$. Despite this, a residual value of $(3.3\pm2.2)\times10^{-5}$ is found for $P_{\pi\pi}$.

Since there could be some doubt that the relative bremsstrahlung amplitudes, measured in the investigation of triple coincidences, really varied as Z+3.83, the $P_{2\pi}$ values of the present work were analysed in accordance with the findings of Dance et al[88)] that the amplitudes were directly proportional to Z. The results of this analysis are presented in table 6-4 where they are compared with the values found for the variation with Z+3.83. In both sets of results the value for the target of copper filings is obviously relatively low. One could therefore infer that perhaps the $P_{B\pi}$ value for copper filings was overestimated. This could stem from either the relative $N_{B\pi}$ value (table 6-1) for copper filings being too large, or the self-absorption factor for the solid-copper target being too low. However, because the error in the value of $P_{\pi\pi}+P_{D\pi}$ for copper filings is very large, that value is virtually ignored in a least-squares modelling of the sum of probabilities to a linear

TABLE 6-4 COMPARISON OF ANALYSES FOR SUBTRACTION OF BREMSSTRAHLUNG-CASCADE CONTRIBUTIONS

| TARGET | $(P_{\pi\pi}+P_{D\pi})\times 10^5$ (assuming bremsstrahlung amplitudes $\propto$ Z+3.83) | $(P_{\pi\pi}+P_{D\pi})\times 10^5$ (assuming bremsstrahlung amplitudes $\propto$ Z) |
|---|---|---|
| Be | 2.31±0.89 | 3.13±0.89 |
| B | 2.82±0.73 | 3.37±0.73 |
| C | 2.88±0.84 | 4.10±0.84 |
| Al | 5.3 ±1.6 | 9.3 ±1.7 |
| S | 5.9 ±1.5 | 8.7 ±1.7 |
| Cu-F | 3.9 ±5.1 | 3.9 ±5.1 |

relationship with atomic number. When the newly-calculated values of $P_{\pi\pi}+P_{D\pi}$ were so modelled, $P_{D\pi}$ was established as $(0.41\pm0.14)\times10^{-5}Z$ and $P_{\pi\pi}$ as $(1.61\pm1.02)\times10^{-5}$. Both of these values are consistent with the theoretically predicted values and the results of the present work reported in section 6.2.

In summary then, it is believed that definite evidence has been found of double pair production. The cross section for the process relative to that for single pair production, for 6.6-MeV gamma rays, is reported as

$$\frac{\sigma_{\pi\pi}}{\sigma_{\pi}} = (1.54\pm0.83)\times10^{-5}. \tag{6.7}$$

# APPENDIX A

## TIME-DEPENDENT PERTURBATION THEORY

In almost any book devoted to quantum mechanics one can find a good treatment of time-dependent perturbation theory[102)]. In this theory the time-dependent Schrödinger equation,

$$i\hbar \frac{\partial\psi}{\partial t} = H\psi, \qquad \text{(A.1)}$$

is used to describe the evolution in time of a system represented by the wave function $\psi$. The Hamiltonian H of the system is seen as having two parts, a time-independent part, $H_o$, whose stationary solution is known, and a small time-dependent part, $H'$, for which an approximate solution is required. The latter component is construed as the Hamiltonian of a perturbation. $\psi$ can be written in terms of a spatial wave function and a time dependent part as

$$\psi = R(r)e^{-i(Et/\hbar)} \ . \qquad \text{(A.2)}$$

Here r refers to all the relative coordinates of the interacting system. Before the onset of perturbation at t=0, the initial state can be described by

$$H_oR_j = E_jR_j \ , \qquad \text{(A.3)}$$

where the eigenfunction $R_j(r)$ is orthonormal. The perturbed system can then be expanded in terms of the complete set of stationary eigenfunctions as

$$\psi = \sum_j a_j(t) R_j e^{-i(E_j t/\hbar)} , \qquad (A.4)$$

where the coefficients, $a_j$, assume a time dependence, and afford a probability interpretation for finding the system in a particular state in terms of $|a_j(t)|^2$. Substitution of equation (A.4) into equation (A.1), with the realization that equation (A.3) holds true, results in

$$i h \sum_j \frac{\partial a_j}{\partial t} R_j e^{-i(E_j t/\hbar)} = \sum_j H' a_j R_j e^{-i(E_j t/\hbar)} . \qquad (A.5)$$

Multiplication of equation (A.5) by $R_f^*$, followed by integration over all space, provides

$$i\hbar \frac{\partial a_f}{\partial t} e^{-i(E_f t/\hbar)} = \sum_j a_j e^{-i(E_f t/\hbar)} \int R_f^* H' R_j dr. \qquad (A.6)$$

This reduces to

$$\frac{\partial a_f}{\partial t} = \frac{1}{i\hbar} \sum_j a_j H'_{fj} e^{i(\omega_{fj} t)} , \qquad (A.7)$$

where

$$H'_{fj} \equiv \int R_f^* H' R_j dr, \qquad (A.8)$$

and

$$\omega_{fj} \equiv \frac{E_f - E_j}{\hbar} . \qquad (A.9)$$

The treatment so far is exact. The perturbation approximation is introduced at this stage in order to perform the integration of $\partial a_f/\partial_t$. This consists of replacing $H'$ by $\epsilon H'$ and expressing each "a" as a power series in $\epsilon$. Typically one can set

$$a_s = a_s^{(o)} + \varepsilon a_s^{(1)} + \varepsilon^2 a_s^{(2)} + \dots \quad \text{(A.10)}$$

The procedure is then to substitute the series expansions into equations (A.7), equate equal powers of $\varepsilon$, and finally set $\varepsilon$ equal to unity. One should note that the unperturbed starting condition is described by

$$a_j^{(o)} = a_j(o) = 1. \quad \text{(A.11)}$$

The aforementioned substitution provides

$$\frac{\partial a_f^{(o)}}{\partial t} + \varepsilon \frac{\partial a_f^{(1)}}{\partial t} + \varepsilon^2 \frac{\partial a_f^{(2)}}{\partial t} + \dots = \frac{1}{i\hbar} \sum_j \left[\varepsilon a_j^{(o)} + \varepsilon^2 a_j^{(1)} + \dots\right] H'_{fj} e^{i(\omega_{fj} t)} . \quad \text{(A.12)}$$

Clearly the zero-order expansion term gives

$$\frac{\partial a_f^{(o)}}{\partial t} = 0, \quad \text{(A.13)}$$

which implies that

$$a_f^{(o)} = \delta_{fj}. \quad \text{(A.14)}$$

In the first-order approximation, equation (A.12) becomes

$$\frac{\partial a_f^{(1)}}{\partial t} = \frac{1}{i\hbar} \sum_j a_j^{(o)} H'_{fj} e^{i(\omega_{fj} t)} , \quad \text{(A.15)}$$

$$= \frac{1}{i\hbar} H'_{fj} e^{-(\omega_{fj} t)} . \quad \text{(A.16)}$$

If the perturbation is assumed to be described as a step function which has a constant finite value between times o and t, equation (A.16) can be integrated to give

$$a_f^{(1)} = \frac{1}{i\hbar} H'_{fj} \int_0^t e^{i(\omega_{ij} t)} dt , \tag{A.17}$$

$$= \frac{1}{\hbar\omega_{fj}} H'_{fj} \left[1 - e^{i(\omega_{fj} t)}\right] . \tag{A.18}$$

By neglecting higher orders of approximation, one can then write the probability of a transition from state j to state f, with a time t spend under the influence of a step-function perturbation, as

$$|a_f|^2 \approx |a_f^{(1)}|^2 , \tag{A.19}$$

$$= \frac{4|H'_{fj}|^2}{(\hbar\omega_{fj})^2} \sin^2\left(\frac{\omega_{fj} t}{2}\right) . \tag{A.20}$$

Since there could be many possible final states, the concept of transition probability per unit time can be introduced as

$$\lambda = \frac{1}{t} \sum_f |a_f|^2 . \tag{A.21}$$

If one assumes that $H'_{fj}$ varies slowly within the group of final states, in the energy region around $E_f$, the quantity $|H_{fj}|^2$ can be taken to denote a mean value independent of the actual value $E_f$, and therefore can be treated as essentially a constant. Furthermore, if one can regard the final states as forming a continuum, it is then possible to express the number of states per unit energy, in the interval around $E_f$, in the form of an energy level density $\rho(E_f)$. Equation (A.21) can then be re-expressed as

$$\lambda = \frac{1}{t}\int_{-\infty}^{\infty} |a_f|^2 \rho(E_f)\,dE_f \;. \tag{A.22}$$

However, since $dE_f$ is identically $\hbar d\omega_{fj}$, equation (A.22) becomes

$$\lambda = \frac{1}{t}\int_{-\infty}^{\infty} |a_f|^2 \rho(E_f)\hbar d\omega_{fj} \;, \tag{A.23}$$

$$= \frac{1}{t}\int_{-\infty}^{\infty} \frac{|H_{fj}|^2}{(\hbar\omega_{fj})^2}\, \rho(E_f)\hbar d\omega_{fj} \;, \tag{A.24}$$

$$= \frac{4}{\hbar t}\, |H_{fj}|^2 \rho(E_f) \int_{-\infty}^{\infty} \frac{\sin^2(\omega_{fj}t/2)}{\omega_{fj}^2}. \tag{A.25}$$

Following evaluation of the integral in equation (A.25) as $\pi t/2$, one can write the transition probability rate as

$$\lambda = \frac{2\pi}{\hbar}\, |H'_{fj}|\, \rho(E_f)\,. \tag{A.26}$$

# APPENDIX B

# THE DIRAC THEORY FOR HALF-SPIN RELATIVISTIC PARTICLES

## B.1 THE RELATIVISTIC EQUATION

Klein and Gordon103), using the relativistic energy relation

$$E^2 = p^2c^2 + m^2c^4 \tag{B.1}$$

as a starting point, were able to produce a relativistic wave equation. The equation is readily obtained through substitution in equation (B.1) of the operator definitions

$$\hat{E} = i\hbar \frac{\partial}{\partial t} , \tag{B.2}$$

and

$$\hat{p} = \frac{\hbar}{i} \nabla . \tag{B.3}$$

The result is then given as

$$\frac{\partial^2 \psi}{\partial t^2} = \left(c^2 \nabla^2 - \frac{m^2 c^4}{\hbar^2}\right) \psi . \tag{B.4}$$

A disturbing feature of this equation is that the probability density,

$$\rho = \frac{i\hbar}{2mc^2} \left(\psi^* \frac{\partial \psi}{\partial t} - \frac{\partial \psi^*}{\partial t} \cdot \psi\right) , \tag{B.5}$$

may be negative as well as positive. Moreover, the solution wave function $\psi$ in equation (B.4) transforms as a scalar under Lorentz transformations, therefore permitting only a translational degree of freedom. However, in dealing with an electron, one must also be able to account for its spin.

Dirac[104], sought to eliminate these difficulties by constructing a linear differential wave equation of first order in the time derivative. He consequently rewrote equation (B.1) as

$$E = (\vec{\alpha}\cdot\vec{p})c + \beta(mc^2). \tag{B.6}$$

The corresponding wave equation may then be specified as

$$[-E + (\vec{\alpha}\cdot\vec{p})c + \beta(mc^2)]\psi = 0 , \tag{B.7}$$

or as

$$\frac{\hbar}{i}\frac{\partial\psi}{\partial t} + \frac{\hbar c}{i}(\vec{\alpha}\cdot\vec{\nabla})\psi + m^2c^2\psi = 0 , \tag{B.8}$$

upon substitution of the operator relationships expressed in equations (B.2) and (B.3). The vector and scalar parameters, $\vec{\alpha}$ and $\beta$, can be shown to satisfy the relationships

$$\alpha_x^2 = \alpha_y^2 = \alpha_z^2 = \beta^2 = 1 , \tag{B.9}$$

$$\alpha_x\alpha_y+\alpha_y\alpha_x = \alpha_x\alpha_z+\alpha_z\alpha_x = \alpha_y\alpha_z+\alpha_z\alpha_y = 0 , \tag{B.10}$$

and

$$\alpha_x\beta+\beta\alpha_x = \alpha_y\beta+\beta\alpha_y = \alpha_z\beta+\beta\alpha_z = 0 . \tag{B.11}$$

An appropriate representation may be given as

$$\alpha = \begin{pmatrix} \vec{0} & \vec{\sigma} \\ \vec{\sigma} & \vec{0} \end{pmatrix} \tag{B.12a}$$

and

$$\beta = \begin{pmatrix} \vec{1} & \vec{0} \\ \vec{0} & -\vec{1} \end{pmatrix} . \tag{B.12b}$$

Here $\vec{0}$ and $\vec{1}$ are zero and unit 2×2 matrices, and $\vec{\sigma}$ stands for the second-rank Pauli spin matrices,

$$\sigma_x = \begin{pmatrix} 0 & 1 \\ 1 & 0 \end{pmatrix} , \tag{B.13a}$$

$$\sigma_y = \begin{pmatrix} 0 & -i \\ i & 0 \end{pmatrix} , \tag{B.13b}$$

and

The wave function is then represented as a column matrix with four components by

$$\psi = \begin{bmatrix} \psi_1(x,y,z,t) \\ \psi_2(x,y,z,t) \\ \psi_3(x,y,z,t \\ \psi_4(x,y,z,t) \end{bmatrix} \tag{B.14}$$

The probability density may now be written as

$$\rho = \sum_\mu |\psi_\mu|^2 = \psi^\dagger\psi \; . \tag{B.15}$$

Here $\psi^\dagger$ is the Hermitian conjugate wave function formed as a row vector of the four complex conjugate components. In this definition, the probability density is always positive definite. The equation of continuity,

$$(\psi^\dagger \frac{\partial\psi}{\partial t} + \frac{\partial\psi^\dagger}{\partial t}\psi) + \mathrm{div}\,\vec{j} = 0 \; , \tag{B.16}$$

is then satisfied by the current

$$\vec{j} = c\psi^\dagger\vec{\alpha}\psi \; . \tag{B.17}$$

So far the theory developed has been for a free particle. The transformation to the description of a particle in an electromagnetic field($A^\mu = \{\phi,\vec{A}\})$ is accomplished by allowing E to tend to $E-e\phi$ and $\vec{p}$ to tend to $\vec{p} - \frac{e}{c}\vec{A}$ . This leads to the wave equation for a bound particle,

$$\{(E-e\phi)+c(\vec{\alpha}\cdot[\vec{p} - \frac{e}{c}\vec{A}]) + \beta mc^2\}\psi = 0 \; . \tag{B.18}$$

The validity of equation (B.18) can be demonstrated by comparison with previous theory. If one considers a relativistic $\frac{1}{2}$-spin particle in a Coulomb field given by

$$e\phi = -\frac{Ze^2}{r} \quad , \qquad \text{(B.19a)}$$

and

$$\vec{A} = 0 \; , \qquad \text{(B.19b)}$$

the energy levels, including rest mass, are found to be

$$E_n = mc^2\left\{1 + \frac{1/137}{(n-k+[k^2-(1/137)^2]^{1/2})^2}\right\}^{-1/2} \qquad \text{(B.20)}$$

for

$$n = 1,2,3,\ldots \qquad \text{(B.21)}$$

and

$$k = 1,2,\ldots,n \; . \qquad \text{(B.22)}$$

Equation (B.20), which, but for small differences, shows good agreement with experimental results, is equivalent to the Sommerfeld fine structure formula.

In the nonrelativistic limit with conditions

$$\phi = 0 \qquad \text{(B.23a)}$$

and

$$\frac{\partial \vec{A}}{\partial t} = 0 \quad , \qquad \text{(B.23b)}$$

equation (B.18) reduces to the normal Schroedinger equation with an additional term of

$$-\frac{e\hbar}{2mc}\,(\vec{\sigma}\cdot\vec{H})$$

in the Hamiltonian. This energy component is that due to a particle of magnetic moment $e\hbar/2mc$ in a magnetic field of strength $\vec{H}$.

Also, in the nonrelativistic limit, the central field problem described by

$$e\phi = V(r) \qquad \text{(B.24a)}$$

and

$$\vec{A} = 0 \qquad \text{(B.24b)}$$

reduces to the Schroedinger equation with a spin-orbit term of

$$\frac{1}{2mc^2 r}\,\frac{\partial V(r)}{\partial r}\,(\vec{S}\cdot\vec{L}) \ ,$$

where $\vec{L}(=\vec{r}\times\vec{p})$ is the orbital angular momentum of the particle and $\vec{S}(=\frac{1}{2}h\vec{\sigma})$ is the spin angular momentum.

## B.2 ELECTRON-POSITRON THEORY

As noted previously in equation (B.14), the wave function $\psi$ has four components. One pair of these components refers to a particle of positive energy and two possible spin orientations, while the other pair provides a similar description for a particle of negative energy. The wave function can be written in recognition of the above pairing as

$$\psi = \begin{pmatrix} u \\ v \end{pmatrix} , \qquad \text{(B.25)}$$

where

$$u \equiv \begin{pmatrix} \psi_1 \\ \psi_2 \end{pmatrix} = \begin{pmatrix} u_{+1} \\ u_{-1} \end{pmatrix} , \qquad \text{(B.26)}$$

and

$$v \equiv \begin{pmatrix} \psi_3 \\ \psi_4 \end{pmatrix} = \begin{pmatrix} v_{+1} \\ v_{-1} \end{pmatrix} . \qquad \text{(B.27)}$$

The positive and negative subscripts designate the two possible spin directions. The field-free equation, (B.7), can now be written as

$$E\begin{pmatrix} u \\ v \end{pmatrix} = c(\vec{\sigma}\cdot\vec{p})\begin{pmatrix} v \\ u \end{pmatrix} + mc^2\begin{pmatrix} u \\ -v \end{pmatrix} . \qquad \text{(B.28)}$$

If one assumes the Z-direction to be the distinguishable direction, one can substitute $\sigma_z p_z$ for $\vec{\sigma}\cdot\vec{p}$. Equation (B.28) then provides the four linear equations

$$(E-mc^2)u_{+1} = p_z v_{+1} \ , \qquad (B.29)$$

$$(E+mc^2)v_{+1} = p_z u_{+1} \ , \qquad (B.30)$$

$$(E-mc^2)u_{-1} = -p_z v_{-1} \ , \qquad (B.31)$$

and

$$(E+mc^2)v_{-1} = -p_z u_{-1} \ . \qquad (B.32)$$

Consider the positive-energy, spin-up situation in which for arbitrary normalization

$$u_{+1} = 1 \qquad . \qquad (B.33a)$$

and

$$u_{-1} = v_{-1} = 0 \ . \qquad (B.33b)$$

From equation (B.29) it is clear that

$$v_{+1} = \frac{(E-mc^2)}{p_z} = \frac{p_z}{(E+mc^2)} \ , \qquad (B.34)$$

where the latter equality is established by multiplying numerator and demoninator by $(E+mc^2)$. An equation identical to equation (B.34) can be obtained by considering equation (B.30). Similarly the negative-energy,spin-down situation may be realized with

$$v_{-1} = 1 \qquad (B.35a)$$

and

$$u_{+1} = v_{+1} = 0 \ . \qquad (B.35b)$$

The solution from equations (B.31) and (B.32) is

$$u_{-1} = \frac{p_z}{|E|+mc^2} \ . \qquad (B.36)$$

Similar considerations can be made for the positive-energy, spin-down situation, and the negative-energy, spin-up situation.

The wave functions describing these four possible situations are then

$$_{+}\psi_{\uparrow} = \begin{pmatrix} 1 \\ 0 \\ \frac{p_z}{E+mc^2} \\ 0 \end{pmatrix} , \qquad (B.37)$$

$$_{+}\psi_{\downarrow} = \begin{pmatrix} 0 \\ 1 \\ \frac{-p_z}{E+mc^2} \end{pmatrix} , \qquad (B.38)$$

$$_{-}\psi_{\uparrow} = \begin{pmatrix} \frac{-p_z}{|E|+mc^2} \\ 0 \\ 1 \\ 0 \end{pmatrix} , \qquad (B.39)$$

and

$$_{-}\psi_{\downarrow} = \begin{pmatrix} 0 \\ \frac{p_z}{|E|+mc^2} \\ 0 \\ 1 \end{pmatrix} . \qquad (B.40)$$

Here the arrows indicate spin direction, and the positive and negative signs indicate the sign of the energy. Proper normalization,via

$$u^2 + v^2 = 1, \qquad (B.41)$$

is established for each wave function by the same normalization constant,

$$N = \left[\frac{|E|+mc^2}{2mc^2}\right]^{1/2} \qquad (B.42)$$

The physical interpretation becomes clear upon operating on the above spinor wave functions with both $\sigma_z$ and the Hamiltonian operator $\hat{H}$. One obtains

$$\sigma_z\psi = \pm\psi \ , \qquad (B.43)$$

where the signs refer to spin direction, and

$$\hat{H}\psi = \pm|E|\psi \ . \qquad (B.44)$$

Here the signs indicate negative or positive energy. There are no solutions for which any other spin component, than that in the direction of motion, is sharp. The positive-energy solutions correspond to electrons whereas the negative-energy solutions correspond to positrons. The Dirac positron-electron energy diagram (figure 2-2) stems directly from the possibility of such negative-energy solutions. This is seen from the energy equation, (B.1), which can be rewritten as

$$E = \pm\sqrt{p^2c^2 + m^2c^4} \ . \qquad (B.45)$$

When a particle has no momentum, its total energy is then $\pm mc^2$. If the particle is given momentum, its total energy then becomes either more positive than $+mc^2$ or more negative than $-mc^2$, thus establishing a gap of $2mc^2$ between the allowed region of positive energy and the negative energy "sea".

## REFERENCES

1. A. P. Arya, Fundamentals of Nuclear Physics, Chapter VIII, p. 261, Allan and Bacon, Inc., Boston, 1966.
2. C. S. Wu and S. A. Moszkowski, Beta Decay, p. 4, John Wiley and Sons, New York, 1966.
3. E. Fermi, Z. Physik 88, 161 (1934).
4. T. D. Lee and C. N. Yang, Phys. Rev. 105, 1671 (1957).
5. J. D. Jackson, Classical Electrodynamics, John Wiley and Sons, New York, 1963.
6. W. Heitler, The Quantum Theory of Radiation, Introduction, p. xi, Clarendon Press, Oxford, 1954.
7. J. M. Blatt and V.F. Weisskopf, Theoretical Nuclear Physics, John Wiley and Sons, New York, 1952.
8. S. Rosseland, Z. Physik 14, 173 (1923).
9. R. D. Evans, The Atomic Nucleus, McGraw-Hill Book Co., New York, 1955.
10. M. Mayer, Phys. Rev. 75, 1969 (1949).
11. S.G. Nilsson, Mat. F. Medd. 29, No. 16 (1955).
12. J. E. Nafe, E. B. Nelson and I. I. Rabi, Phys. Rev. 71, 914 (1947).

    H. M. Foley and P. Kusch, Phys. Rev. 72, 1256 (1947); 73, 412 (1948); 74, 250 (1948).
13. E. S. Dayhoff, S. Triebwasser and W. E. Lamb, Phys. Rev. 89, 98 (1953).
14. J. C. Wesley and A. Rich, Phys. Rev. A4, 1341 (1971).
15. B. E. Lautrup, A. Peterman and E. de Rafael, Physics Reports 3C, 193 (1972).

16. Ibid. 15, p. 200.

Ibid. 15, p. 204.

17. F. Mandl, Introduction to Quantum Field Theory, Interscience Publishers, Inc., New York, 1959.

18. J. M. Jauch and F. Rohrlich, The Theory of Photons and Electrons, p. 134, Addison-Wesley, Cambridge, 1955.

19. R. P. Feynman, Phys. Rev. 76, 769 (1949); 80, 440 (1949).

20. D. H. Wilkinson and D. E. Alburger, Phys. Rev. C5, 719 (1972).

21. J. E. Hooper and D. T. King, Phil. Mag. 41, 1194 (1950).

22. W. Heitler, Quantum Theory of Radiation, p. 181, Oxford University Press, 1944.

23. L. M. Afrikian, Zh. Eksperim. i Teor. Fiz-Pis'ma Redakt. 33, 531 (1957); [transl: JETP Letters 6, 414 (1958)].

24. H. Bethe and W. Heitler, Proc. Roy. Soc. A146, 83 (1934).

25. S. N. Gupta, Phys. Rev. 99, 1015 (1955).

26. V. G. Serbo, Zh. Eksperim. i Teor. Fiz-Pis'ma Redakt. 12, 50 (1970); [transl: JETP Letters 12, 39 (1970)].

27. A. Robertson, W. V. Prestwich and T.J. Kennett, Phys. Rev. Lett. 29, 966 (1972).

28. G. M. Shklyarevskii, Zh. Eksperim. i Teor. Fiz. 46, 690 (1964); [transl: Sov. Phys. JETP 19, 470 (1964)].

29. R. Yu. Volkovyskii, Yad. Fiz. 2, 878 (1965); [transl: Sov. J. Nucl. Phys. 2, 626 (1966)].

30. Ibid. 9, Appendix A.

31. U. Fano, Nucleonics 11 (8), 8 (1953); 11 (9), 55 (1953).

32. R. D. Evans, Handbuch der Physik (S. Flügge,ed.) Vol. 34, p. 218, Springer, Berlin, 1958.

33. H. Hertz, Ann. Physik 31, 983 (1887).

34. A. Einstein, Ann. Physik 17, 132 (1905).

35. G. D. Latyshev, Revs. Mod. Phys. 19, 132 (1947).

36. Ibid. 6, Chapter V, p. 204.

37. J. J. Thomson, Conduction of Electricity Through Gases, Vol. II, p. 256, Cambridge University Press, London and New York, 1933.

38. M. Stobbe, Ann. Physik 7, 661 (1930).

39. G. W. Grodstein, Natl. Bur. Std. (U.S.) Circ. No. 583 (1957).

40. M. Gavrila, Phys. Rev. 113, 514 (1959).

R. H. Pratt, Phys. Rev. 117, 1017 (1960); 119, 1619 (1960).

R. H. Pratt, R. D. Levee, R. L. Pexton and W. Aron, Phys. Rev. A134, 898 (1964).

D. Liberman, J. T. Waber and D. T. Cromer, Phys. Rev. 137, A27 (1965).

41. H. Brysk and C.D. Zerby, Phys. Rev. 171, 292 (1968); Union Carbide Report UCC/DSSD-299 (1967).

42. G. Rakavy and A. Ron, Phys. Rev. 159, 50 (1967).

43. R. D. Schmickley and R. H. Pratt, Phys. Rev. 164, 104 (1967).

44. Ibid. 7, Chapter 10.

45. Ibid. 6, Chapter 5.

46. P.V.C. Hough, Phys. Rev. 73, 266 (1948).

47. H. A. Bethe and L. C. Maximom, Phys. Rev. 93, 768 (1954); 87, 156 (1952).

48. H. Davies, H.A. Bethe and L. C. Maximom, Phys. Rev. 93, 788 (1954).

H. Davies and H. A. Bethe, Phys. Rev. 87, 156 (1952).

49. H. A. Bethe, Proc. Cambridge Phil. Soc. 30, 524 (1934).

50. L. C. Henry and T. J. Kennett, Can. J. Phys. 49, 1167 (1971).

51. Ibid. 39, p. 55.

52. I. Øverbø, K. J. Mork and H. Olsen, Phys. Rev. 175, 1978 (1968).

53. A. Borsellino, Phys. Rev. 89, 1023 (1953).

54. H.S. Sandhu, E.H. Webb, R.C. Mohanty and R.R. Roy, Phys. Rev. 125, 1017 (1962).

55. P.A.M. Dirac, Proc. Cambridge Phil. Soc. 26, 361 (1930).

56. S. DeBenedetti and H.C. Corben, Ann. Rev. Nucl. Sci. 4, 191 (1954).

M. Deutsch, Progr. Nucl. Phys. 3, 131 (1958).

L. Simons, Handbuch der Physik (S. Flügge, ed.) vol. 34, p. 139, Springer, Berlin 1958.

57. F. Perrin, Compt. Rend. 197, 1100 (1933).

58. J. Joseph and F. Rohrlich, Revs. Mod. Phys. 30, 354 (1958).

59. Ibid. 9, Chapter 24, p. 709.

60. C.J. Frei, H.H. Staub and H. Winkler, Helv. Phys. Acta 31, 491 (1958).

61. A. H. Compton, Bull. Natl. Res. Council (U.S.) No. 20, p. 19 (1922); Phys. Rev. 21, 207,483 (1923).

62. O. K. Klein and Y. Nashina, Z. Physik 52, 853 (1929).

63. Ibid. 9, Chapter 18, p. 568.

64. E. Rutherford, Phil. Mag. 21, 669 (1911).

65. C. G. Darwin, Phil. Mag. 25, 201 (1913).

66. N. F. Mott, Proc. Roy. Soc. A124, 425 (1929); A135, 429 (1932).

67. W. A. McKinley, Jr. and H. Feshbach, Phys. Rev. 74, 1759 (1948).

68. R. R. Roy and R. D. Reed, Interactions of Photons and Leptons with Matter, Chapter 4, Academic Press,Inc., New York, 1968.

69. N. F. Mott, Proc. Roy. Soc. A126, 259 (1930).

70. C. Møller, Ann. Physik 14, 531 (1932).

71. H. J. Bhabha, Proc. Roy. Soc. A154, 195 (1936).

72. H. A. Bethe, Handbuch der Physik (S. Flügge, ed.) Vol. 24, p. 273, Springer, Berlin, 1933.

F. Bloch, Ann. Physik 16, 285 (1933); Z. Physik 81, 363 (1933).

73. H. A. Bethe, Ann. Physik 5, 325 (1930).

74. R. R. Wilson, Phys. Rev. 60, 749 (1941).

C. Bakker and E. Segrè, Phys. Rev. 81, 489 (1951).

75. F. Rohrlich and B. C. Carlson, Phys. Rev. 93, 38 (1954).

76. H. J. Bhabha, Proc. Roy. Soc. A164, 257 (1938).

77. W. Duane and F. L. Hunt, Phys. Revs. 6, 116 (1915).

78. H. W. Koch and J. W. Motz, Revs.Mod. Phys. 31, 920 (1959).

79. H. A. Bethe and W. Heitler, Proc. Roy. Soc. A146, 83 (1934).

80. H. A. Bethe and L. C. Maximom, Phys. Rev. 93, 768 (1954).

H. Davies, H. A. Bethe and L.C. Maximom, Phys. Rev. 93, 788 (1954).

H. Olsen, Phys. Rev. 99, 1335 (1955).

H. Olsen and L. C. Maximom, Phys. Rev. 110, 589 (1958).

81. Ibid. 68, Chapter 6.

82. L. I. Schiff, Phys. Rev. 70, 87 L (1946).

83. Ibid. 58.

84. Ibid. 9, Chapter 21, p. 616.

85. H. W. Koch and J. W. Wyckoff, IRE Trans. on Nucl. Sci. NS-5, No. 3 (1958).

86. H. A. Kramers, Phil. Mag. 46, 836 (1923).

87. W. W. Buechner, R.J. Van de Graaff, E. A. Burrill and A. Sperduto, Phys. Rev. 74, 1348 (1948).

88. W. E. Dance, D. H. Rester, B. J. Farmer and J. H. Jackson, J. Appl. Phys. 39, 2881 (1968); 41, 2682 (1970).

89. Ibid. 9, Chapter 21, p. 623.

90. L. Katz and A. S. Penfold, Revs. Mod. Phys. 24, 28 (1952).

91. A. T. Nelms, Natl. Bur. Std. (U.S.) Circ. No. 577 (1956).

92. M. J. Berger and S. M. Seltzer, NASA SP-169, 1968.

93. D. H. Hughes and R.B. Schwartz, Neutron Cross Sections BNL 325, Second Edition, 6 (1958).

94. P. Fettweiss and M. Saidane, Nucl. Phys. A139, 113 (1969).

95. L. Nichol, A. Lopez, A. Robertson, W.V. Prestwich and T. J. Kennett, Nucl. Instr. and Meth. 81, 263 (1970).

96. K. M. Case, F. De Hoffmann and G. Placzek, *Introduction to the Theory of Neutron Diffusion* Vol. 1, Los Alamos Scientific Laboratory, Los Alamos, New Mexico, 1953.

97. R. L. Heath, *Scintillation Spectrometry*, AEC (U.S.) Report TID-4500, Idaho, 1964.

98. C. M. Lederer, J. M. Hollander and I. Perlman, Table of Isotopes, Sixth Edition, Table I, John Wiley and Sons, Inc., New York, 1968.

99. E. Storm and H. I. Israel, Nuclear Data Tables 7, 565 (1970).

100. T. J. Kennett, W. V. Prestwich, G. L. Keech, Nucl. Instr. and Meth. 29, 325 (1964).

101. C.D. Zerby and H. S. Moran, ORNL Report No. 2454 (1958).

102. A.Messiah, Quantum Mechanics, Vol. 2, Chapter XVII, p. 724, North-Holland Publishing Co., Amsterdam, 1966.

103. Ibid. 102, Chapter XX, p. 884.

104. P.A.M. Dirac, Proc. Roy. Soc. (London) A117, 610 (1928).